Integrating AVO, Seismic Inversion, and Rock Physics in Agua Fría 3D Seismic Cube
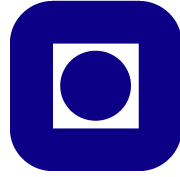
Juan Carlos Gloria Lopez

Norwegian University of Science and Technology
Department of Petroleum Engineering and Applied Geophysics

NTNU

Norwegian University of Science and Technology

Department of Petroleum Engineering and Applied Geophysics

Integrating AVO, Seismic Inversion, and Rock Physics in Agua Fría 3D Seismic Cube

Author:

Juan Carlos Gloria López

Supervisor:

Pr. Per Avseth

June 10, 2014

Acknowledgment

Abstract

Department of Petroleum Engineering and Applied Geophysics

Norwegian University of Science and Technology

Integrating AVO, Seismic Inversion, and Rock Physics in Agua Fría 3D Seismic Cube

By

Juan Carlos Gloria López

Ten exploratory wells have been drilled in the Agua Fría area, led by amplitude anomalies and structural highs. Five of them resulted in dry wells and the other five in gas and oil discoveries. In some of these wells, water sands respond seismically as amplitude anomalies. On the other hand, some oil and gas sands are not easily recognizable from post-stack seismic data. Bright spots are also observed in the study area.

Seismic interpretation can be uncertain if no geology is related to elastic response of the subsurface rocks. The purpose of this thesis is to integrate diagenesis data from log and core data, rock physics models, AVO analysis and seismic inversion information to characterize the Agua Fría 3D seismic cube.

Mechanical compaction and sorting are the main factors affecting the porosity trend in the selected wells according to the rock physics modeling.

AVO class III are the main class present in the study area. However, these responses can be related to brine, oil or gas sands. Rock physics templates and seismic inversion data are useful to understand these responses and to decrease uncertainty to the analysis of these anomalies.

The integration of these methodologies allow to improve the understanding of the seismic amplitude response to different geological facies present in the study area.

Contents

List of Figures

List of Tables

Chapter 1

Introduction

In 2009 four prospects were drilled in the Agua Fría 3D seismic cube led by amplitude anomalies which resulted in dry wells. Since then, different geological and geophysical methodologies have been applied to the area which resulted in four new oil and gas discoveries. AVO analysis and seismic inversion are two of the most applied methods for amplitude analysis. However, these techniques are barely used together to improve the data evaluation. Seismic interpretation can be uncertain if no geology is related to elastic response of the subsurface rocks. For this reason, this project aims to integrate diagenesis data from log and core data, rock physics models, AVO analysis and seismic inversion information to improve the understanding of the seismic amplitude response to the different geological facies present in the study area.

Velocity-depth trends and rock physics models are the link between the elastic properties measured by logs or seismic with geological rock properties, such as lithology, pore fluids, fluid saturation, sorting, diagenesis, and pressure. AVO analysis evaluates amplitude anomalies with the variation of offset or incident angle for the identification of pore fluids and lithologies. Seismic inversion methods are based in the convolutional model which reverse the seismic data by removing the wavelet effect of the trace to determine acoustic impedance and VpVs ratio.

Since rock physics, AVO analysis and seismic inversion methods are directly related to contrasts in acoustic impedance and VpVs ratio, these techniques complement each other and decrease the interpretation uncertainty. In past years, these methodologies were barely integrated with each other. However, the limitations of each technique and the difficulty of finding hydrocarbons in complex geology areas have yield an attempt to

integrate this processes for a better understanding of the seismic response in a given area.

Porosity depth trends due to compaction have been studied by Magara (1980 [59]), and Ramm and Bjoerlykke (1994 [60]). These trends are applied for rock physics templates (RPTs) which were first presented by Ødegaard and Avseth (2003 [63]). RPTs integrated with AVO analysis are useful to predict the expected amplitude and AVO response at a sand-shale interface as a function of depth. Several authors including AlMustafa, (2011 [70]), Box and Doss (2008 [71]), and Nasser (2010 [72]) have attempted to define the optimal depth interval where AVO analysis more reliable.

This thesis aims to integrate diagenesis data from log and core data, rock physics models, AVO analysis, and seismic inversion information to improve the understanding of the seismic amplitude response to the different geological facies present in the study area. The first step is to make a feasibility analysis to define whether it is possible to discern fluids, porosity and lithologies from elastic log parameters. The next step is to define porosity and velocity trends with rock physics models. These models allow to establish lithologies and fluid trends. In the AVO analysis stage, different attributes are estimated, cross plotted and mapped. The last process is simultaneous seismic inversion. At this stage, acoustic impedance, VpVs ratio and density are estimated, cross plotted and mapped. The last step is to integrate and interpret rock physics trends, AVO analysis and seismic inversion results. The combination and comparison of these techniques with the geology of the area allows to decrease uncertainty of the final seismic interpretation.

Chapter 2

Geological Background

2.1 Location

The Agua Fría 3D seismic cube is located at the Veracruz Basin (VB) in southeastern Mexico. The VB is geologically limited to the north by the Santa Ana High, to the south by the Salina del Istmo Basin, to the west by the Zongolica Range and to the east it extends to the Gulf of Mexico (GOM) (Figure 2.1).

2.2 Tectonic framework

The basin passed trough a rift stage from Triassic to Middle Jurassic and a drift stage from Middle Jurassic to Early Cretaceous. From Late Jurassic to Late Cretaceous this area was part of the passive margin of the GOM. From Late Cretaceous to Eocene the Laramidic orogeny created the Sierra Madre Oriental thrusted belt. This tectonic load originated a tertiary foreland basin. A sub horizontal subsidence continued until Miocene (Ferrari, 1999 [1]; Prost, 2001 [2]). During Middle Miocene the basin changed from a foreland basin to a forearc basin due to a reorganization in the suduction system in southern Mexico. Compressive and transpressive stresses affected the VB during Early and Middle Miocene. The subsequent uplifting caused the erosion of rocks from Paleocene to Middle Miocene.

Jeanette et al., (2002 [3]) made an informal subdivision of the major trends that share structural style, kinematics and timing of deformation. From west to east the trends are the western Homolcine, the Loma Bonita Anticline, the Tlacotalpan Syncline, the Antón Lizardo Trend, and the Coatzacoalcos Reentrant (Figure 2.2).
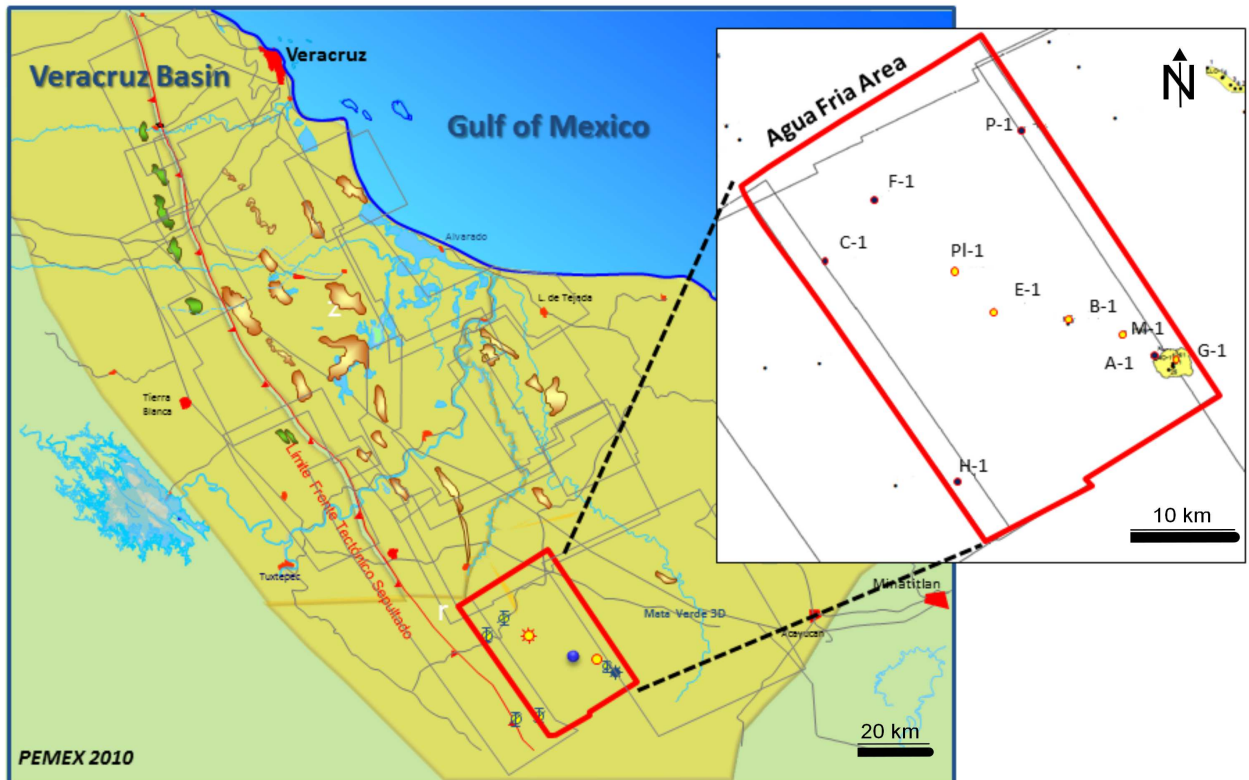
Figure 2.1: Location of the Agua Fría 3D seismic cube within the Veracruz Basin, Mexico (Courtesy of PEMEX).

2.3 Stratigraphy

The sedimentary rocks of the VB lay on a Paleozoic-Triassic metamorphic basement (PEMEX-IMP-Amoco, 1995 [4]; Viniegra, 1965 [5]). Four main tectonic sequences are observed within the basin as shown in Fig. 2.3.

Synrift events includes continental rocks from Todos Santos formation formed during the opening of the GOM in Middle Jurassic (Rueda-Gaxiola, 2003 [6]; Tarango-Ontiveros, 1985 [7]). The passive margin tectonic sequence started with marine sediments of Kimmeridgian age and are overlayed by rocks of the Tepexilotla formation of Tithonian age (Tarango-Ontiveros, 1985 [7]; PEMEX-IMP-Amoco, 1995 [4]). During Early Cretaceous, sands and platform limestones were deposited. Platform limestones of the Orizaba formation were deposited in Middle Jurassic in this area. For Turonian age, a partial sinking of
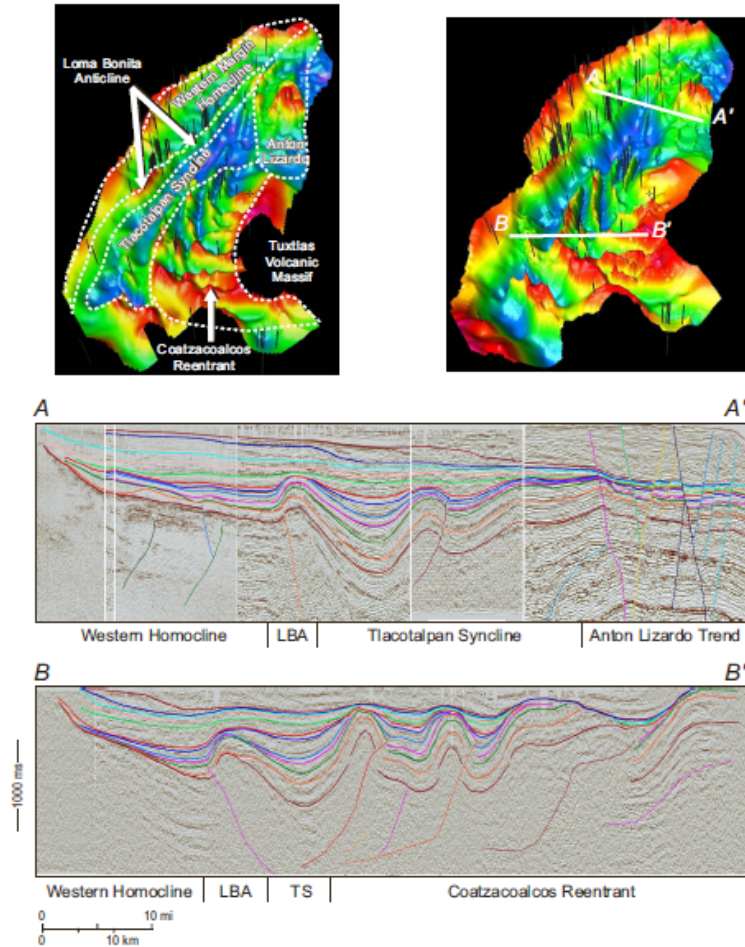
Figure 2.2: Structural trends of the Veracruz Basin (Jeanette, et al., 2002).

the Cordoba Platform occurred. Where anoxic conditions prevailed, shaly limestones of the Maltrata formation were deposited, and for the open sea conditions the Guzmantla formation was formed. Carbonated bioclastic rocks occured in Coniacian-Santonian at the top of the Guzmantla formation. At Campanian age the Cordoba Platform uplifted, producing erosion of the carbonated formations. In the lowest zones, the San Felipe formation was deposited, represented by shaly limestones and carbonated breccias. For Maaestrichtian bioclastic limestones of Atoyac formation were developed and for the deepest areas shaly limestones, breccias and shales of the Mendez formation were deposited (Salvador, 1987 [8]).

A foreland stage in the basin indicates the change in sedimentation from carbonate to silicilastic rocks during Tertiary. Uplifting and erosion of Cretaceous and Jurassic formations occured during Laramide orogeny. At Paleocene, fine-grained sandstones of the Velasco and Chicontepec formations overlaid Cretaceous rocks. Aragon sandy
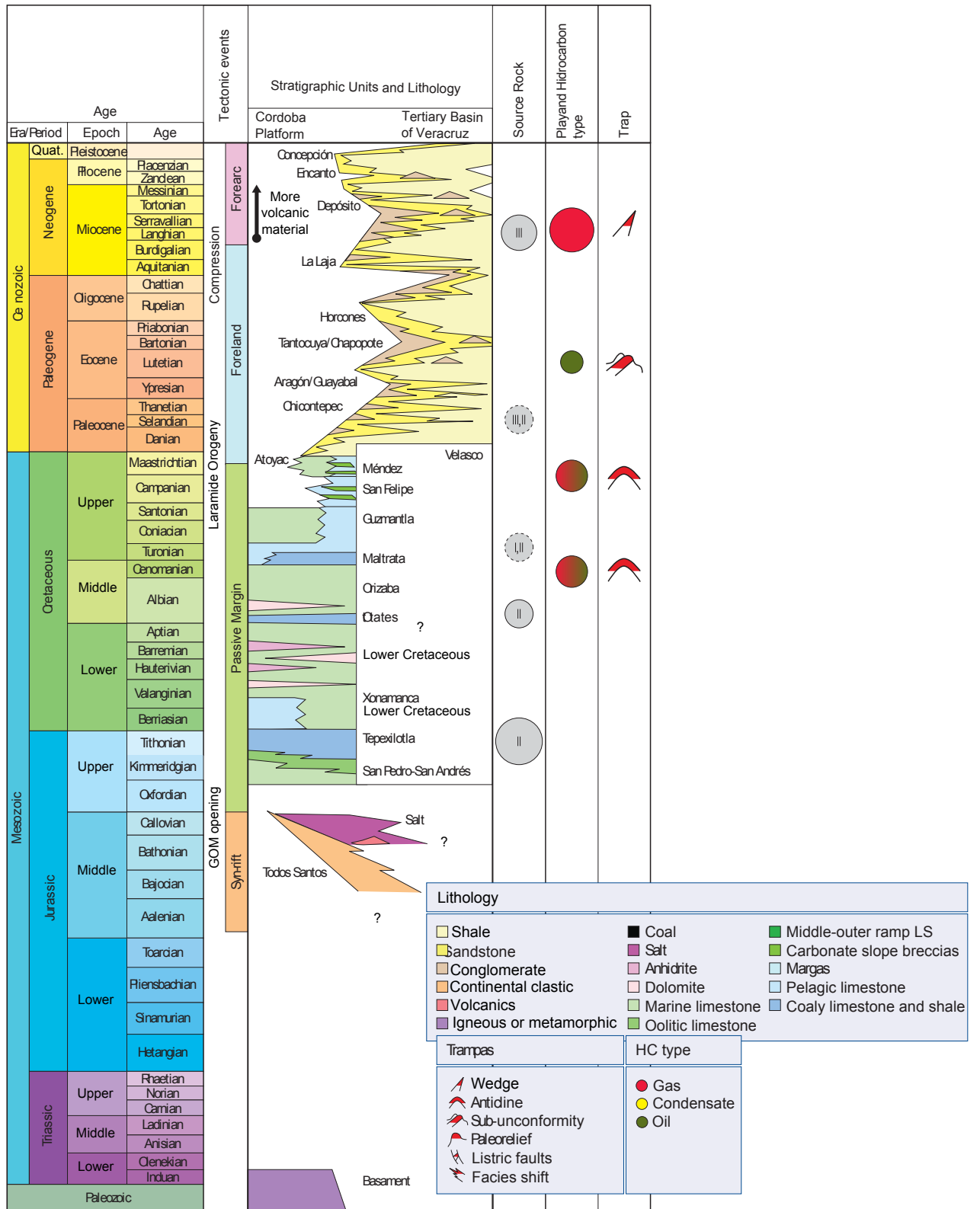
Figure 2.3: Stratigraphic column of the Veracruz Basin (SLB, Descubriendo el Yacimiento, 2010).

and shaly formation were deposited during Lower Eocene. For Middle Eocene flow debris, conglomerates and turbiditic sandstones sedimentation formed the Guayabal formation. Tantoyuca and Chapopote formations were deposited during Late Eocene. The Paleocene-Middle Eocene was affected by the Laramidic folding and faulting. Upper Eocene-Oligocene sediments onlap the unconformity developed over the deformed rocks (Santoyo-Pineda, 1983 [9]; Baldit-Sandoval, 1985 [10]; Escalera-Alcocer, 1985 [11]). The Upper Miocene, Upper Oligocene and Lower Miocene are represented by conglomerate intervals that are part of submarine fans. Late Oligocene sediments are found only in the central and eastern part of the basin (Martínez-Medrano, et al., 2010 [12])

The Miocene-Pliocene deposits have been subdivided in several stratigraphic sequences based on tridimensional seismic and well data. (Jeannette, et al., 2003 [13]; Escalera-Alcocer, 1985 [11]; Cruz-Helú, et al.,1977 [14]; Arreguín-López, 2004 [15]). The forearc tectonic sequence started with the occurrence of the Trans-Mexican Volcanic belt. These intrusive and volcanic rocks resulted in a sediment source from north to northeast, forming progradations from north to south within the basin during Late Miocene and Pliocene (Cruz-Helú, et al., 1977 [14]; Martínez-Medrano, et al., 2010 [12]; Arreguín-López, 2005 [16]). During Late Miocene and Pliocene the uplift of Anegada and Los Tuxtlas limited the sediment flow to the GOM into a narrow zone between these two elements, as is preserved today and that corresponds to the proximity of the river mouth of the Papaloapan river.

2.4   Petroleum geology

The VB has five petroleum systems where three of them are known (Upper Jurassic, Lower-Middle Cretaceous and Miocene) and the other two are hypothetical (Upper Cretaceous and Paleogene) as shown in Fig.2.4. Upper Jurassic source rocks contains type II kerogen, which reached the oil window during the Late Cretaceous-Paleocene and genereted gas during the Eocene-Oligocene. Lower-Middle Cretaceous unit has type II kerogen, reaching the oil window in the Paleocene-Eocene and gas window during the Miocene-Pliocene. Miocene source rocks have immature organic matter and have been generating biogenic gas which is stored in Upper Miocene-Lower Pliocene reservoir rocks.

Thermogenic gas has been migrated through deep faults, unconformities and strati-
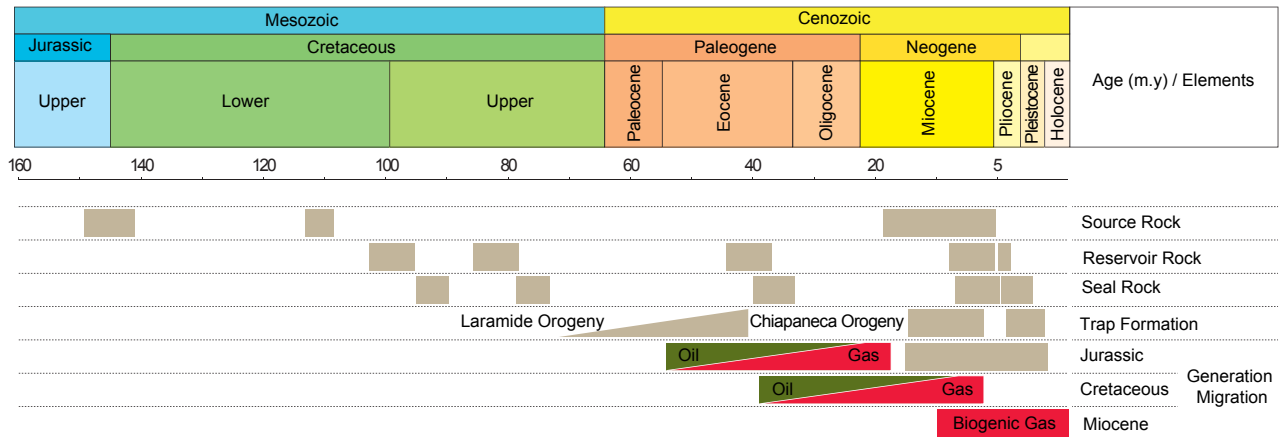
Figure 2.4: Petroleum system event chart of the Veracruz Basin (Vázquez, 2010).

graphic planes from Upper Cretaceous source intervals throughout the Tertiary section. Deepening of the basin and associated tilting and remigration may have occurred throughout the Tertiary. Interbedded shales form hydrocarbons top seals in the Tertiary interval. Most oil in Tertiary rocks is found in Miocene units. Biogenic gas migration has been more local, supplying the sandstones adjacent to the source rocks (González-García, 1992 [17]; Serrano-Bello, et al., 1996 [18]; Talukdar, et al., 2002 [19]).

There are four structural plays in the Tertiary of the VB and one in the Laramide thrust belt (Prost and Aranda, 2001 [2]). Studies indicate a stratigraphic component for some of these plays within the basin:

1. Footwall structures associated with fault-related folds. Hydrocarbons could probably migrated up along faults from a deep source.

2. West-directed hanging-wall, fault-related folds along the same trends.

3. East-directed fault-related folds.

4. The updip corner of tilted fault blocks.

5. The primary structural play in the Laramide thrust belt beneath the westernmost Veracruz Basin is a four-way, hanging-wall, stacked, thrusted fold.

The main reservoir rocks within the VB are the limestones from the Orizaba formation, the carbonate breccias from the San Felipe and Méndez formations, and the

Miocene-Pliocene turbidite sandstones (Meneses de Gyves, 1953 [20]; Martínez, et. al, 2001 [21])

Chapter 3

Theoretical Framework

3.1 Diagenesis

Diagenesis includes a broad spectrum of physical, chemical and biological post-depositional processes by which original sedimentary assemblages and their interstitial pore waters react in an attempt to reach textural and geochemical equilibrium with their environment (Curtis, 1977 [23]; Burley et al., 1985 [24]). As temperature, pressure and chemistry changes through basin history diagenetic processes occur. Diagenesis is differentiated from metamorphism by a temperature range of 180-250 °C which separates the two regimes (Frey, 1987 [25]; Slater, et al., 1994 [26]) as observed in Fig. 3.1 .

3.1.1 Diagenetic regimes

The digenetic processes that occur during the evolution of a sedimentary basin can be divided into diagenetic regimes. Three conceptual regimes are commonly recognized: eogenesis, mesogenesis and telogenesis.

Eogenesis includes all the early diagenesis processes that occur at or near the surface of the sediments where the chemistry of the interstitial waters is controlled mainly by the depositional environment (Berner, 1980 [27]; Chapelle, 1993 [28]). Weathering and soil development in continental depositional settings and bacterially mediated redox reactions in marine environments are included at this stage. Eogenesis can be defined in terms of depth of burial and temperature where the maximum depth limit is about 1-2 km.

Mesogenesis or burial diagenesis occurs during burial. It can be extended to inverted sedimentary basins that experienced certain degree of uplift and cooling. Mesogenesis
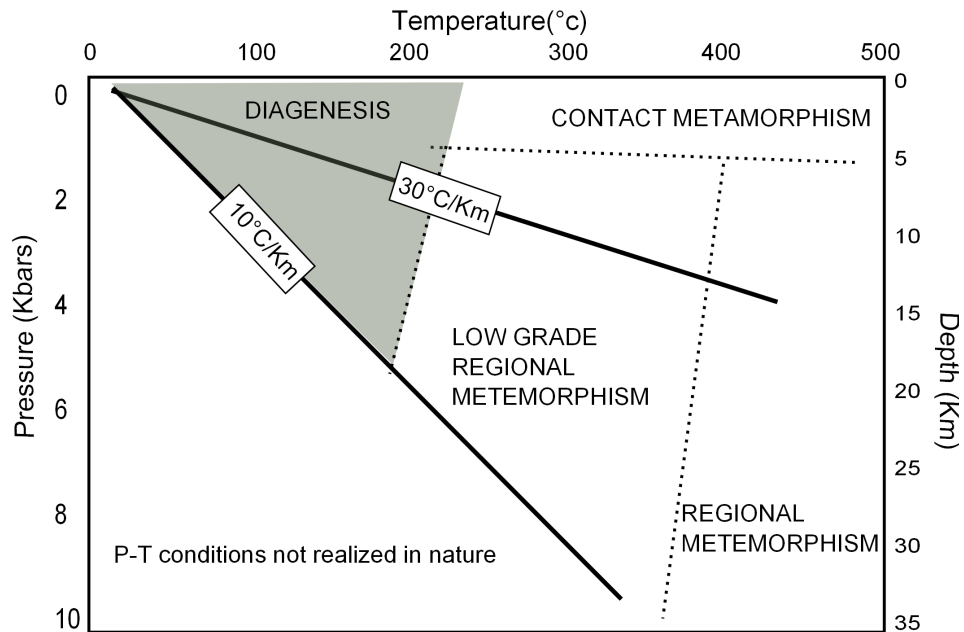
Figure 3.1: Pressure-temperature diagram relating diagenesis to metamorphic regimes (Worden and Burley, 2009).

begins at 1-2 km of burial depth and temperatures between 30 and 70°C (Morad, et al, 2000 [29]).

Telogenesis occurs in uplifted and exhumed rocks that have been exposed to the influx of meteoric water that is not related to the depositional environment of the host sediment. It differs from mesogenesis during moderate inversion and uplift simply because the rocks are in contact with flowing, low salinity, highly oxidized, CO_2-charged waters (Worden and Burley, 2009 [30])

3.1.2 Sand and shale compaction

Compaction is the diagenetic process of decreasing volume reduction and consequential pore-water expulsion within sediments. This is mainly observed in response to vertical shear-compressional stresses owing to increasing weight of overburden. However, this same mechanism can take place under tectonic compressional forces. During early stages of burial, sands loose porosity due to the rearrangement of grains. The amount of porosity loss will depend largely on how well sorted the sand is. In a poorly sorted sand, more

porosity will be lost than in a well-sorted sand (Vesic and Clough, 1968 [31]). During early burial the most damaging processes that affects porosity and permeability are packing change and ductile grain deformation (Surdam, et al., 1989 [64]).

Figure 3.2 shows different compaction curves for sandstones and mudstones. Depositional sand porosities are about 45 % and for muds depositional porosities can be up to 70 % owing to electrostatically bound water and the platy nature of mudflakes (Worden and Burley, 2009 [30]).
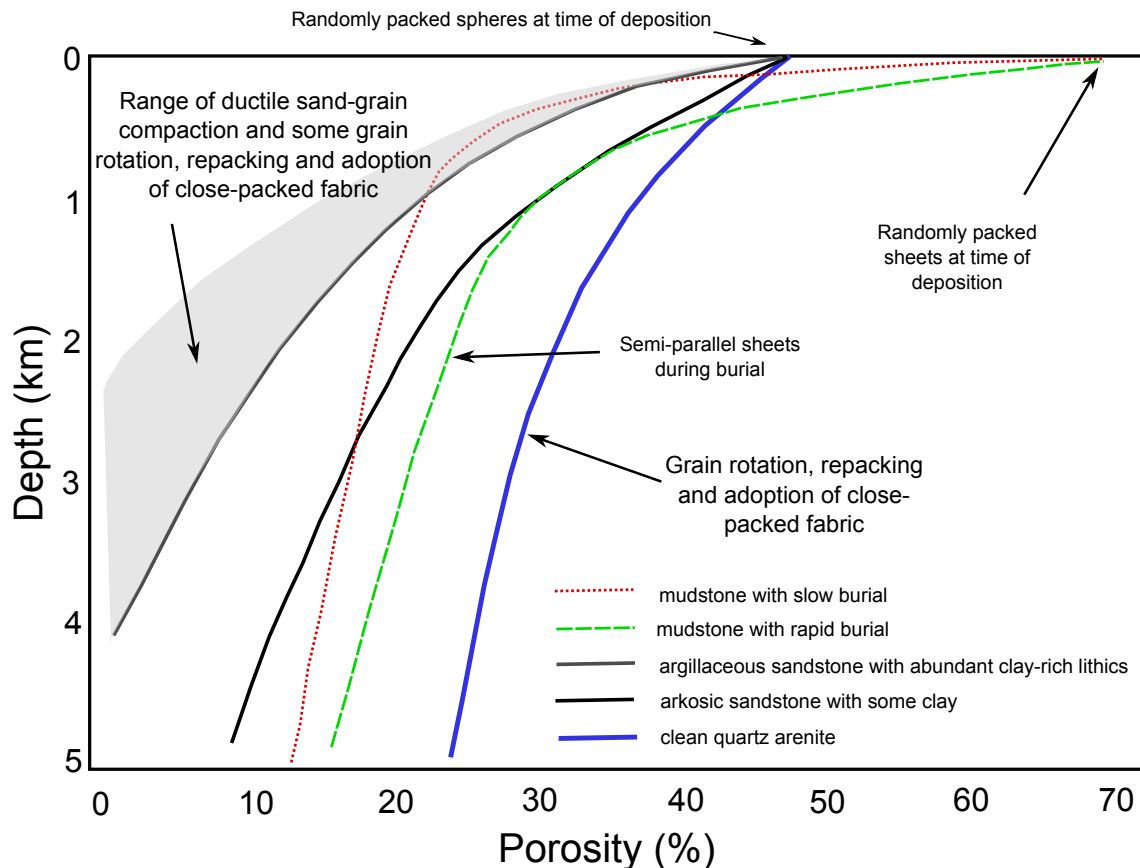
Figure 3.2: Representative compaction curves for sandstones and mudstones (Worden and Burley, 2009).

Sands that contain soft grains, such as glauconite or mica, or those rich in clay content lose porosity much more easily with burial. Kurkjy (1988 [33]) quantified the variation of porosity with depth in these kind of formations with laboratory data.

3.1.3 Sand cementation

Cementation is the diagenetic process by which authigenic minerals are precipitated in the pore space of sediments which thereby become lithified. The most common minerals

cement in sandstones are quartz (and related chalcedonic silica varieties), carbonate minerals, a variety of aluminosilicate clay minerals and zeolites (Worden and Burley, 2009 [30]). Evaporite minerals, other sulfates, sulfides, oxides, feldspar minerals, and other forms of silica can occur widely as cements, but not in volumetric importance.

Quartz cement is the most simple of cements and can occur in a variety of forms. Quartz overgrowths are approximately equal thickness rinds that form on detrital quartz grains (Waugh, 1971 [35]). According to Primmer et al, (1997 [34]) quartz-dominated diagenesis is the main diagenetic style.

Carbonate mineral cements occur in sandstones and can develop during eogenesis and mesogeneisis. Shallow marine sandstones are often cemented with nodules or discrete layers of eogenetic calcite. Marine sandstones develop a wide range of carbonate cements through reaction between detrital aluminosilicate minerals and the products of the breakdown of organic matter. Mesogenesis is characterized by the recrystallization of pre-existing carbonate minerals (i.e. calcite and dolomite) in a ferroan form and results in cement precipitation (Hein, et al., 1979 [36]).

Clay mineral cements are important components of sandstones because of the effect they have on permeability. The most common clay minerals are kaolinite ($Al_2Si_2O_5(OH)_4$), illite ($KAl_3Si_3O_{10}(OH)_2$) and chlorite (($Fe - Mg)_5Al_2Si_3O_{10}(OH)_8$). Smectite family clays can occur as cements, however they are less documented than the others.

3.2 Rock physics interpretation of geological elements

The aim of rock physics is to understand the relation between seismic measurements and rock properties, such as mineralogy, porosity, pore fluids, pore shapes, and pore pressure. A critical part for seismic analysis are rock physics models that relate velocity and impedance to porosity and mineralogy (e.g. shale content)(Avseth, et al., 2005 [42])

In this section the basic rock physics concepts and models used for this project are discussed.

3.2.1 Porosity depth trends

The rate of porosity decrease for sands and shales is more rapid at shallow depths and slows at greater depth of burial (Magara, 1980 [59]). At deposition, shales tend to have

relatively high porosities compared with sands. Sands have depositional porosities of about 40 % and shales depositional porosities could be higher than 80 % (Avseth, 2005 [42]) as shown in Fig. 3.3. This has been observed by several authors who have proposed a number of so-called compaction curves for sandstones and shales (Baldwin and Butler, 1985 [61]; Magara, 1980 [59]; Ramm and Bjørlykee, 1994 [60]).
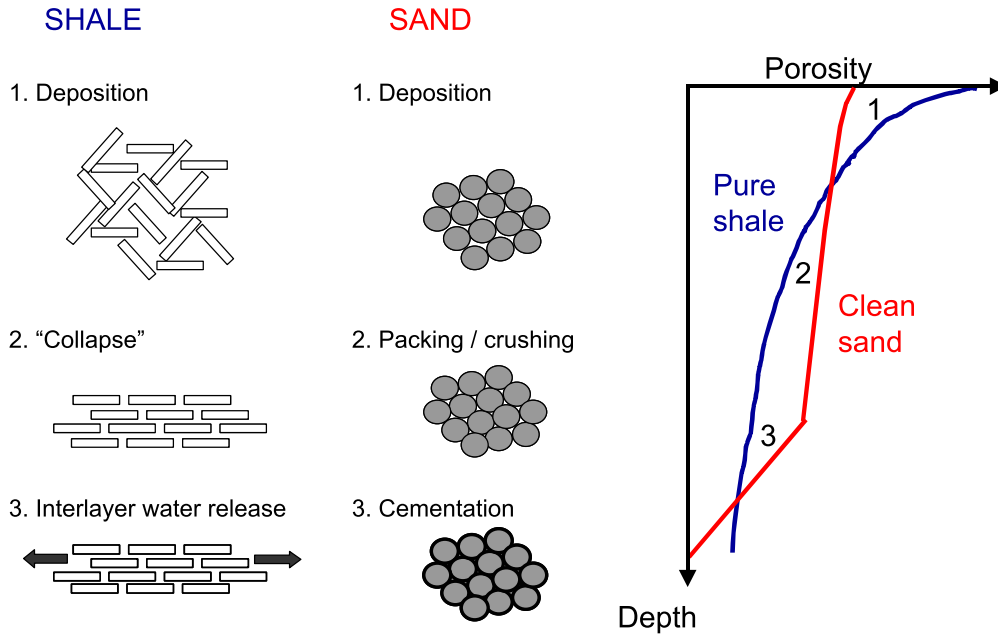
Figure 3.3: Schematic illustration of porosity-depth trends for sand and shales (From Avseth, et al., 2005)

Rubey and Hubbert (1959 [62]) proposed an exponential function to porosity change with depth as:

$$\phi = \phi_0 \cdot e^{-cZ} \tag{3.1}$$

where ϕ is the porosity at depth Z, ϕ_0 is the depositional porosity (i.e. critical porosity) at surface ($Z=0$) and c is a constant of dimension (length^{-1}). A clay content-dependent exponential regression model for porosity versus depth of sands was developed by Ramm and Bjørlykke (1994 [60]) which is only valid for the mechanical compaction regime:

$$\phi = A \cdot e^{-(\alpha + \beta C_I)Z} \tag{3.2}$$

where A, α, and β are regression coefficients. Coefficient A is related to initial porosity at the surface, α is a framework grain stability factor for clean sandstones ($C_I = 0$) and

β describes the change with increasing clay index (C_I). The clay index C_I is the ratio of the volume content of total clay (V_{Cl}) to the total volume content of stable framework grains, where quartz grain are assumed (V_{Qz}). C_I is expressed as:

$$C_I = V_{Cl}/V_{Qz} \tag{3.3}$$

Chemical compaction affects the porosity of rocks. Quartz cementation is of great importance in quartz-rich sands because drastically affects porosities, permeability and seismic properties. It can be developed during shallow burial, however is more common to occur at deeper levels associated with pressure solution. This diagenetic process is probably the most devastating to porosity during deep burial (Surdam et al., 1989 [64]). For sedimentary basins, such as in the North Sea and the Gulf Coast, sandstones are subjected to mechanical compaction down to depths about 2.5-3 km. In deeper depths chemical compaction due to pressure solution and quartz cementation will predominate. Ramm and Bjørlykke (1994 [60]) suggested that clean sandstones lose porosity mostly via pressure solution and quartz cementation as follows:

$$\phi = \phi_D - k\,(Z - Z_D) \tag{3.4}$$

where ϕ_D is the porosity at depth Z_D where diagenetic cement starts. The rate at which the cement volume increases with depth is defined by k.

Diagenesis of shales is restricted to mechanical compaction during shallow burial (less than $\sim 80\,^\circ C$). Stable clay fabric tends to develop in the early stages of burial, and remains unchanged during the subsequent burial history, then clay fabrics are relatively independent of depth, and pure shales tend to obtain a nearly constant porosity trend with depth (Sintubin, 1994 [65]).

3.2.2 Velocity depth trends

When interpreting a new area it is important to identify the correct velocity-porosity relation, which usually lead to better results when is combined with log and core data, and the geological model.

For the velocities estimation, bounds on the elastic moduli of rocks provide a useful framework. There are different models that try to describe the elastic behavior of the rocks. In general, for the rock elastic moduli modelling is needed to specify: (1) the

volume fractions of the different constituents, (2) the elastic moduli of the varius phases and, (3) the geometric details of how the phases are arranged relative to each other. Practically, the geometric details of the rock have been never adequately integrated into a model. When it is specified only the volume fractions of the phases and their elastic moduli, without geometric details of their arrangement, then just the upper and lower bounds on the moduli and velocities can be predicted (Avseth, et al., 2005 [42]).

The Voigt and Reuss bounds

Voit (1910 [52]) and Reuss (1929 [53]) are the simplest upper and lower bounds respectively. The Voigt upper bound on the effective elastic modulus, M_V, of a mixture of N material phases is:

$$M_V = \sum_{i=1}^{N} fi \cdot Mi \tag{3.5}$$

where fi and Mi are the volume fraction and the elastic modulus respectively of the ith constituent. This is the stiffest bound which is the arithmetic average of the constituent moduli. For this bound is assumed all the constituents have the same strain, then it gives the ratio of average stress to average strain and is sometimes called the isostrain average.

The Reuss lower bound of the effective elastic modulus (M_R), is:

$$\frac{1}{M_R} = \sum_{i=1}^{N} \frac{fi}{Mi} \tag{3.6}$$

This is the softest bound which is the harmonic average of the constituent moduli. For this bound is assumed all the constituents have the same stress, then it gives the ratio of average stress to average strain and is sometimes called the isostress average.

For both Voigt and Reuss formulas, M can represent any modulus. However, it is more common to calculate this bounds averages of the shear modulus, μ and the bulk modulus, K, and then compuet the other moduli appling the rules of isotropic linear elasticity.

3.2.3 Rock physics models

As discussed in 3.2.2, if velocity of a rock is predicted only with the porosity, the mineralogical composition, and the elastic moduli of the constituents, the best estimations can

be made are the upper and lower bounds of the velocities. If the geometric details of how the mineral grains and pores are arranged relative to each other, more accurate seismic properties can be predicted.

The rock physics models are the link between rock physics properties and sedimentary microstructure. The rock physics diagnostic technique was introduced by Dvorkin and Nur (1996 [54]) to infer rock microstructure from velocity-porosity relations.

For this thesis project the friable- (unconsolidated) sand model was applied for the rock physics modelling, and it is discussed in the next section.

The friable-(unconsolidated) sand model

This high-porosity model introduced by Dvorkin and Nur (1996 [54]) describes the velocity-porosity change with sorting at a specific effective pressure. The "well sorted" end member is represented as a well-sorted packing of similar grains whose elastic properties are determined by the elasticity at the grain contacts. Typically, the "well sorted" end member has a critical porosity, ϕ_c around 40 %. The variation of the model represents poorly sorted sands as the "well sorted" end member is modified with additional smaller grains deposited in the pore space. This additional smaller grains deteriorate sorting, decrease porosity, and only slightly increase stiffness of the rock.

The elastic moduli of the dry well-sorted end member at critical porosity is given by the Hertz-Mindlin theory (Mindlin, 1949 [55]) as follows:

$$K_{HM} = \left[\frac{n^2 \cdot (1 - \phi_c)^2 \cdot \mu^2}{18 \cdot \pi^2 \cdot (1 - \nu)^2} \cdot P \right]^{\frac{1}{3}} \tag{3.7}$$

$$\mu_{HM} = \frac{5 - 4\nu}{5 \cdot (2 - \nu)} \left[\frac{3 \cdot n^2 \cdot (1 - \phi_c)^2 \cdot \mu^2}{2 \cdot \pi^2 \cdot (1 - \nu)^2} \cdot P \right]^{\frac{1}{3}} \tag{3.8}$$

where K_{HM} is the dry bulk modulus, and μ_{HM} is the shear modulus, both at critical porosity ϕ_c ; P is the effective pressure (i.e., the difference between the overburden pressure and the pore pressure); μ and ν are the shear modulus and Poisson´s ratio of the solid phase; and n is the coordination number (the average number of contacts per grain).

The effective pressure versus depth is obtained as:

$$P = g \int_0^Z (\rho_b - \rho_{fl}) \, dz \tag{3.9}$$

where g is the gravity constant, and ρ_b and ρ_{fl} are the bulk and the fluid density respectively, at a given depth, Z.

Murphy (1982 [56]) shown that the coordination number, n, depends on porosity. The following empirical equation gives an approximation between coordination number and porosity:

$$n = 20 - 34 \cdot \phi + 14 \cdot \phi^2 \tag{3.10}$$

The bulk (K) and shear (μ) moduli of the mineral are the other end point of the model at zero porosity. The moduli of the poorly sorted sands with porosities from 0 to ϕ_c are "interpolated" between the mineral point and the well-sorted end memeber using the lower Hasihin-Strikman (1963 [58]) bound.

At porosity ϕ the concentration of the pure solid phase in the rock is $1 - \phi/\phi_c$ and that of the original sphere-pack phase is ϕ/ϕ_c. Therefore, the bulk (K_{dry}) and shear ($\mu_d ry$) moduli of the dry friable sand mixture are:

$$K_{dry} = \left[\frac{\phi/\phi_c}{K_{HM} + 4 \cdot \mu_{HM}/3} + \frac{1 - \phi/\phi_c}{K + 4 \cdot \mu_{HM}/3} \right]^{-1} - \frac{4}{3} \cdot \mu_{HM} \tag{3.11}$$

$$\mu_{dry} = \left[\frac{\phi/\phi_c}{\mu_{HM} + z} + \frac{1 - \phi/\phi_c}{\mu + z} \right]^{-1} - z \tag{3.12}$$

where

$$z = \frac{\mu_{HM}}{6} \cdot \left[\frac{9 \cdot K_{HM} + 8 \cdot K_{HM}}{K_{HM} + 2 \cdot \mu_{HM}} \right] \tag{3.13}$$

After estimating both, dry bulk modulus (K_{dry}) and (μ_{dry}), the saturated elastic moduli, K_{sat} and μ_{sat}, can be predicted from Gassman's equations.

3.2.4 Fluid substitution

Gassman's (Gassmann, 1951 [57]) equations predict how the rock modulus changes with a variation of the pore fluids. The two fluid effects that are considered in the fluid substitution estimation are the change in rock bulk density, and in rock compressibility.

The compressibility of a dry rock can be defined as the sum of the mineral compressibility and an extra compressibility due to the pore space, as follows:

$$\frac{1}{K_{dry}} = \frac{1}{K_{mineral}} + \frac{\phi}{K_{\phi}} \tag{3.14}$$

where ϕ is the porosity, K_{dry} is the dry rock bulk modulus, $K_{mineral}$ is the mineral bulk modulus, and K_{ϕ} the pore space stiffness. In the same way, the compressibility of a rock saturated with a fluid is defined as:

$$\frac{1}{K_{sat}} = \frac{1}{K_{mineral}} + \frac{\phi}{K_{\phi} + K_{fluid} \cdot K_{mineral}/(K_{mineral} - K_{fluid})} \tag{3.15}$$

where K_{fluid} is the pore-fluid bulk modulus. From Eqs. 3.14 and 3.15 Gassman's equations can be expressed as:

$$\frac{K_{sat}}{K_{mineral} - K_{sat}} = \frac{K_{dry}}{K_{mineral} - K_{dry}} + \frac{K_{fluid}}{\phi \cdot (K_{mineral} - K_{fluid})} \tag{3.16}$$

and

$$\mu_{sat} = \mu_{dry} \tag{3.17}$$

Therefore, Eqs. 3.16 and 3.17 predict the modulus for an isotropic rock where the rock bulk modulus will change if the fluid changes, but the shear modulus will not. The dry and saturated moduli, are related to P-wave velocity as:

$$Vp = \sqrt{\frac{K + (4/3) \cdot \mu}{\rho}} \tag{3.18}$$

and S-wave as:

$$Vs = \sqrt{\frac{\mu}{\rho}} \tag{3.19}$$

where bulk density is estimated from:

$$\rho = \phi \cdot \rho_{fl} + (1 - \phi) \cdot \rho_{min} \tag{3.20}$$

where ρ_{min} is the mineral density and ρ_{fl} is the fluid density. For dry rocks, the fluid density is zero.

3.2.5 Rock physics templates

The combination of the depositional trends, rock physics models and fluid substitution in templates or charts is what is known as rock physics templates (RPTs). This technology was first presented by Ødegaard and Avseth (2003 [63]). One of the most common RPTs is acoustic impedance versus Vp/Vs ratio. This kind of analysis starts with log

data and then extends to seismic data (e.g. elastic inversion) for prediction of lithology and hydrocarbons. For the construction of the RPTs, porosity-velocity trends for the expected lithologies are estimated using Hertz-Mindlin contact theory (Mindlin, 1949 [55]) for the high-porosity end member. The other end point is at zero porosity and has the bulk and shear moduli of the solid mineral. The two end points are connected by the modified Hashin-Shtrikman (Hashin and Shtrikman, 1963 [58]) bounds for mixture of two phases. The next step is to calculate the dry rock properties with the rock physics models and apply Gassman´s relations for estimating the brine and hydrocarbon saturated rock properties assuming a uniform saturation.

This RPTs are constructed honoring the local geology of the study area. Lithology, mineralogy, burial depth, diagenesis, pressure and temperature are geological factors that are considered in the creation of these templates.

3.3   Amplitude versus offset

Amplitude variation with offset (AVO) is a technique to evaluate amplitude anomalies called "bright spots". The variation of reflection coefficients with source-to-receiver spacing in seismic data contains information about lithology and pore fluid content of subsurface rocks (Ostrander, 1984 [37]). AVO is directly related to contrasts in acoustic impedance and Poisson's ratio which are related to changes of the in situ fluid saturation. The application of this tool can increase our ability to predict hydrocarbon accumulations, taking into account that there are several factors that should be considered in the interpretation of AVO results including thin bed effects, anisotropy, reflector dip and depth, and inelastic attenuation.

3.3.1   Offset-dependent reflection coefficient

Consider two semi-infinite isotropic homogeneous elastic media in contact at a plane interface. Then, consider an incident compressional plane wave impinging on this interface. A reflection at an interface implicates energy partition from an incident P-wave to a reflected P-wave, a transmitted P-wave, a reflected S-wave, and a transmitted S-wave as shown in Fig. 3.4 . The angles for incident, reflected, and transmitted rays at the boundary are

related to Snell's law as:

$$p = \frac{sin\theta_1}{V_{P1}} = \frac{sin\theta_2}{V_{P2}} = \frac{sin\phi_1}{V_{S1}} = \frac{sin\phi_2}{V_{S2}} \tag{3.21}$$

where V_{P1} and V_{P2} are P-wave velocities, and V_{S1} and V_{S2} are S-wave velocities in medium 1 and 2, respectively. θ_1 is the incident P-wave angle, θ_2 is the transmitted P-wave angle, ϕ_1 is the reflected S-wave angle, ϕ_2 is the transmitted S-wave angle, and p is the ray parameter.
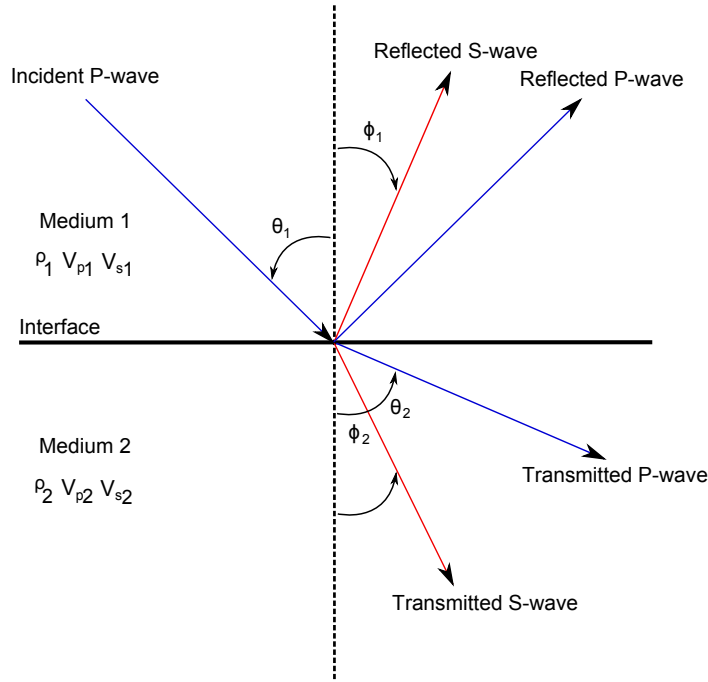
Figure 3.4: Reflected and transmitted waves at an interface between two elastic mediums for an incident P-wave.

At zero offset or normal incidence (Fig.3.5) there are not converted S-waves and the P-wave reflection coefficient R_0 is given by:

$$R_0 = \frac{I_{P2} - I_{P1}}{I_{P2} + I_{P1}} = \frac{1}{2}\frac{\Delta I_P}{I_{PA}} \approx \frac{1}{2} \, ln \, (I_{P2}/I_{P1}) \tag{3.22}$$

where:

$I_P =$ is the continuous P-wave impedance profile

$I_{P2} =$ impedance of medium 2 $= \rho_2 \cdot V_{P2}$

$\rho_2 =$ density of medium 2

$I_{P1} =$ impedance of medium 1 $= \rho_1 \cdot V_{P1}$

$\rho_1 =$ density of medium 1

I_{PA} = average impedance across the interface = $(I_{P2} + I_{P1})/2$, and,

$\Delta = I_{P2}$ - I_{P1}

The logarithmic approximation is acceptable for reflection coefficients smaller than about ± 0.5. The P-wave transmission coefficient at normal incidence T_0 is given by:

$$T_0 = 1 - R_0 \tag{3.23}$$
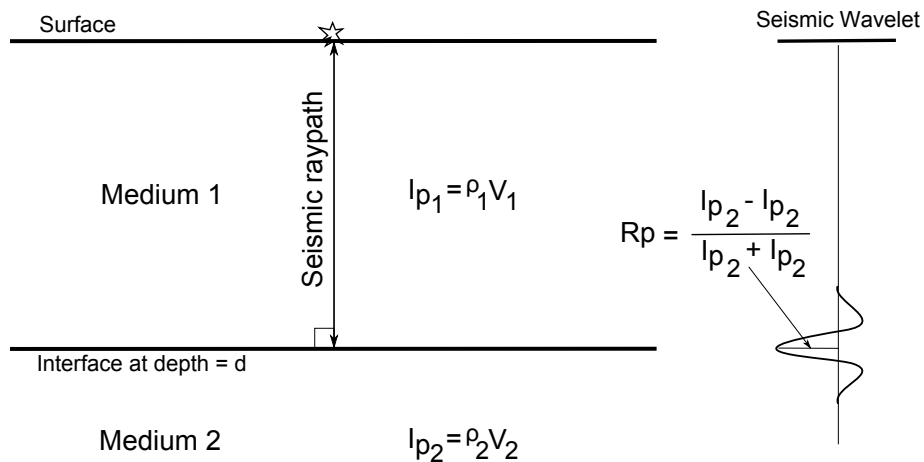
Figure 3.5: Zero-offset reflection coefficient is a product of the contrast of acoustic impedance at the interface of two different elastic mediums.

The offset-dependent reflectivity is the variation of reflection and transmission co-efficients with incident angle and corresponding increasing offset. The traces in a seismic gather reflect from the subsurface interfaces to the surface at increasing angle of incidence θ as shown in Fig.3.6.

The first order approximation to the reflection coefficients as a function of angle is given by adding a second term to the zero-offset reflection coefficient (Eq.3.3.1):

$$R_\theta \approx R_0 + B\,sin^2\,\theta \tag{3.24}$$

where, B is the gradient term which produces the AVO effect and will be discussed further in section 3.3.2. It is dependent on the changes in density, ρ, P-wave velocity, V_P, and S-wave velocity, V_S.
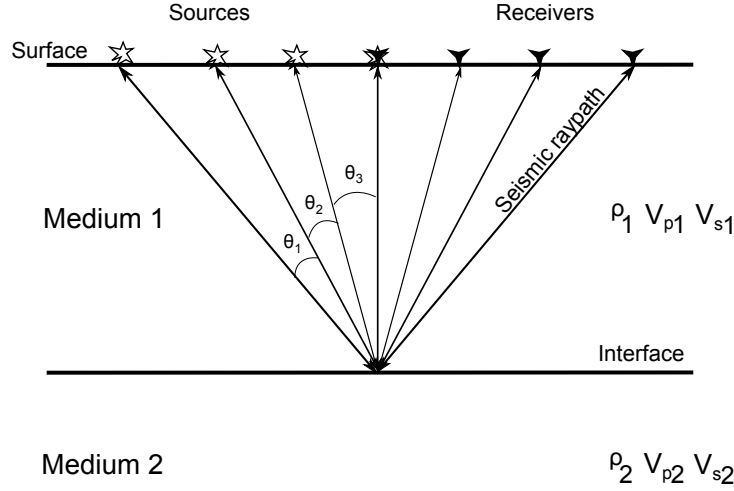
Figure 3.6: AVO effect is produced by a gradient, B, which is dependent on changes in density, P-wave and S-wave velocity at the interface of two elastic mediums.

3.3.2 Approximations of the Zoeppritz equations

The Zoeppritz (Zoeppritz, 1919 [38]) equations describe all possible plane wave reflection and transmissions coefficients at a plane interface as a function of reflection angle. Since these equations are complicated to develop, different approximations have been given by several authors. Aki and Richards (1980 [39]) gave an approximation for the analysis of P-wave reflections assuming weak layer contrasts:

$$R_{\theta 1} \approx \frac{1}{2}(1 - 4\,p^2\,V_S^2)\frac{\Delta\rho}{\rho} + \frac{1}{2\,cos^2\,\theta}\frac{\Delta V_P}{V_P} - 4\,p^2\,V_S^2\,\frac{\Delta V_S}{V_S} \qquad (3.25)$$

where:

$p = sin\theta/V_{P1}$

$\Delta\rho = \rho_2 - \rho_1$

$\Delta V_P = V_{P2} - V_{P1}$

$\Delta V_S = V_{S2} - V_{S1}$

$\theta = (\theta_1 + \theta_2)/2 \approx \theta_1$

$\rho = (\rho_2 + \rho_1)/2$

$V_P = (V_{P2} + V_{P1})/2$

$V_S = (V_{S2} + V_{S1})/2$

In the equations above, p is the ray parameter, θ_1 is the angle of incidence, and θ_2 is the transmission angle; V_{P1} and V_{P2} are the P-wave velocities above and below a given interface, respectively. V_{S1} and V_{S2} are the S-wave velocities , while ρ_1 and ρ_2 are

densities above and below this interface as described in 3.3.1.

Shuey´s (1985 [40]) approximations of the Zoeppritz equations confirm mathematically that the Poisson's ratio is the elastic constant most directly related to the offset-dependent reflection coefficient for incident angles up to 30°:

$$R_\theta \approx R_0 + G\,sin^2\,\theta + F\,(tan^2\,\theta - sin^2\,\theta) \tag{3.26}$$

where

$R_0 = 1/2(\Delta V_P/V_P + \Delta\rho/\rho)$

$G = 1/2\ \ \Delta V_P/V_P - 2\,V_S^2/V_P^2\,(\Delta\rho/\rho + 2\,\Delta V_S/V_S)$

$= R_0 - \Delta\rho/\rho\,(1/2 + 2\,V_S^2/V_P^2) - 4\,V_S^2/V_P^2\ \Delta V_S/V_S$

and

$F = 1/2\ \ \Delta V_P/V_P$

R_0 is the normal-incidence reflectivity, G is the AVO gradient at intermediate offsets and F dominates the variation of the reflection coefficient at far offsets, near to critical angle.

Since pre-stack data for AVO analysis usually is available in angles up to 40°, this simplifies Shuey approximation as follows:

$$R_\theta \approx R_0 + G\,sin^2 \tag{3.27}$$

The contrast in acoustic impedance at an interface controls the zero-offset or incident angle reflection coefficient, R_0, while the gradient G varies with changes in density (ρ), P-wave velocity (V_P), and S-wave velocity (V_S) related to the rock properties. Koefoed (1955 [41]) indicated the importance of the Poisson's ratio or equivalently the V_P/V_S ratio in the offset-dependent reflectivity.

3.3.3 AVO attributes and cross-plot analysis

The two most important AVO parameters are zero-offset resistivity (R_0) and gradient (G) based on Shuey's approximation. These seismic parameters can be extracted, via a least-squares seismic inversion, for each sample CDP gather over a selected portion of a 3D seismic cube (Avseth, et al., 2005 [42]). These attributes can be analyzed by cross-

plotting intercept (R_0) versus gradient (G). This display is a helpful and intuitive way of presenting AVO for a better understanding of the rock properties.

As shown in Fig. 3.7 AVO cross-plot is split up into four cuadrants, where the intercept (R_0) is along the x-axis and the gradient (G) is along y-axis. At the first quadrant (upper right), R_0 and G are both positive values. The 2nd quadrant is where R_0 is negative and G is positive (upper left). The third is where both R_0 and G are negative (lower left). Finally, the 4th quadrant is where R_0 is positive and G is negative (lower right). The quadrant numbers must not be confused with the AVO classes, as will be explained in detail further.
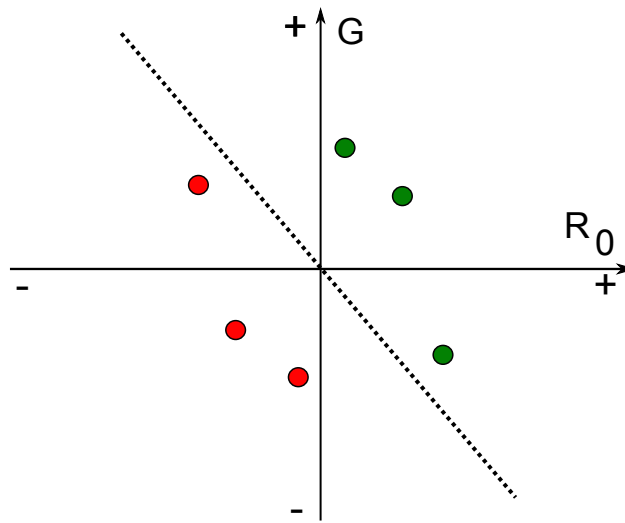
Figure 3.7: AVO cross-plot sketch. Cross-plotting of intercept (R_0) vs gradient (G) can give a better understanding of the rock properties.

Rutherford and Williams (1989 [43]) introduced a classification of AVO characteristics for seismic reflections from the interface between shales and underlying gas sands. This classification is explicitly defined for gas sands and has become the industry standard. Three AVO classes are defined based on where the top of the gas sand is located in a R_0 versus G cross-plot. Table 3.1 summarizes the main characteristics of the different AVO classes. Class I are hard events with relatively high impedance and low V_P/V_S ratio compared with the cap-rock. Class II represent sands with weak intercept but strong negative gradient. Due to the low acoustic impedance contrast between the two layers, this kind of AVO class is often hard to see because they yield dim spots on stacked seismic data. Class III is the AVO category that is commonly related to "bright spots". Ross and Kinman (1995 [44]) distinguished between a class IIp and class II AVO anomaly. Class

IIp shows a weak but positive intercept and negative gradient, causing a polarity change with offset. This class disappears on full stack sections contrary to class II which will show no polarity change and may be observed as a negative amplitude on a full-offset stack.

Table 3.1: AVO classes, after Rutherford and Williams (1989), extended by Castagna and Smith (1994), and Ross and Kinman (1995).

Class	Relative impedance	Quadrant	R_0	G	AVO product
I	High-impedance sand	4th	+	-	Negative
IIp	No or low contrast	4th	+	-	Negative
II	No or low contrast	3th	-	-	Positive
III	Low impedance	3rd	-	-	Positive
IV	Low impedance	2rd	-	+	Negative

In 1997 Castagna and Swan [45] added a class IV AVO anomaly to the Rutterford and William classification scheme. The occurrence of this class is rare, but are produced by low acoustic impedance sands with gas capped by a relatively stiff cap-rock characterized by V_P/V_S ratios slightly higher than in the sands.

The AVO classes cross-plot described above can be observed in Fig. 3.8. These classes were originally defined for gas sands. However, nowadays the AVO class system is used for descriptive classification of observed anomalies that are not necessarily gas sands (Avseth, 2005 [42]).

3.4 Seismic impedance inversion

Seismic impedance inversion is besides AVO, another method for lithofacies identification. In addition to obtain intercept and gradient, pre-stack seismic amplitudes which shows the boundaries between layers can be inverted to obtain reliable estimates of elastic parameters, including V_P, V_S and ρ, which are interval properties useful for geological interpretation. Moreover, impedance inversion take into account the full waveform of the seismic trace, not just the amplitudes. In practice, inversion techniques are used to determine the acoustic impedance, by removing the wavelet that comes form the seismic acquisition and processing stages. The estimated elastic parameters can be linked to rock
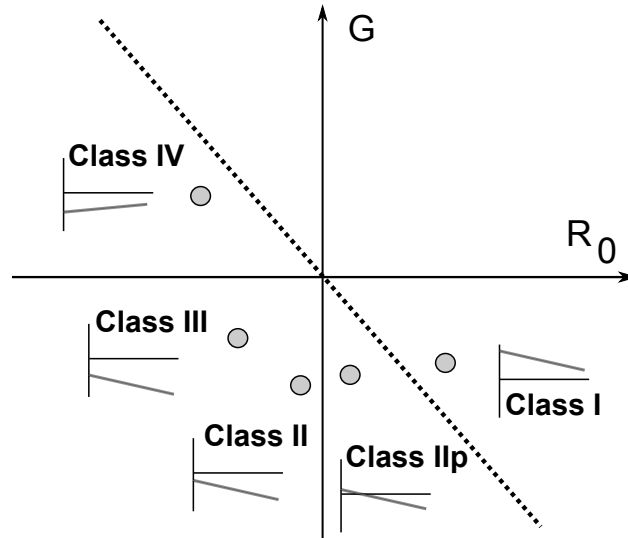
Figure 3.8: Rutherford and Williams AVO classes (1989), originally defined for gas sands (classes I, II and III), along with the added classes IV (Castagna and Smith, 1994) and IIp (Ross and Kinman, 1995) Figure adapted from Castagna et al. (1998)

properties as lithology, porosity and pore fluids, using rock physics models and statistical techniques. The obtained elastic parameters depend on the data and the assumed model. On the other hand, forward modelling takes a model of subsurface acoustic impedance from well logs and convolute it with a seismic pulse or wavelet to create a synthetic trace (Barclay, et al., 2008). Figure 3.9 shows a graphic description of modeling and impedance inversion processes.

3.4.1 Post-stack inversion model

Early impedance inversions were limited to post-stack data, and did not properly take into account wavelet interference. Post-stacked data can be inverted alone for P-wave impedance, and S-wave data is lost. In 1D impedance inversions the seismic trace $S(t)$ is modeled as a convolution of the normal-incidence reflectivity series $r(t)$ with the wavelet $w(t)$:

$$S(t) = w(t) \cdot r(t) \tag{3.28}$$

The normal-incidence reflectivity is defined in terms of the contrast in the acoustic impedance ($I = \rho \ V$) where the approximation holds for small impedance contrasts as:
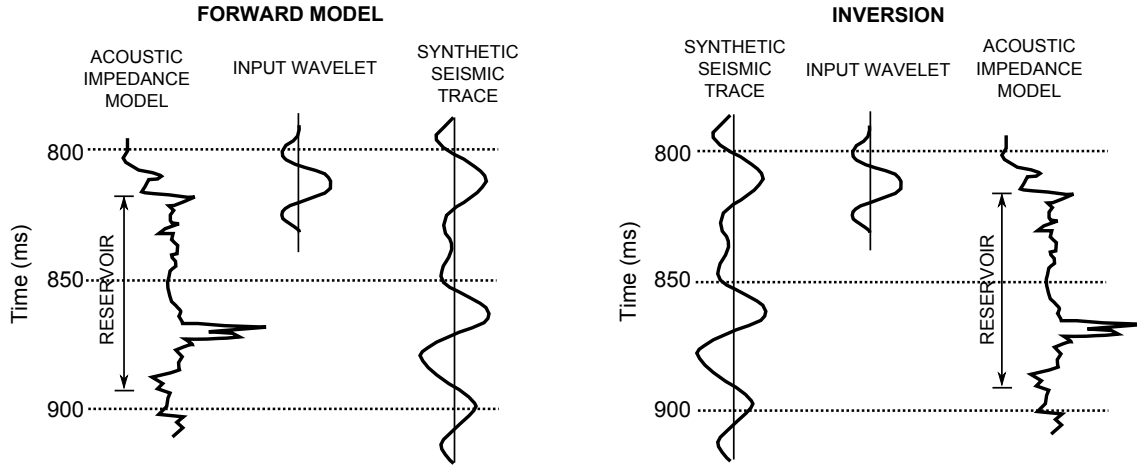
Figure 3.9: Modelling and inversion. The forward modelling (left), takes a model of subsurface acoustic impedance estimated form well logs, combines it with a seismic pulse (wavelet), and obtains as a result a synthetic seismic trace. The inversion (right) begins with a seismic trace recorded and removes the effect of a wavelet estimated to create values of acoustic impedance in each sample of time. (From Barclay, et al., 2008)

$$r = \frac{I_{j+1} - I_j}{I_{j+1} + I_j} \approx \frac{1}{2} d\left(log I\right) \tag{3.29}$$

The first step for the inversion is to tie the well data (sonic and density) to the migrated post-stack seismic data by comparing the synthetic trace calculated with the well logs and the nearest traces to the well location. For the construction of the synthetic trace is necessary the use of a wavelet which is extracted from the seismic data. A robust method is to extract the amplitude spectrum from the seismic autocorrelation and use the well log to estimate an average phase.

Seismic data is band-limited (around 10 Hz to 50 Hz), and therefore lacks of the low and high frequency information which is included in well data. Due to the non-uniqueness nature of the inversion algorithms, there is more than one possible geological model consistent with the seismic data. The next step for the acoustic inversion is to build a prior model which includes the low-frequency (spatial frequency) component of the impedance. This low-frequency trend can be estimated from sonic logs or RMS velocity and provides the information needed for maximize the vertical resolution and minimize tuning effects in the inversion process.

3.4.2 Pre-stack inversion model

As discussed in section 3.4.2, post-stack data inversion estimates only the acoustic impedance ($\rho \, V_P$) and no V_P/V_S ratio information is obtained. On the other hand, with pre-stack data inversion P-wave and S-wave impedances can be estimated.

Simultaneous inversion

Pre-stack is sometimes referred to as simultaneous inversion because the P and S impedances are calculated together with density. It is performed on fully-processed pre-stack data in the angle domain. The process is based on the assumptions that the linearized approximation for reflectivity holds, PP and PS reflectivity as a functions of angle can be given by the Aki-Richards (2002 [39]) as shown in section 3.3.2, and there is a linear relationship between the logarithm of P-impedance and both S-impedance and density, which is expected to hold for the background wet lithologies (Hampson, et al., 2005 [68]).

In the mode conversion described in section 3.3.1, the angle of incidence is greater than zero, and an incident P-wave at an angle θ results in reflected and transmitted P and S-waves. The amplitudes of the reflected and transmitted waves can be computed using the Zoeprittz equations.

Elastic impedance inversion

Elastic impedance (EI) is a far-offset inversion approach which is based on a pseudo-impedance attribute (Mukerji, et al., 1998 [69]). This method contains information about the V_P/V_S ratio and allow us to use the same trace-based zero-offset algorithm for inversion of the far-offset stack as for the near-offset stack, to get an elastic impedance 3D cube. This method can be used to invert data with AVO effects, unlike the post-stack inversion methods. This approach to inversion also uses a wavelet especially for the offset or incident angle allowing a more accurate estimation of the rock properties. The key to using this extracted attribute effectively for quantitative reservoir characterization is calibration with log data (Avseth, et al., 2005 [42]). The acoustic impedance, $I_a = \rho \, V$, can be expressed as:

$$I_a = e^{2 \int R(0) \, dt} \tag{3.30}$$

where $R(0)$ is the normal-incidence reflection coefficient. Similarly, the elastic impedance may be defined in terms of the elastic P-P reflection coefficient at θ, $R(\theta)$, as:

$$I_e(\theta) = e^{2 \int R(\theta)\, dt} \tag{3.31}$$

Substituting in this equation one of the approximations for $R(\theta)$ in terms of V_P, V_S, and ρ contrasts:

$$R(\theta) = R(0) + A\, sin^2\theta + B\, tan^2\theta \tag{3.32}$$

where

$$R(0) = \frac{1}{2}\left(\frac{\Delta V_P}{V_P} + \frac{\Delta\rho}{\rho}\right) \tag{3.33}$$

$$A = -2\left(\frac{V_S}{V_P}\right)^2\left(\frac{2\Delta V_S}{V_S} + \frac{\Delta\rho}{\rho}\right) \tag{3.34}$$

$$B = \frac{1}{2}\frac{\Delta V_P}{V_P} \tag{3.35}$$

I_e can be expressed as:

$$I_e(\theta) = \rho\, V_P \cdot e^{tan^2\theta \int d(lnV_P)} \cdot e^{-4sin^2\theta(V_S/V_P)^2 \int 2d(ln\, V_S)} \cdot e^{-4sin^2\theta(V_S/V_P)^2 \int d(ln\, \rho)} \tag{3.36}$$

or

$$I_e(\theta) = V_P^{(1+tan^2\theta)}\rho^{(1-4Ksin^2\theta)}V_S^{(-8Ksin^2\theta)} \tag{3.37}$$

The benefits of seismic inversion for acoustic impedance are (Savic, et al., 2000 [67]):

- The broader bandwidth of the impedance data maximizes vertical resolution and minimizes tuning effects.

- Interpreting volumes rather than surfaces is more geologically intuitive. It simplifies lithologic and stratigraphic identification, and supports static reservoir models of any complexity.

- Since the data is no longer zero-mean, the dynamic range in any given color display scale is more than doubled, increasing confidence in relatively subtle features.

- Calibrated seismic impedance predicts correlative petrophysical properties like porosity, clay content, and net/gross, throughout the seismic data volume.

Chapter 4

Methodology

The Agua Fría 3D cube and eight exploration wells (Figure 4.1) were selected for an integrated characterization applying a methodology that relates rock physics, AVO analysis and seismic inversion methods for a better understanding of why not all the amplitude anomalies drilled within the area have resulted in hydrocarbon accumulations.
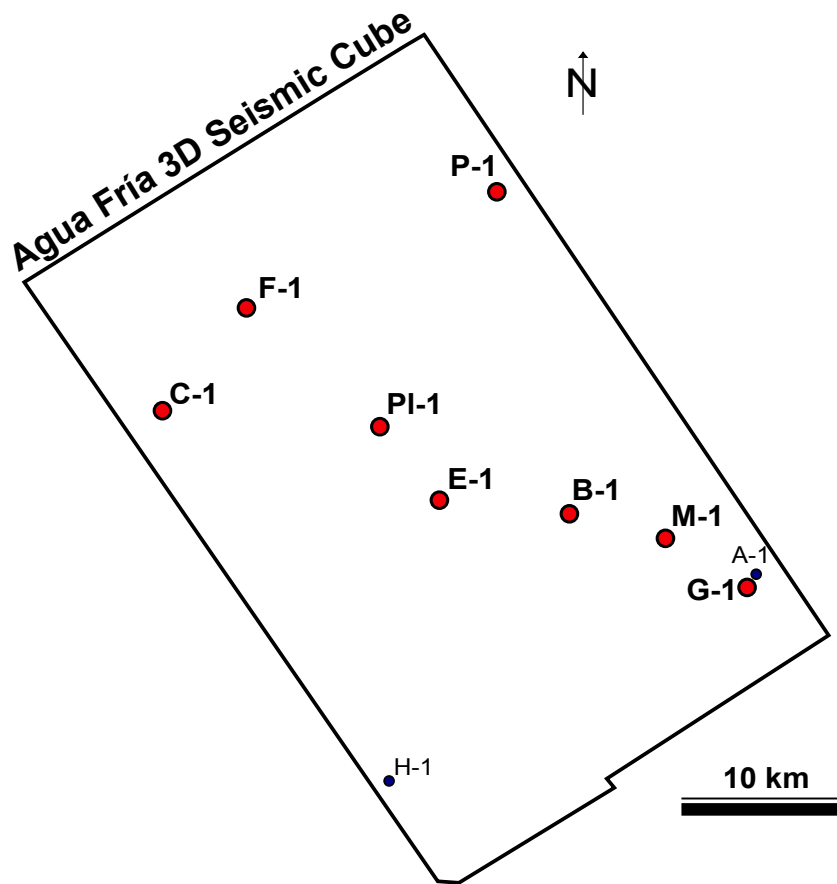
Figure 4.1: Agua Fría 3D seismic cube. Red circles show the selected exploration wells used for this project.

4.1 Software

Two main commercial softwares were used for data displaying, evaluation and analysis.

Interactive Petrophysics 4.1 is a commercial log analysis software with basic and advanced petrophysical modules. This program was used for log plot and cross plot data display. Aditionally, rock physics equations were loaded into the program for velocity estimations.

Hamson & Russel 9 encompasses all aspects of seismic exploration and reservoir characterization, from AVO analysis and seismic inversion to 4D and multicomponent interpretation. This computational program was used for the evaluation, processing and analysis of seismic data.

4.2 Integrated work flow

Figure 4.2 describes the work flow followed for the integrated characterization of Agua Fría 3D seismic cube. Four main stages comprises this work flow and they complement each other in the final integration stage. The methodology applied in this project is described in the next sections following the work flow structure.

4.2.1 Data loading, conditioning and feasibility

At this first stage the objective of the project is established. The inventory of well log and seismic data define if it is sufficient or not for the objective of the project. After data loading and conditioning in the adequate software, a feasibility analysis with well log data is performed to define the strengths and limitations of the proposed methods.

Project objective

Characterize the Agua-Fria 3D seismic cube applying an integrated methodology with rock physics, AVO analysis and seismic inversion methods.

Data inventory

All data used in this thesis project was provided by *PEMEX E & P*. P-wave, S-wave and density log curves availability were the main filters for the exploration wells selection.
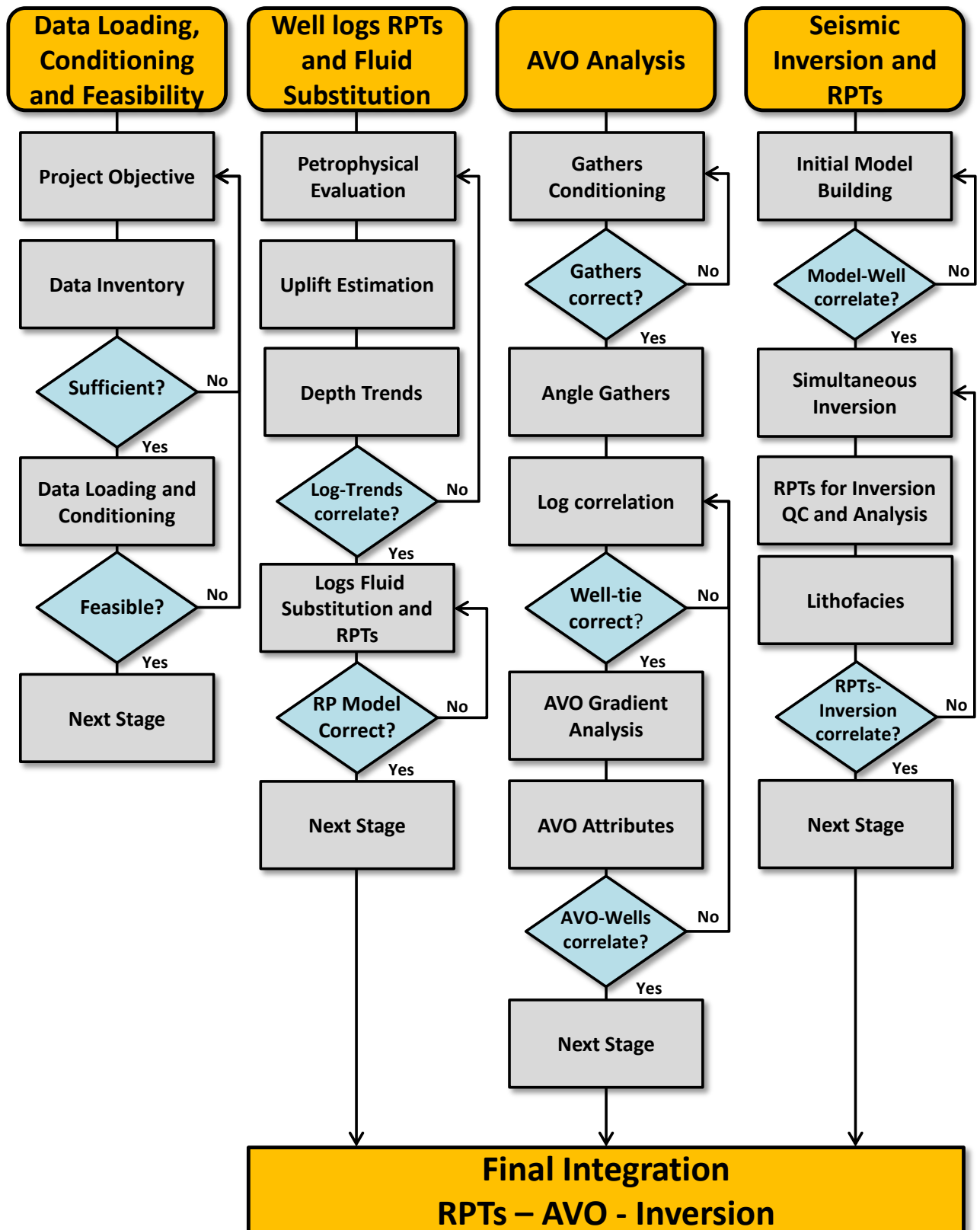
Figure 4.2: Integrated work flow proposed for the thesis project.

The current status of the selected wells is shown in Table 4.1.

Table 4.1: Wells current status

Well	Status
P-1	Dry well
F-1	Dry well
C-1	Dry well
Pl-1	Gas well
E-1	Gas-Oil well
B-1	Gas-Oil well
M-1	Gas-Oil well
G-1	Gas-Oil well

The available data for this thesis project is divided in two groups, well log and seismic data as listed in Tables 5.1 and 4.3 respectively. Modular Formation Dynamic Tester (MDT) pressure points are also available for five wells.

Table 4.2: Well log data for the selected wells.

Well	Well log curves	Core Data
P-1	GR, DTC, DTS, RHOB, NPHI, RT	Helium porosity and permeability
F-1	GR, DTC, DTS, RHOB, NPHI, RT	Helium porosity and permeability
C-1	GR, DTC, DTS, RHOB, NPHI, RT	Helium porosity and permeability
PL-1	GR, DTC, DTS, RHOB, NPHI, RT, MDT	Helium porosity and permeability, petrography
E-1	GR, DTC, DTS, RHOB, NPHI, RT, MDT	Helium porosity and permeability
B-1	GR, DTC, DTS, RHOB, NPHI, RT, MDT	Helium porosity and permeability, petrography
M-1	GR, DTC, DTS, RHOB, NPHI, RT, MDT	Helium porosity and permeability, petrography
G-1	GR, DTC, DTS, RHOB, NPHI, RT, MDT	Helium porosity and permeability

Well log and core data is sufficient for a porosity calibration. Compressional (DTC) and shear (DTS) slowness and density (RHOB) log curves cover almost the entire well depth range which leads to obtain elastic parameters as AI and VpVs ratio in a broad depth interval.

Pre-stack seismic data quality is sufficient for AVO gradient analysis and Simulta-

Table 4.3: Available seismic data from Agua Fría 3D cube.

| Type	Format
Post-stack seismic data with filter	SEGY
Post-stack seismic data with no filter	SEGY
Pre-stack seismic data	SEGY
Regional Velocity Model	ASCII
Regional Interpreted Horizons	ASCII

neous Inversion. The most near offset data seems to be absent, however it is enough for a near partial stacking and for an A (Intercept) volume estimation. Post-stack data with no filters allows the comparison with pre-stack data analysis and it is useful for Acoustic inversion processes. The provided regional velocity model is utilized for the angle gather estimation and the seismic inversion. The five regional horizons are used for acoustic inversion process.

Data loading and conditioning

Well log data was loaded in *Interactive Petrophysics 4.1* for QC and analysis. Log editing and sonic logs spike removal was done. Seismic data, velocity model and regional horizons were loaded in *Hamson & Russel 9* for QC, analysis and processing. CMP gathers conditioning (pre-stack data) is discussed in a further section.

Feasibility analysis

The amount and quality of data allows to make the feasibility analysis to define the uncertainties and limitations for the project. In Fig. 4.3 elastic log data for well B-1 is plotted. The two upper plots shows how low impedance of gas sand allows to separate them from other lithologies. However, oil sands cannot be differentiated just with acoustic impedance variation. The two lower plots S-wave information is added allowing to separate gas and oil sands from other trends. Other lithologies can be identified by these cross plots, in this case, conglomerate that in some intervals fall in the low VpVs ratio and low AI trend. This analysis allowed to understand that S-wave information is critical for fluid differentiation in this project.
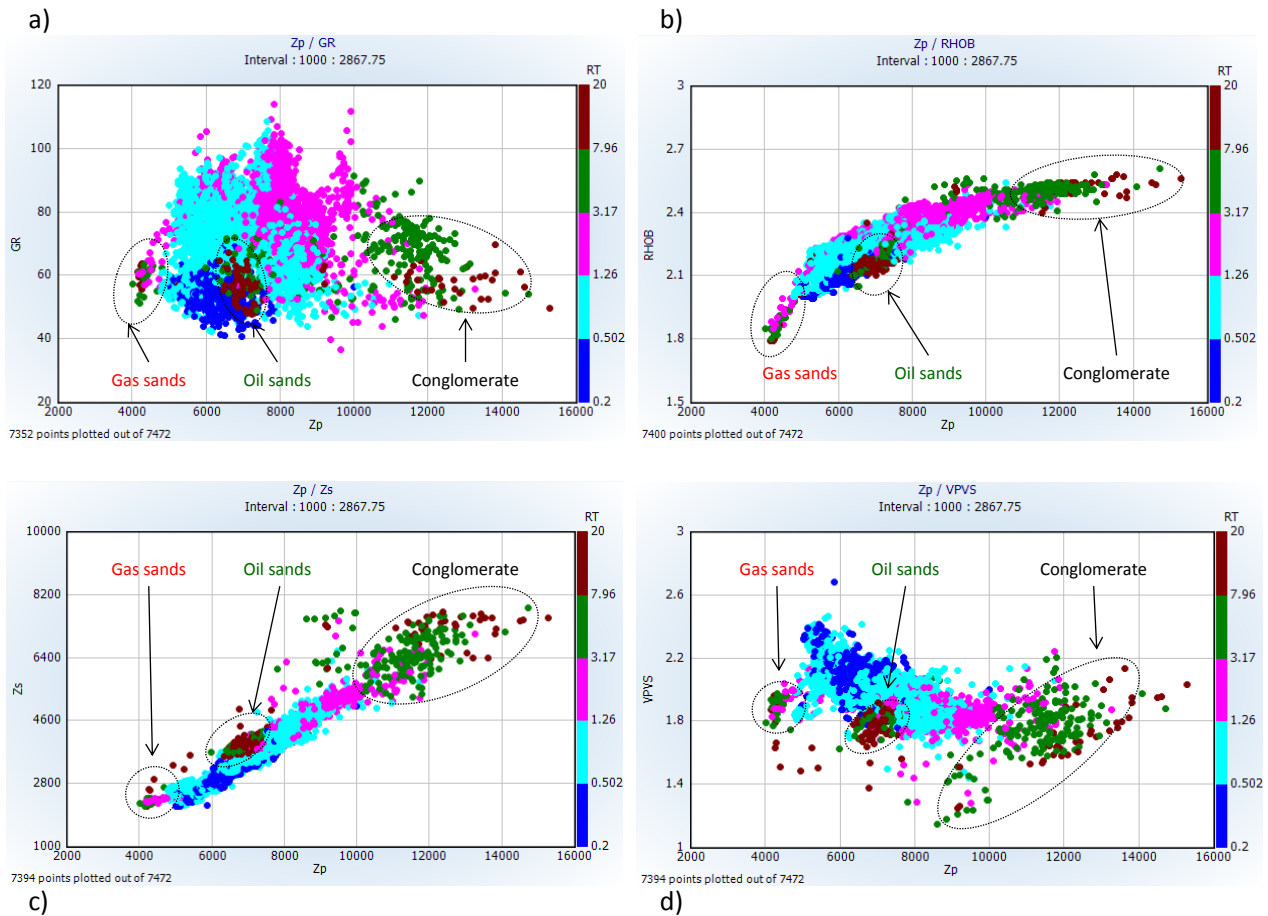
Figure 4.3: Well B-1 feasibility analysis. In a) and b) plots, gas sands can be discriminated using acoustic impedance data. On the other hand, oil sands have same acoustic impedance values as other lithologies. c) and d) plots show how adding S-wave information (Zs) it is possible to differentiate oil sands from other trends. Resistivity (RT) is plotted in the z axis as an aid for hydrocarbon identification.

4.2.2 Well logs RPTs and fluid substitution

Log-core calibration and petrophysical evaluation are done at this stage. Main parameters as water saturation (Sw), clay volume (Vcl) and porosity (Phi) are calculated. Porosity and velocity depth trends are estimated from rock physics (RP) models. Fluid substitution allows to define different trends for RPTs construction and to estimate the change in elastic parameters as acoustic impedance (AI) and VpVs ratio with Sw variations. RPTs define the lithology and fluid trends for well data.

Petrophysical evaluation

At this step Sw is estimated with Archie equation for clean sands (Vcl < 10 %) as follows:

$$Sw^n = \frac{a \cdot Rw}{\phi^m \cdot Rt} \tag{4.1}$$

where n and m are saturation and cementation exponents respectively, and a is tortuosity factor where the three of them are unit less. Rw and Rt are the brine and fluid saturated rock resistivity, respectively. The brine salinity for the study area variates from 55,000 to 120,000 ppm.

Temperature is an important parameter for the petrophysical evaluation as well for defining diagenetic regimes as discussed in section 3.1.1. The geothermal gradient was estimated from the MDT tool temperature measurements of five wells (Figure 4.4).
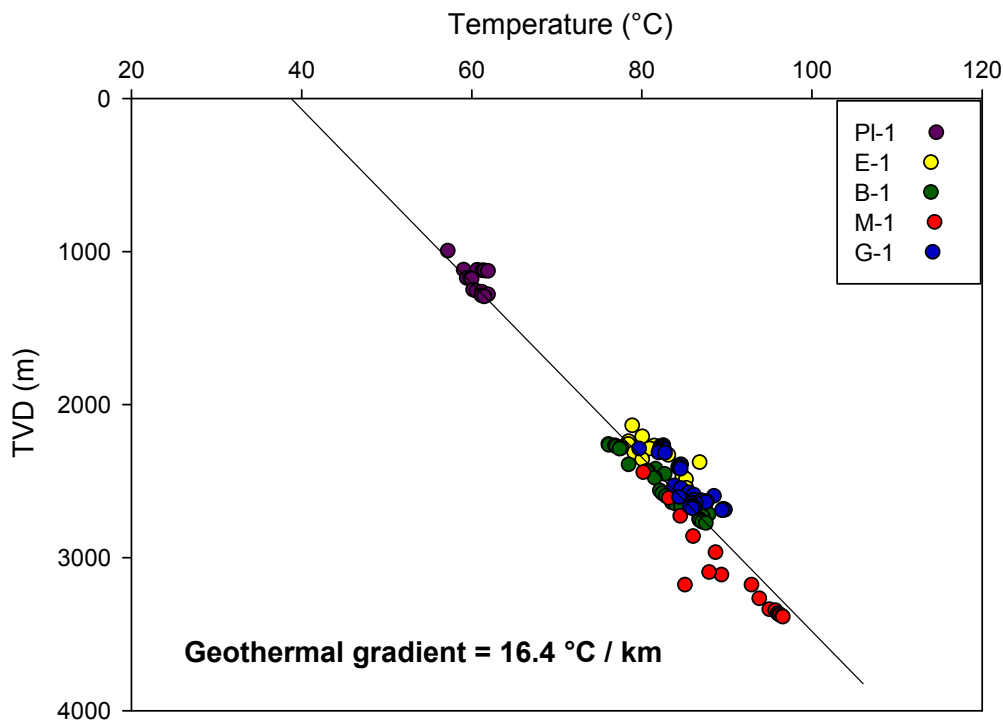
Figure 4.4: Geothermal gradient was estimated with temperature measurements from MDT logging tool.

Porosity depth trends

Porosity-depth functions are derived from Ramm and Bjørlykke (1994 [60]) as discussed in section 3.2.1.

The porosity-depth modeling of mechanical compacted sands is estimated as follows:

$$\phi = 45 \cdot e^{-(0.10+0.27 \cdot 0.1)Z} \tag{4.2}$$

where a porosity at deposition (i.e., critical porosity) is considered to be 45 %. As clean sands are assumed for this trend, $C_I = 0.1$ is used as described by Avseth et al. (2001 [51]).

For shales, a higher critical porosity of 60 % is selected. $C_I = 2$ is assumed due to the lack of mineralogy information (quartz and clay content) for the selected wells in the shale intervals.

Chemical compaction trend is estimated to start about 2235 m in the study area. After uplift correction described in section 4.2.2, the chemical compaction trend become:

$$\phi = 33 - 15 \cdot (Z - 2.235) \tag{4.3}$$

The porosity of 33 % and k = 15 was selected, in order to calibrate the log porosity below 2235 m.

Uplift estimation

There is a difference between the porosity-depth trends estimated in section 4.2.2 and the porosity log data. Since the VB has been subjected to different tectonic events, an uplift during Late Miocene and Pliocene in the area, as described in section 2.2, is assumed to be causing this mismatching.

A shale layer in Middle Miocene was selected in four wells to calibrate the porosity-depth trends for each well. The maximum burial depth was estimated for each well and the Middle Miocene shale was then calibrated to the porosity-depth shale trend. In Fig. 4.5 the plot to the left shows the present burial depth for this shale. The plot to the right shows the maximum burial depth after a depth shift is made to match the porosity shale trend. This depth shift is the estimated uplift the Middle Miocene shale was subjected to, and this same uplift is applied to all the other shale and sand formations along the well.
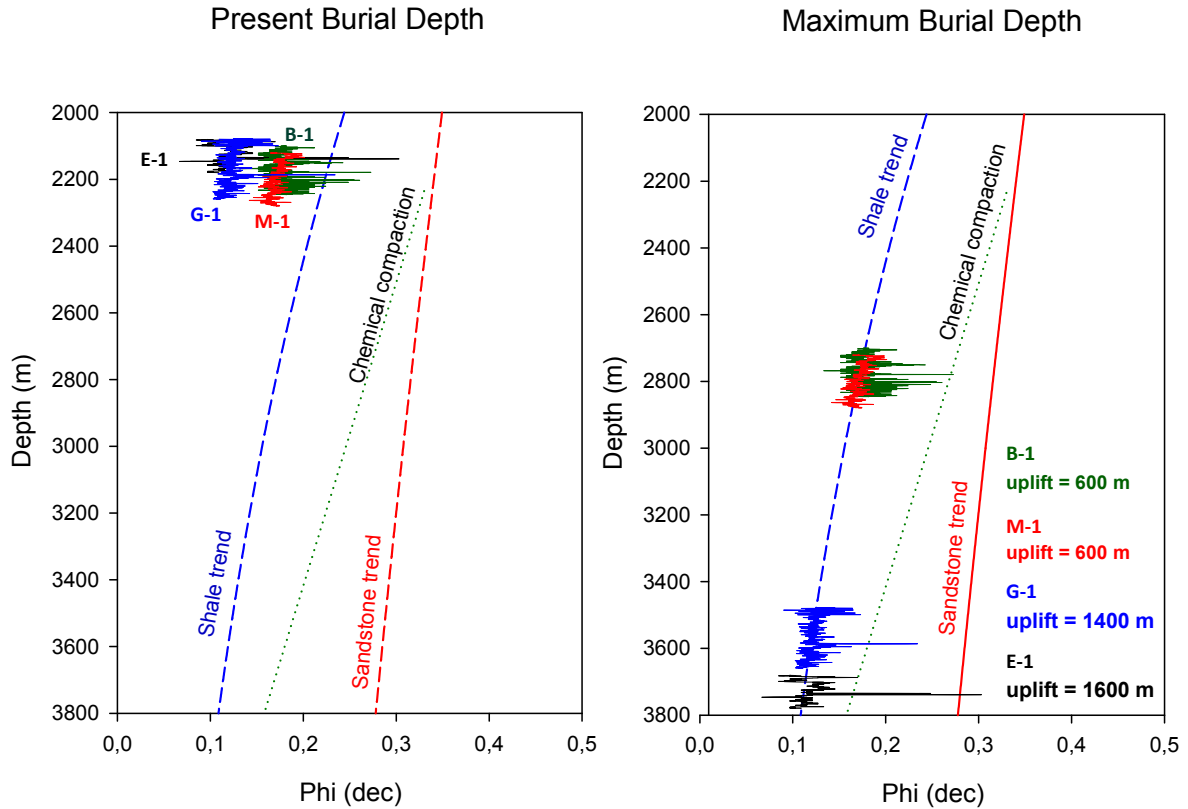
Figure 4.5: The plot to the left shows the Middle Miocene shale for the selected wells and the shale and sandstone porosity trends from Ramm and Bjørlykke (1994). In the right plot, Middle Miocene shale has been depth shifted to match the shale trend in order to estimate the uplift for each well.

Velocity depth trends

As a result of uplift estimation, porosity-depth trends can be calibrated with log measured data (Figure 4.6). The correct determination of these trends is critical for the velocity estimation applying rock physics models.

After porosity-depth trends are calibrated with measured data, velocity-depth trends are estimated using the friable-sand model described in section 3.2.3. Bulk and shear modulus for the dry well-sorted end member at critical porosity are obtained from Hertz-Mindlin theory (1949 [55]) using Eqs. 3.7 and 3.8. Applying Hasihin-Strikman (1963 [58]) bounds (Eqs. 3.11, 3.12 and 3.13) the bulk (K_{dry}) and shear (μ_dry) moduli of the dry friable sand mixture are calculated. The saturated elastic moduli, K_{sat} and μ_{sat}, is predicted from Gassman's relations (Eqs. 3.16 and 3.17). P-wave and S-wave velocities are estimated applying Eqs. 3.18 and 3.19.
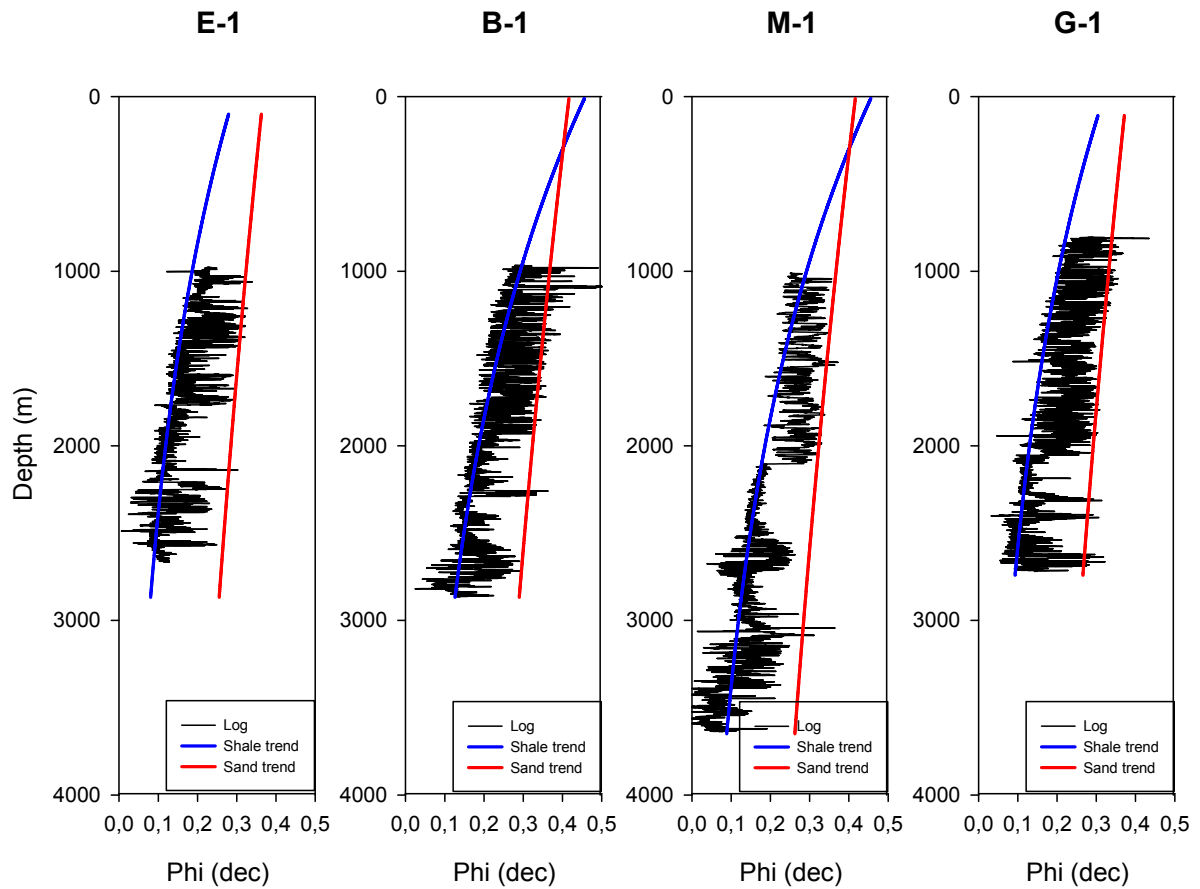
Figure 4.6: A good calibration is observed between the density porosity and the porosity-depth trends for E-1, B-1, M-1 and G-1 wells.

Logs fluid substitution and RPTs

RPTs are constructed as discussed in section 3.2.5 with well log data using the previous depth-trends and RP models. Fluid substitution is performed applying Gassman's relations for the brine and gas trends. The position of the data between these two trends represents the gas saturation (Sg) for a given sand. For this project the selected RPT is presented as a cross plot of AI versus VpVs ratio which includes the RP model, a critical porosity of 45 % and the elastic modulus for fluids and minerals, as described in Table 4.4.

Table 4.4: Mineral and fluid properties for rock physics modelling.

Mineral/fluid	Bulk Modulus (GPa)	Shear Modulus (GPa)	Density (gr/cc)
Quartz	37	44	2.65
Clay	20	10	2.65
Water	2.3	-	1.1
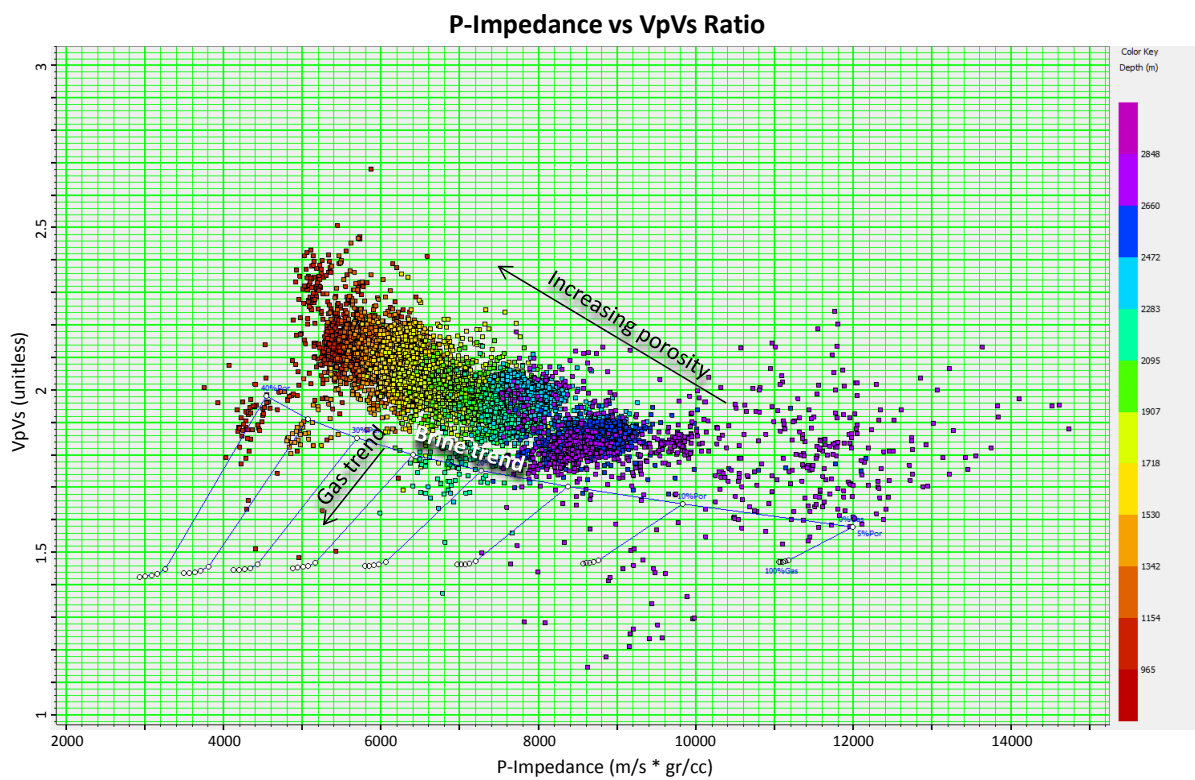
Figure 4.7: Rock physics template (RPT) for well B-1 presented as a cross plot of VpVs ratio vs AI. Trends are included for different lithologies, and increasing gas saturation for sands.

4.2.3 AVO analysis

At this stage, well-tie is done for AVO analysis and further seismic inversion process. AVO gradient analysis is performed to define AVO behavior in the different lithofacies present

in the study area. AVO attributes A (Intercept) and B (Gradient) and their combinations are estimated, cross plotted and mapped.

Gathers conditioning

The most common pre-processing steps before AVO analysis are:

- Spiking deconvolution and wavelet processing

- Spherical divergence correction

- Surface-consistent amplitude balancing

- Multiple removal

- NMO correction

- DMO correction

- Pre-stack migration

    The provided CMP gathers were already conditioned by $PEMEXE\&P$.

Angle Gathers

Both Zoeppritz equations and Shuey's approximations are dependent on the angle of incidence at which the seismic ray strikes the horizon of interest. However, seismic data recording is a function of offset (distance). At this step CMP gathers are converted to angle gathers which are used for the AVO gradient analysis. The definition of the angle interval is done displaying CMP gathers with a color key of incident angle as shown in Fig. 4.8. From this display an angle range from 0 to 50 degrees is selected for the process.

Log correlation

A critical step for AVO analysis and seismic inversion is to correlate well-depth to seismic-time. The depth to time conversion is made through a depth-time table which maps each depth to the two-way travel time from the datum to that depth and back. This time table is calculated from the sonic log, however, is rarely sufficient to define a proper log to seismic tie because some times seismic and log datum are different or the average first layer velocity is not know. Therefore, a manual correlation is done to match events on
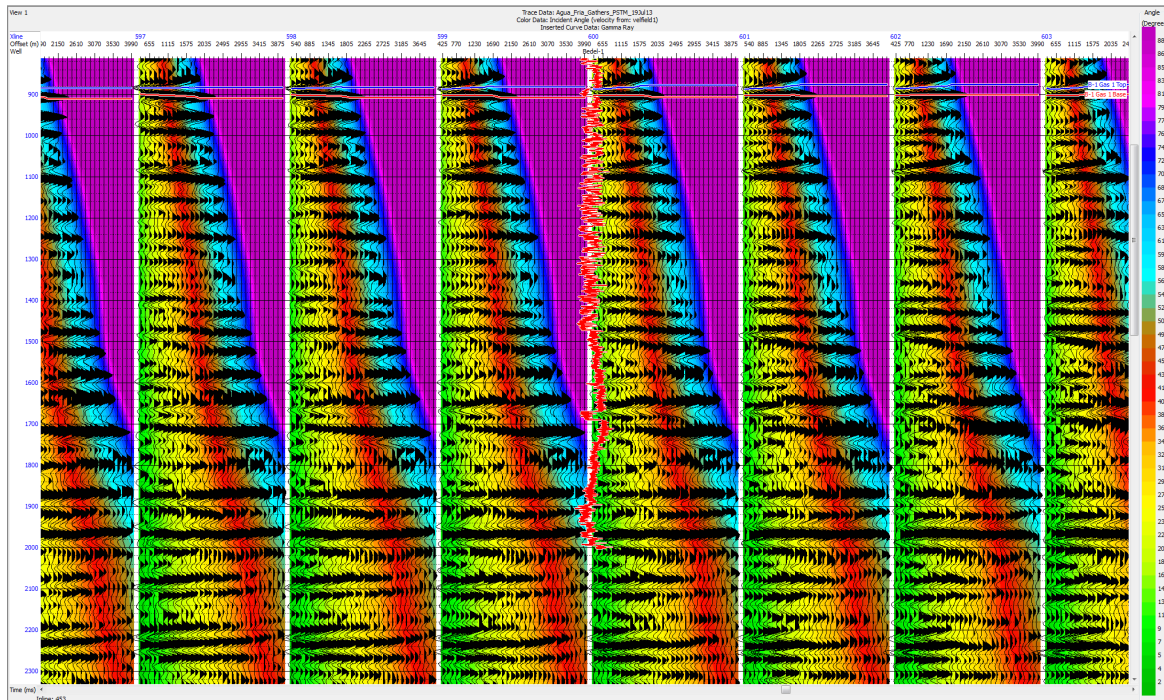
Figure 4.8: Display of CMP gathers with incident angle to define the angle interval for the angle gather process.

a well synthetic with the same events on a seismic trace at a well location. For the well synthetic trace a statistical wavelet is extracted from the seismic data.

A cross correlation is made between lag time and coefficient to know the maximum zero lag coefficient. Table 4.5 lists the maximum coefficients for the selected wells in the study area.

AVO gradient analysis

AVO gradient analysis is a common technique applied in the oil industry for evaluation and interpretation of seismic amplitudes. When the amplitude or reflection coefficient of a seismic reflector is plotted versus offset (or corresponding reflection angle) of the trace, the intercept (A) and gradient (B) are observed. The intercept is at the zero-offset point of the trend and the gradient is the slope of the curve.

For the AVO gradient analysis of the CMP gathers, the two term Aki-Richards

Table 4.5: Maximum coefficient for log correlation in selected wells

Well	Maximum coefficient
P-1	42 %
F-1	23 %
C-1	78 %
Pl-1	53 %
E-1	69 %
B-1	62 %
M-1	51 %
G-1	46 %

(section 3.3.2) equations are used. The amplitude versus offset crossplot is displayed for a certain time event. The analyzed CMP gathers correspond to the locations of the eight selected exploration wells within the Agua Fría seismic cube. Both top and bottom of the selected events are shown in the analysis for comparison of the intercept and gradient in the two interfaces. The main evaluated facies are gas, oil and brine sands.

Other convenient tool for AVO response analysis is the intercept versus gradient cross plot. The points plotted for the selected seismic reflectors allows the comparison with the background data. The position of the points reflects the AVO class type they fall into, as described in 5.4. This AVO intercept and gradient contain information about AI and VpVs ratio obtained form seismic inversion. Both gradient and A versus B cross plots are illustrated in Fig. 4.9 for the top and bottom of a gas sand in B-1 well.

AVO attributes

Other way to analyze AVO data is through AVO attributes. First, A and B volumes are calculated from regression lines obtained from Aki-Richards linear relationship between amplitudes and $sin^2\theta$. From this volumes, AVO product $A*B$ is estimated. This attribute is important for highlighting AVO class III anomalies, since the high negative intercept multiplied by the high negative gradient will result in a high positive value.

Far- versus near-stack data is also a common technique to analyze and interpret pre-stack data. The attributes volumes are created from limited-range stacked section. For this analysis the near stacked volume corresponds a partial stacking of angles from
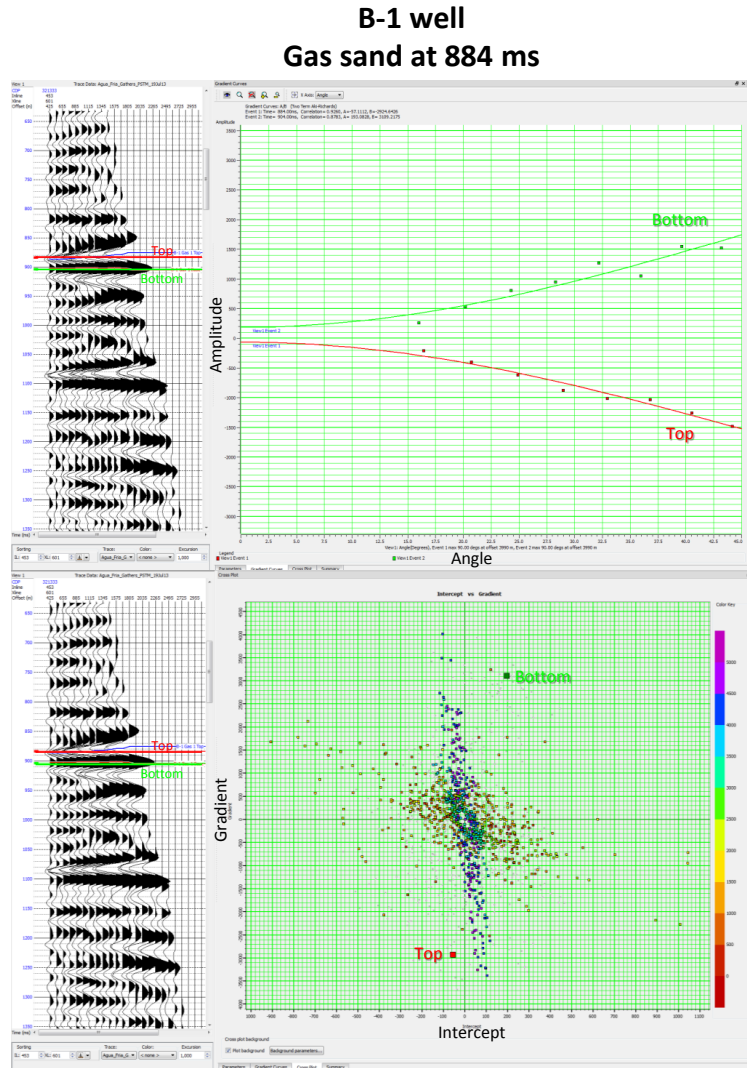
Figure 4.9: Cross plot at the top illustrates an amplitude versus angle plot, useful for AVO gradient analysis. Same data is plotted as gradient versus intercept in the bottom graph.

0 to 15 degrees and for the far stacked data a partial stacking of angles from 20 to 35 degrees. The far stack minus the near stack is a rough estimate of an AVO gradient an is a useful tool for class II AVO anomalies identification. Both attributes, far-near and $A * B$ sections are displayed in Fig. 4.10 for well B-1.

4.2.4 Seismic inversion and RPTs

Prior model building is the first step at this stage before seismic inversion is done. RPTs for inverted data are the quality control and analysis tools mostly used at this stage. Lithofacies are defined using AI and VpVs ratio information from the inverted seismic
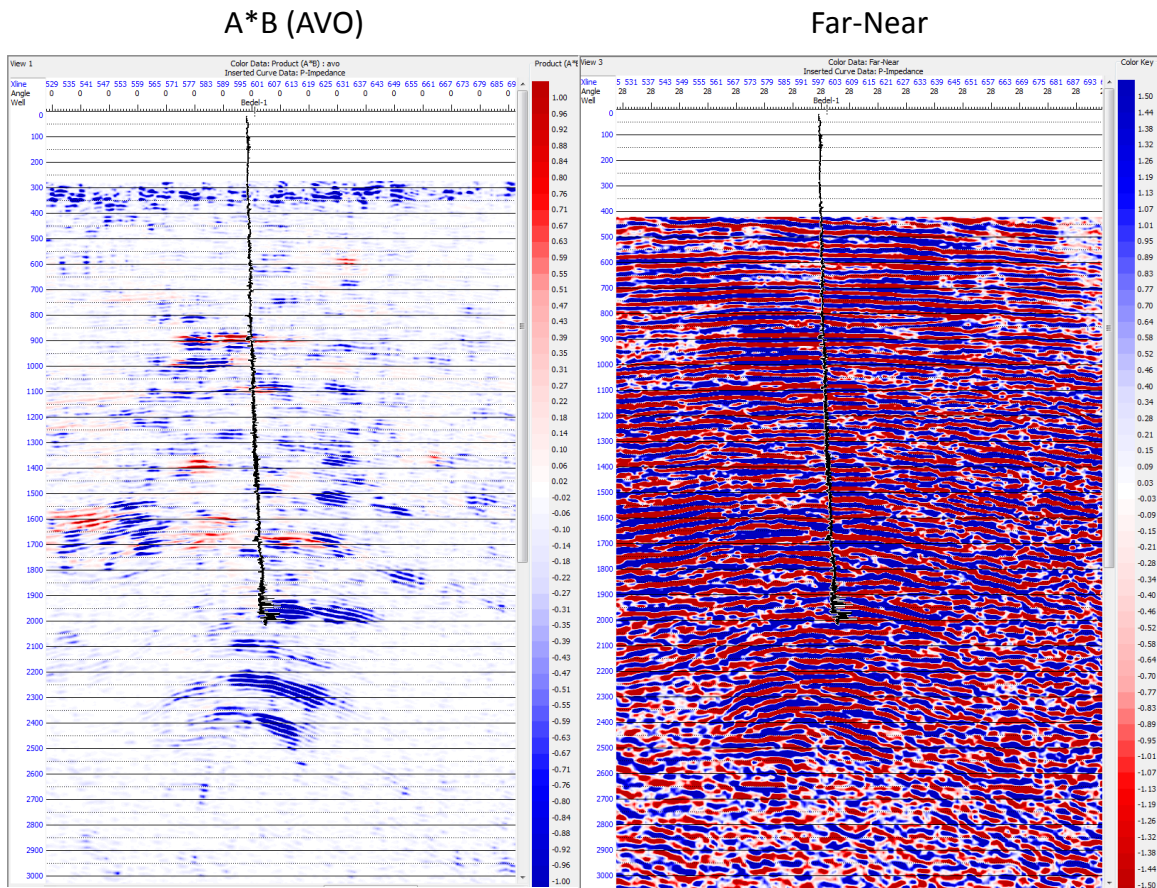
Figure 4.10: AVO attributes.

cube.

Initial model building

As well correlation is already done at the AVO analysis stage, the next step is the model building which includes the selected wells data and the regional horizons. The model consists of three main components, P-impedance, S-impedance and density. The model for the simultaneous inversion is constructed by a initial guess of parameters and iterates towards a solution. For simultaneous inversion, pre-stack data is needed as a set of angle gathers or a set of angle stacks. For this inversion project one set of angle gathers is used.

As a loss of high frequency energy from near to far offsets is expected, two statistical wavelets are extracted from pre-stack data. The first wavelet is extracted from the near angles traces and the second one from the far angles traces.

Simultaneous inversion

After an initial model is constructed, simultaneous inversion is performed at the well locations for QC and calibration of the inversion parameters. A time window from 0 to 3000 ms is set for the process. The two previous extracted wavelets are used in this estimation. Background trends for the three obtained variables, P-impedance, S-impedance and density are used to reduce the non-uniqueness of the inversion process and decrease uncertainty. The synthetic traces estimated from this inversion are compared with the original angle gather to obtain an error gather which is the difference between the two data. Once different parameters are adjusted to minimize this error, the entire volume can be inverted. As a result, P-impedance, S-impedance, VpVs ratio and density volumes are obtained.

RPTs for inversion QC and analysis

The obtained elastic parameters can be plotted with the same RPTs defined with log data. These plots allow to make a quality control (QC) for the inverted data and compare it with the fluid and lithology trends previously defined.

Figure 4.11 is an example of how RPTs are a useful tool to test the inverted data an how fluid and lithology trends can be identified. Interpretation can be enhanced with the combination of RP models and inverted data together.

Lithofacies

Lithofacies from inverted data are defined from RPTs. Maps and cross sections are obtained to define the areal distribution of these facies. Figure 4.12 shows an example of inverted data at well B-1 location. Different lithlogies and fluid trends can be identified with the aid of RPTs.

4.2.5 Final integration

At the final stage RPTs, AVO analysis and seismic inverted data is integrated and interpreted together to define the different elastic seismic responses to the lithofacies present in the study area.
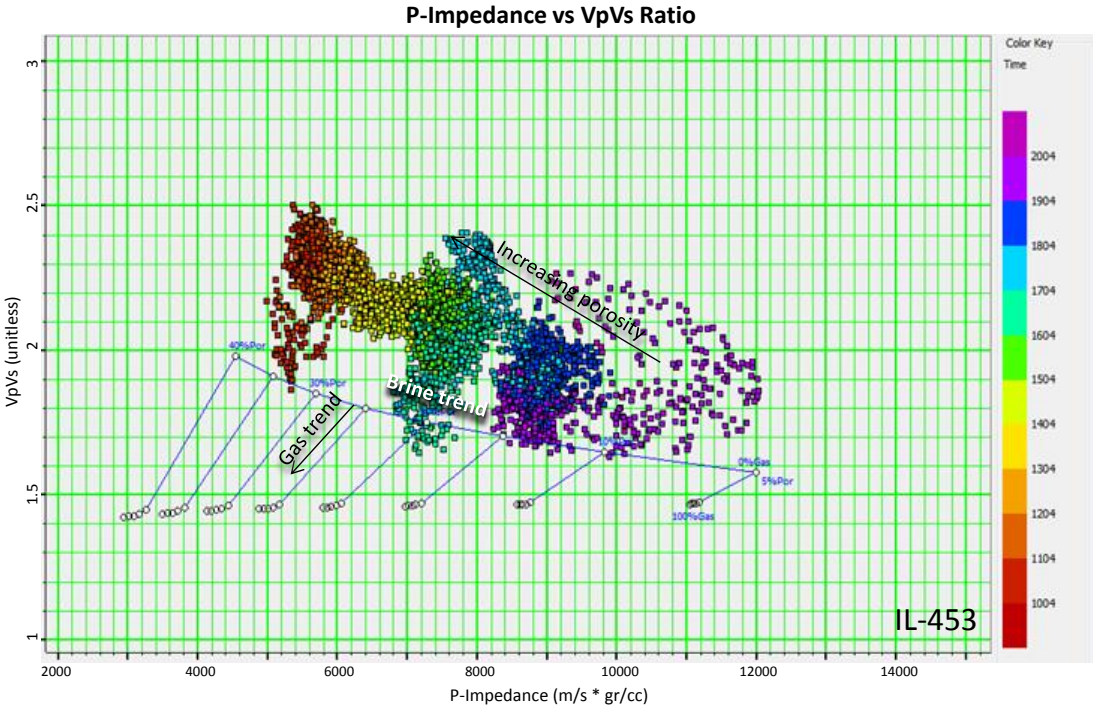
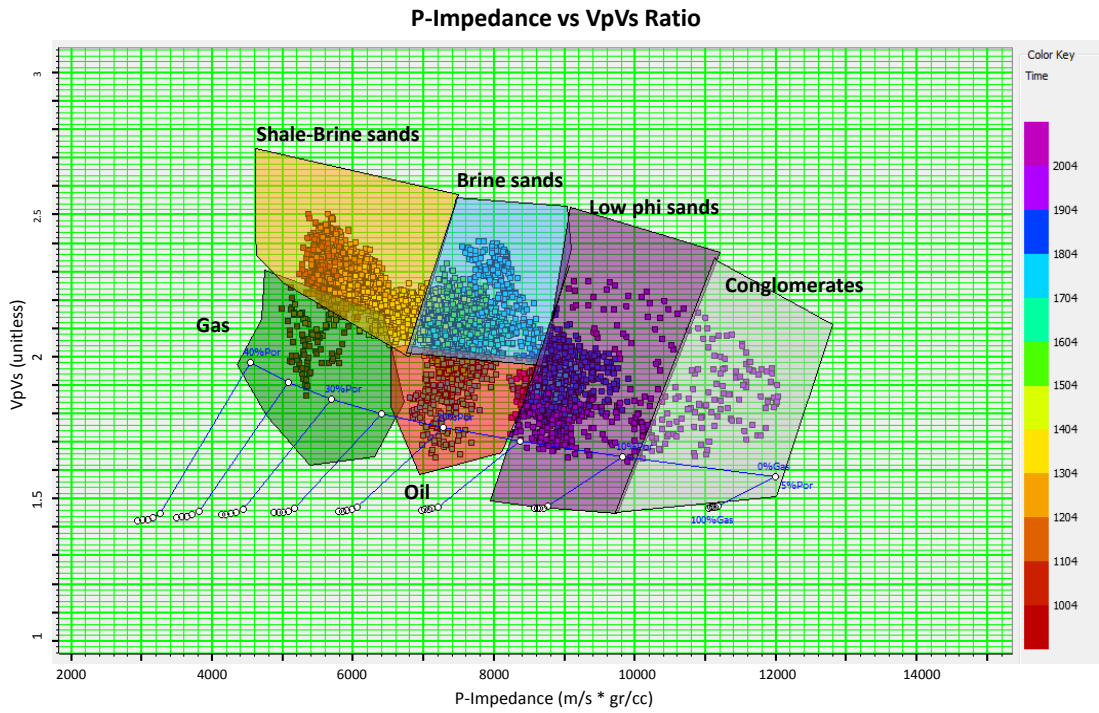**Figure 4.11:** RPTs for QC and analysis of inverted data.

Figure 4.12: Lithofacies form inverted seismic data from B-1 well.

Chapter 5

Results

5.1 Uplift estimation and depth trends

The uplift estimated for the sands and shales southeast of the Agua Fría area varies from 600 to 1600 m. Figure 5.1 shows graphically the maximum burial depth for each well and the present burial depth that is almost the same for all wells. From the plot, wells E-1 and G-1 were buried deeper than M-1 and B-1 wells. Another factor that controls diagenesis is temperature. A low geothermal gradient of 16.4 °C/km is observed for the area compared to the world average geothermal gradient of about 25 °C/km.

P-wave, S-wave and VpVs ratio depth trends are calculated from calibrated porosity-depth trends and rock physics modelling. Figure 5.2 shows the porosity, P-wave velocity and S-wave, and VpVs ratio trends for B-1 well which is representative for the study area.

5.2 Facies classification

Five main facies were identified in the study area: brine sands, oil sands, gas sands, conglomerate, and shale from well log analysis. Wells E-1 and G-1 are the only ones that present the five facies in their drilled interval and they are displayed in Fig. 5.3

5.3 Rock physics modelling

Rock physics models and RPTs defined the fluid, lithology and porosity trends for the study area. The response of elastic parameters as AI and VpVs ratio for different facies,
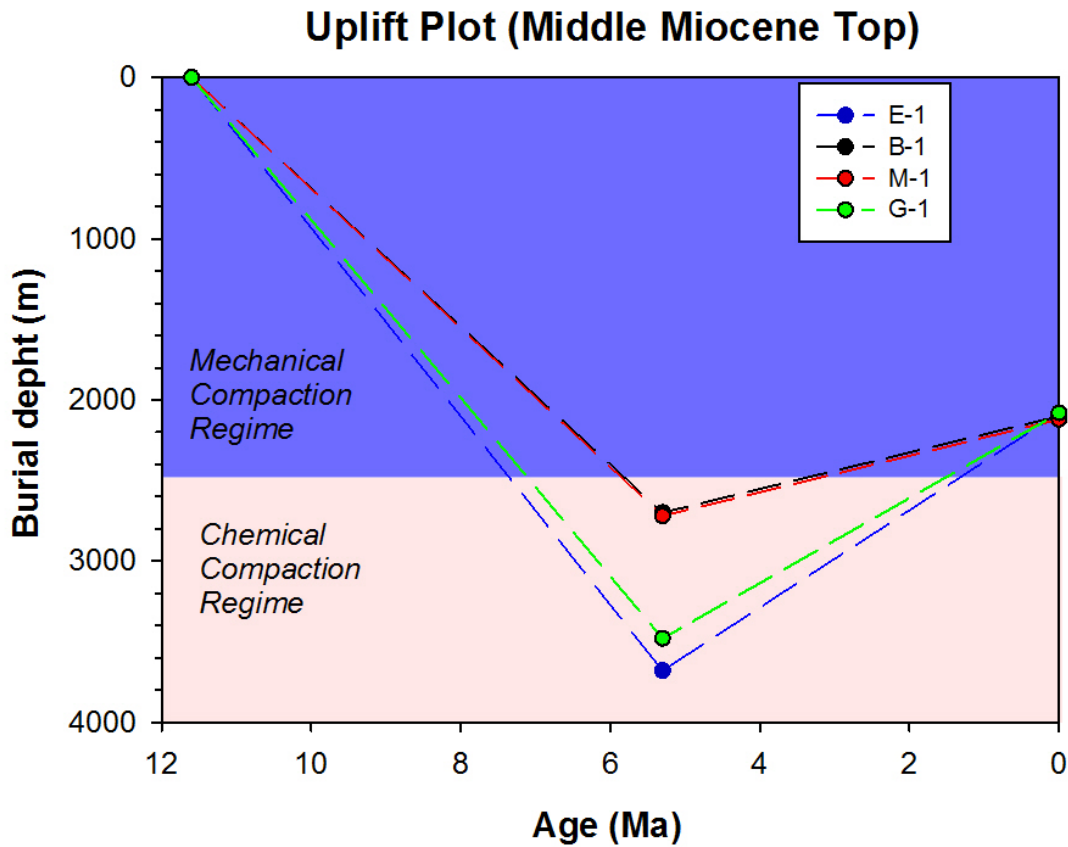
Figure 5.1: The plot shows the burial and uplift of the top of Middle Miocene for the selected wells.

depths and locations can be observed in Fig. 5.4. Table indicate the range of values for AI and VpVs ratio in the selected wells.

Table 5.1: Range of values for AI and VpVs from log data.

Facies	AI $(m/s * gr/cc)$	VpVs ratio $(adim)$
Brine sand	4500 - 8200	1.7 - 2.6
Gas sand	4000 - 9100	1.5 - 2
Oil sand	7000 - 11000	1.65 - 2.15
Shale	5800 - 8800	1.75 - 2.5
Conglomerate	7800 - 13000	1.6 - 2
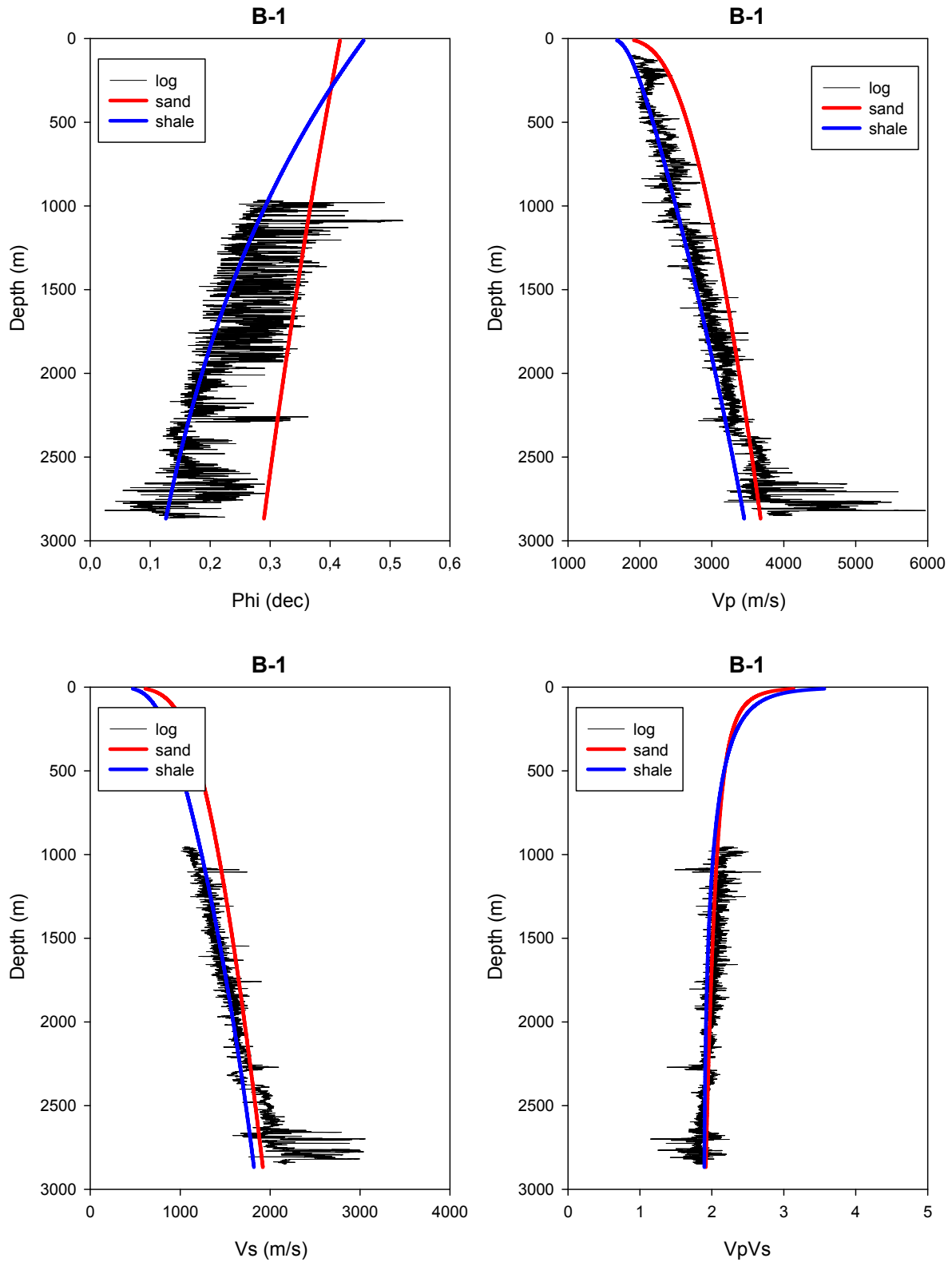
Figure 5.2: P-wave, S-wave and VpVs ratio estimated for B-1 well from porosity-depth trends and RP modelling.
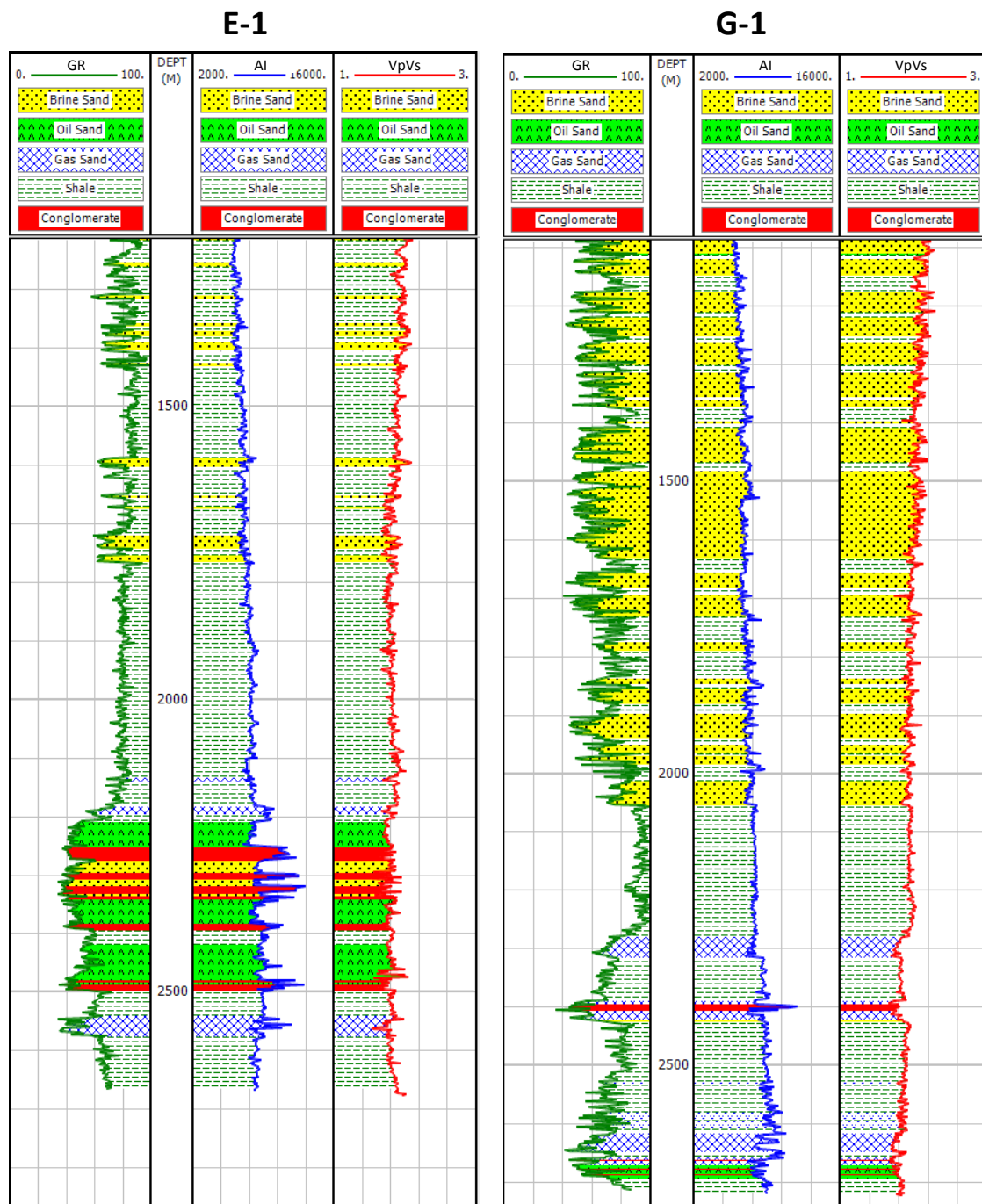
Figure 5.3: Facies classification for E-1 and G-1 exploratory wells. These wells shows the five main facies established for the study area.
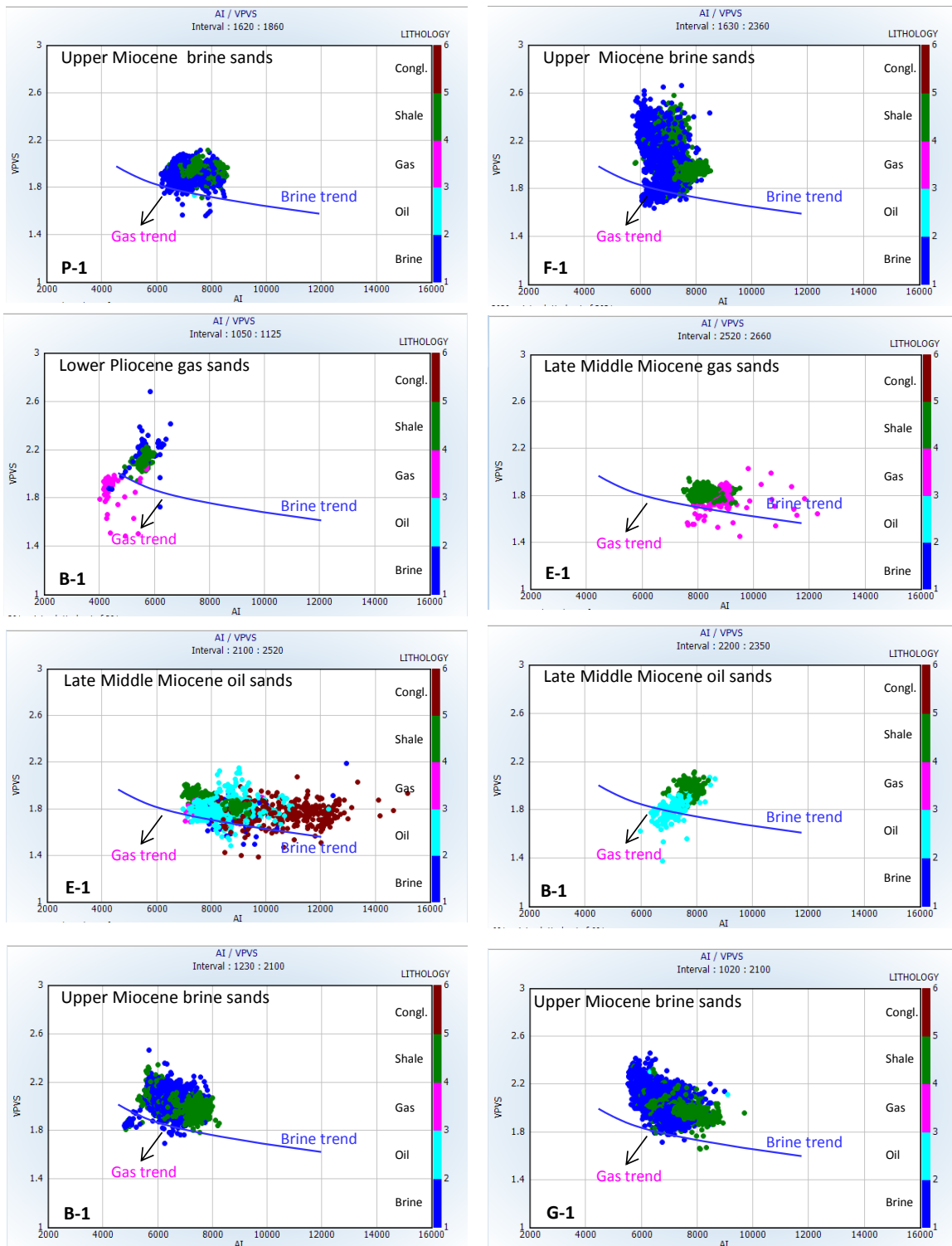
Figure 5.4: RPTs for different facies, depths and locations in the Agua Fría area.

5.4   AVO analysis

Brine, oil and gas sand can respond to a class III AVO response as observed in Fig. 5.5. This is also the most common AVO class anomaly present in area. A high absolute intercept and gradient is at both top and bottom of the sands. From these plots it is observed the lack of near offset data in some CMP gathers. However, this do not affect the intercept and gradient analysis of this facies.

$A * B$ attribute highlights AVO class III anomalies as shown in Fig. 5.6. Far-near attribute volume in not useful for these AVO anomalies, since it slightly shows the difference between these events and the background.

5.5   Simultaneous inversion

Simultaneous inversion seems to correlate with well log data in most of the wells. However, well M-1 shows a poor correlation. The low frequency trend could not be working for this well. P-impedance, VpVs ratio and density volumes can be displayed together with log data as shown in Fig. 5.7.

5.5.1   Final integration

The integration of RPTs, AVO analysis and seismic inversion data allows a better understanding of the cause of the seismic amplitude. Figure 5.8 is a display of these techniques together and how they can the complement each other. Lithofacies from RPTs indicate an oil sand at 1700 ms. $A * B$ AVO attribute highlights this event showing high value, as this is a class II AVO anomaly. Mapping this event allows to define areal distribution and relationship with other facies present in the area. Lithofacies from inverted data and rock physics define well the facies distribution within and around the well locations.
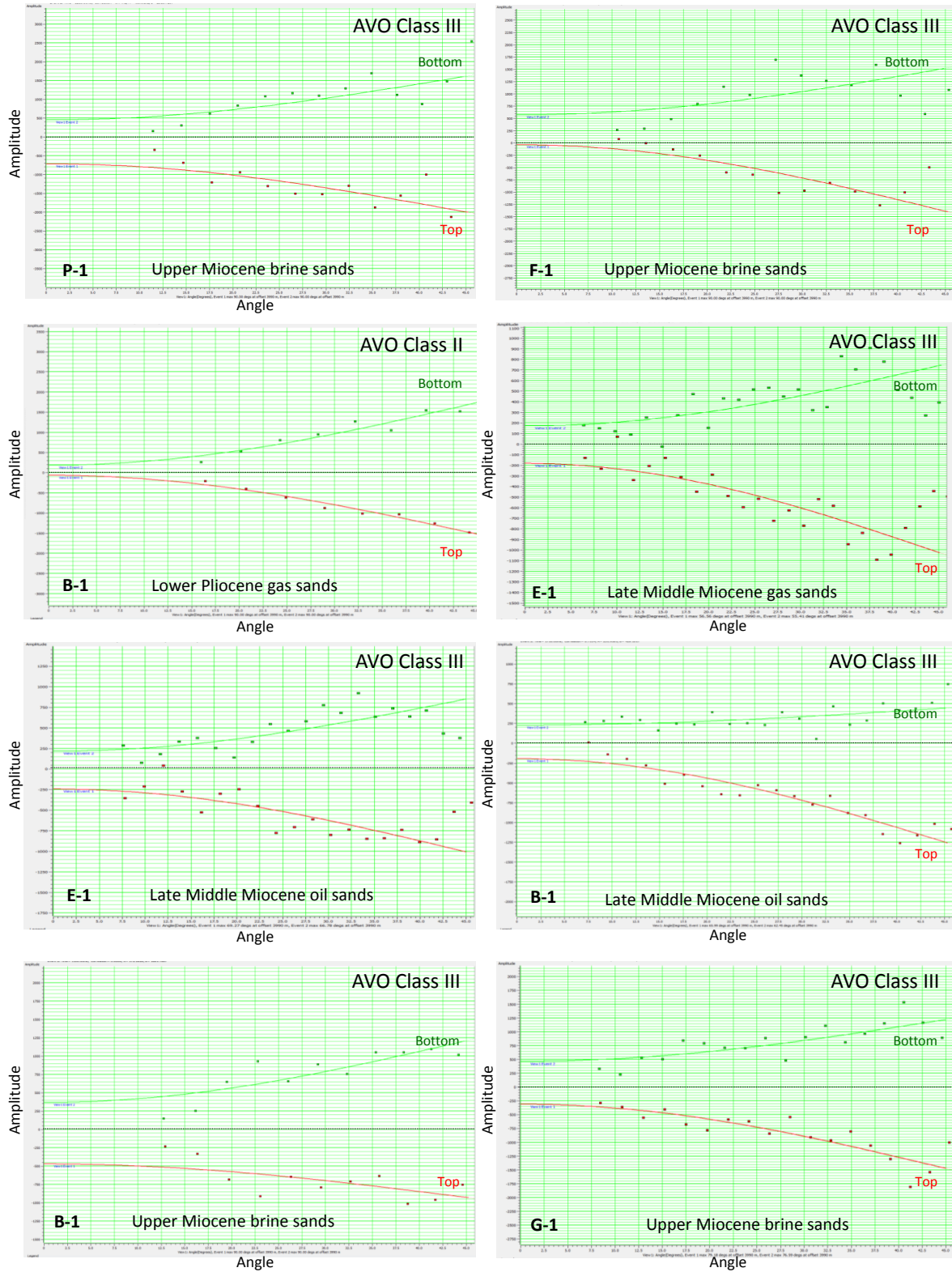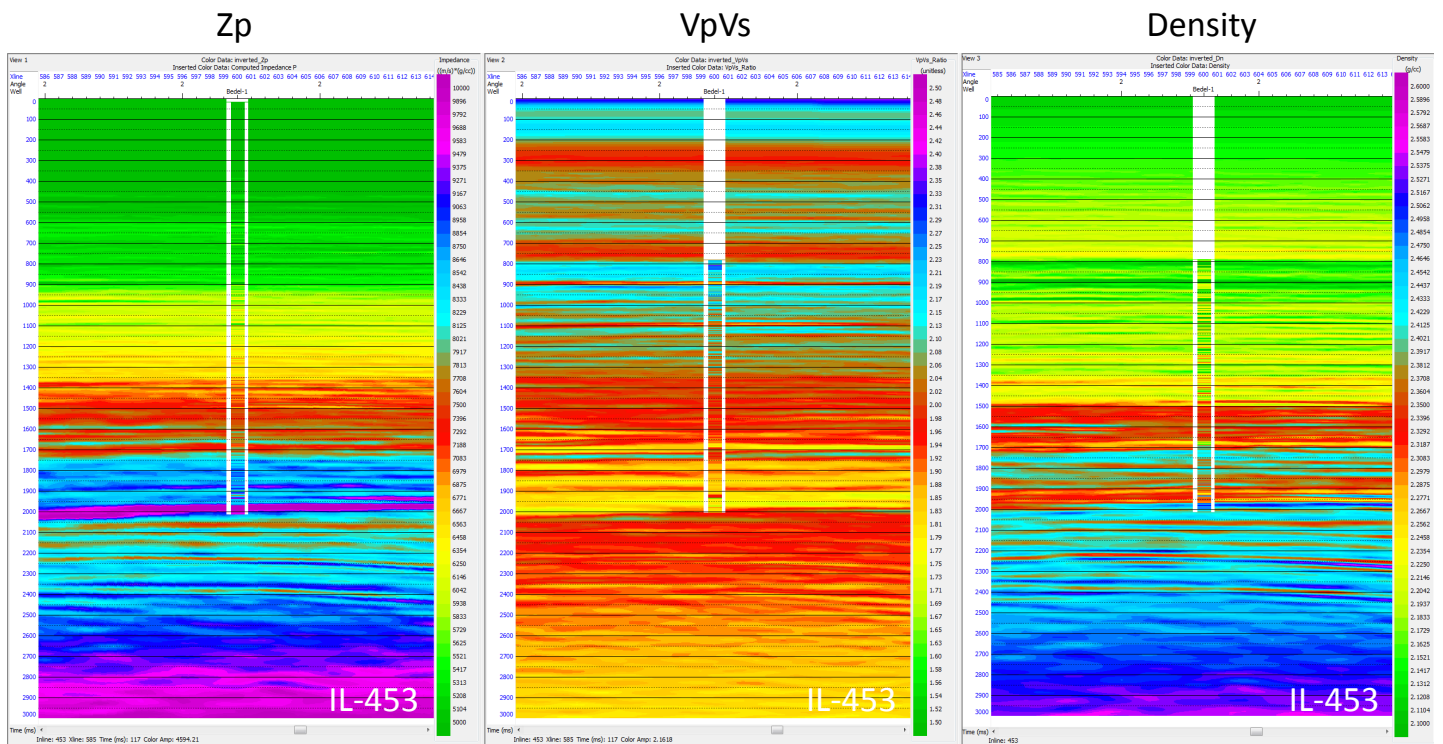
Figure 5.5: AVO gradient analysis for different facies, depths and locations in the Agua Fría area.
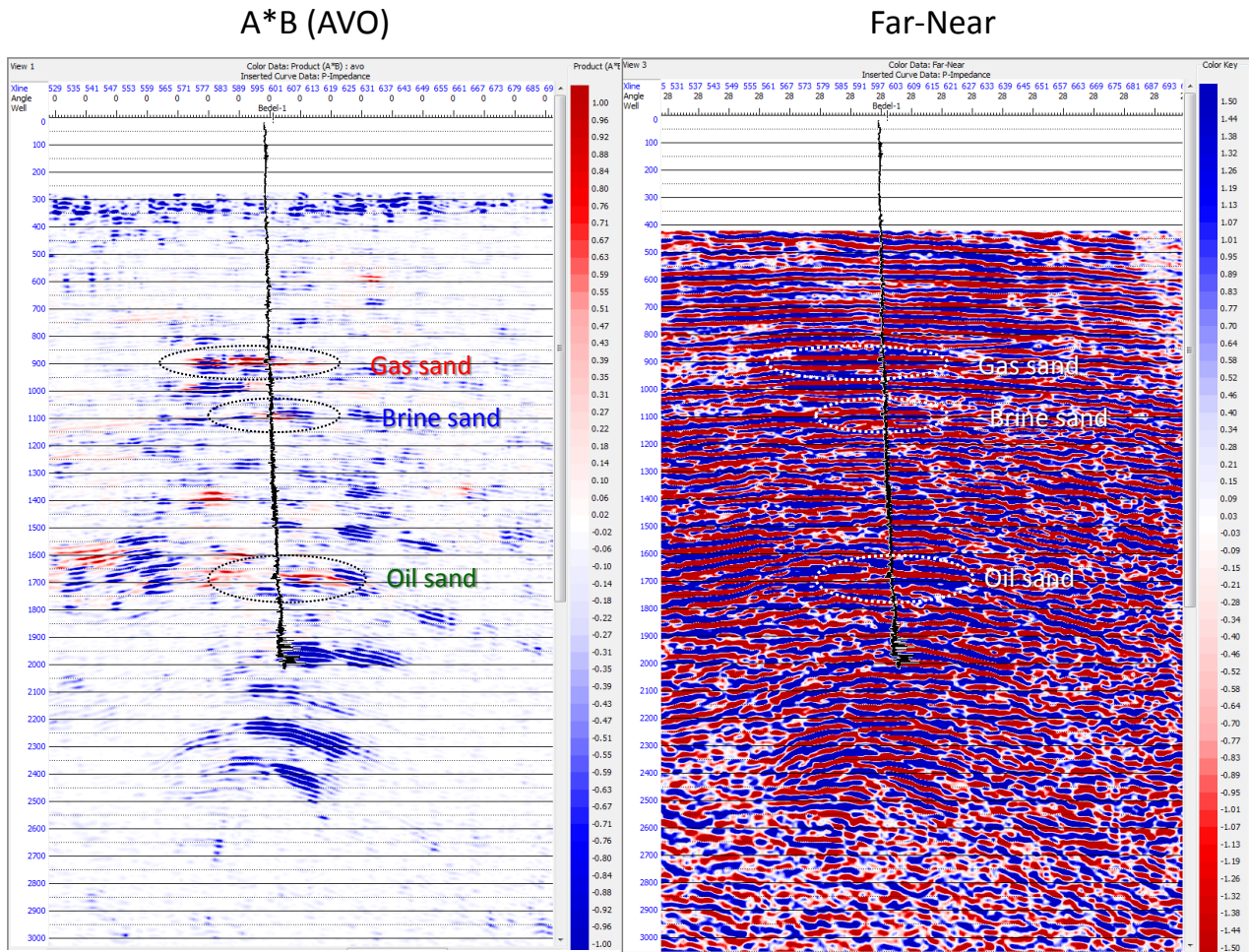
Figure 5.6: AVO attribute $A * B$ is useful tool for AVO class III anomalies. Far-Near attribute slightly highlights this anomalies.

Figure 5.7: Simultaneous inversion for Agua Fría pre-stack data. Data shows good correlation between inverted P-impedance, VpVs ratio and density, and well B-1 log elastic data.
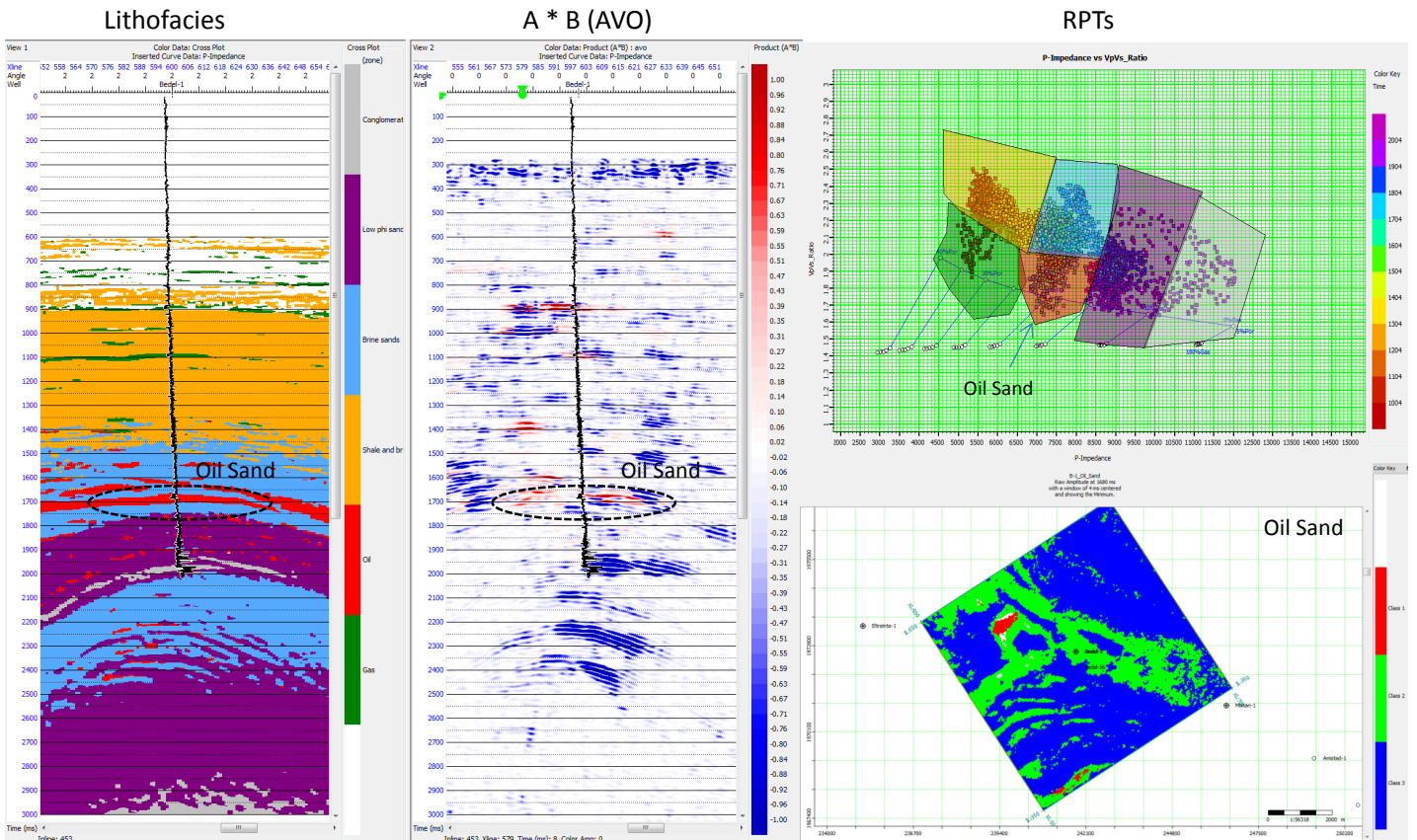
Figure 5.8: Integrated RPTs, AVO attributes and seismic inversion data.

Chapter 6

Discussion

A porosity loss due to mechanical compaction during burial affected the rocks in the study area. A later uplift during Late Miocene and Pliocene changed the rocks position to a shallower depth, keeping the porosity obtained during burial. Porosity-depth trends have a good correlation with the porosity estimated with log data. Both shale and sand porosities decrease with depth due to compaction. Velocity depth trends increase with depth accordingly.

The amplitude anomalies reached by wells P-1, Pl-1, F-1 and C-1 correspond to brine sands. These sands show both, low acoustic impedance and low VpVs ratio compared with the overlying shale. This contrast is confirmed by the simultaneous inversion and the AVO analysis which shows a negative intercept and a negative gradient at the top of the sands. Sands in Pl-1 were tested with the MDT log tool and no hydrocarbon traces were detected with the live fluid analyzer module (LFA). On the other hand, brine sands around 1000-2000 m, drilled by wells G-1, M-1 and E-1 show a small acoustic impedance contrast at the interface with their overlying shales. This can be observed with post-stack seismic data where low amplitude horizons are present in this depth interval.

Gas and oil discoveries correspond mainly to AVO class III anomalies, however in well B-1, one AVO class II event is observed in a gas sand.

One brine sand at 2100 m in well G-1 and one brine sand at 1350 m in well B-1 show an AVO class III response. The cause of this behavior can be the presence of small amounts of gas, causing a decrease of acoustic impedance at the shale-sand interface. However, the LFA analyzer did not identified any hydrocarbon trace.

From inverted data and RPTs, lithofacies can be defined. Fluid saturation is not

estimated in this project, however further studies should focus on hyadrocarbon saturation from RPTs and inverted data.

The methodology proved to be a complete integration of techniques that reduces of seismic interpretation and can be applied for reservoir characterizations projects.

Chapter 7

Conclusions

Mesogenesis starts at very shallow depth and can extend for more than a hundred of meters due to the low geothermal gradient of 16 °C/km observed in the study area. Mechanical compaction and sorting are the main factors affecting the porosity trend in the selected wells according to the rock physics modelling.

Rock physics templates and velocity trends are a useful tool in the study area for porosity, lithology and fluid prediction and, also decrease uncertainty to the amplitude anomalies interpretation.

AVO class III are the main class present in the study area. However, this response can be related to brine, oil or gas sands. Rock physics templates helps to understand this response and to decrease uncertainty to the analysis of these amplitude anomalies.

Some brine sands around 1000-2000 m in the northern part of the area show a low acoustic impedance and VpVs ratio compared with their overlaying shale. This high contrast in acoustic impedance causes an amplitude and AVO anomaly that can misin-terpreted as hydrocarbons accumulations. Further analysis should be made for defining what is causing the low AI values in these sands. On the other hand, brine sands at the same depth interval but in the southern part of the seismic cube, show a small contrast in AI resulting in a low amplitude event in post- and pre-stack data.

Rock physics, AVO analysis and seismic inversion methods are directly related to contrasts in acoustic impedance and VpVs ratio. Therefore, the integration of these techniques allow to quantify seismic interpretation and reduce uncertainty during the analysis of amplitude anomalies.

This methodology can be applied for prospects evaluation, as well for reservoir

characterization projects.

Further work can be done for the deepest part of the study area. As other diagenetic processes can be affecting the rocks, new rock physics models should be tested in these formations.

Bibliography

[1] Ferrari L., López-Martínez M., Aguirre-Díaz G. and Carrasco-Núñez G., 1999, Space-Time patterns of Cenozoic arc volcanism in central Mexico: from the Sierra Madre Occidental to the Mexican Volcanic Belt. Geology, 27, pp. 303-306.

[2] Prost G. and Aranda M., 2001, Tectonics and hydrocarbons systems of the Veracruz Basin, Mexico, in Bartolini C., Buffler RT and Cantú-Chapa A., eds., The western Gulf of Mexico Basin: Tectonics, sedimentary basins, and petroleum systems: AAPG Memoir 75, pp. 271-291.

[3] Jennette D.C., Wawrzyniec T.F. , Fouad K., Meneses-Rocha J., Holtz M., Sakurai S., Talukdar S., Grimaldo F., Muñoz R., Lugo J. E., Barrera D., Williams C. , Escamilla A., Dutton S., Ambrose W. A., Dunlap D., Bellian J., and Guevara E. H., 2002, Integrated basin analysis and gas-play characterization of the Miocene and Pliocene strata in the Veracruz Basin, southeastern Mexico, AAPG Bulletin.

[4] PEMEX-IMP-Amoco, 1995, Estudio tectónico del Cinturón Plegado y Cabalgado de Zongolica y de la Cuenca Terciaria de Veracruz. Internal Report, PEMEX E&P.

[5] Viniegra F., 1965, Geología del Macizo de Teziutlán y de la cuenca cenozoica de Veracruz. AMGP bulletin, v.17, no. 7-12, p. 101-163.

[6] Rueda-Gaxiola J., 2003, The origin of the Gulf of Mexico Basin and its petroleum sub-basins in Mexico, based on red bed and salt palynostratigraphy, in Bartolini C., Buffler RT., and Blickwede J., The Circum-Gulf of Mexico and the Caribbean: Hydrocarbon habitats, basin formation, and plate tectonics: AAPG Memoir 79, p. 246-282.

[7] Tarango-Ontiveros G., 1985, Monografía Geológico Petrolera de la Zona Centro. Internal report, PEMEX E&P.

[8] Salvador A., 1987, Later Triassic-Jurassic paleogeography and origin of Gulf of Mexico Basin. AAPG Bulletin, v.71, p. 419-451.

[9] Santoyo-Pineda, P.J., 1983, Informe final Pozo Heim-1. Internal report, PEMEX E&P.

[10] Baldit-Sandoval, A.J., 1985, Informe geológico final Pozo Dos Matas-1. Internal report, PEMEX E&P.

[11] Escalera-Alcocer J.A., 1985, Informe final Pozo Covarrubias-101A. Internal report, PEMEX E&P.

[12] Martínez-Medrano, M., Vázquez-Benítez, R., Valdivieso-Ramos, V., Rivera-Cruz, S., Hernández-Martínez, R., Flores-Cruz, F., Ángeles-Marín, D., López-Martínez, C., Padilla-Ramos, S., Cuevas-González, C., 2010, Interated seismic and petrographic analysis of the sandstone reservoirs of the Tertiary Veracruz Basin, Mexico. In Gaxiola, J.R., Móntes de Oca, R.S., Ramos, J.R.R., Bartolini, C. and Cantú-Chapa, A. : The petroleum geology of Mexico. AAPG Memoir 90, p. 1-19.

[13] Jennette D.C., Wawrzyniec T.F. , Fouad K., Meneses-Rocha J., Grimaldo F., Muñoz R., Barrera D., Williams C., and Escamilla A., 2003, Traps and turbidite reservoir characteristics from a complex and evolving tectonic setting, Veracruz Basin, southeastern Mexico. AAPG Bulletin, v.87, p. 1599-1622.

[14] Cruz-Helú, P., Verdugo, R., Bárcenas, R., 1977, Origin and distribution of Tertiary conglomerates, Veracruz Basin, Mexico. AAPG Bulletin, v.61, p. 207-226.

[15] Arreguín-López, M.A. and Weimer, P., 2004, Regional sequence stratigraphic setting of Miocene-Pliocene sediments, Veracruz Basin, Mexico. GCAGS Transactions, v.54, p. 25-40.

[16] Arreguín-López, M.A., 2005, Estratigrafía de secuencias de sistemas turbidíticos de aguas profundas de sedimentos del Plioceno y Mioceno, Cuenca de Veracruz. AMGP Bulletin, v.52, no. 1, p. 51-63.

[17] González-García, R. and Holguín-Quiñones, N., 1992, Las rocas generadoras de Mexico. AMGP Bullletin, v.42, no.1, p. 16-30.

[18] Serrano-Bello, E., Román-Ramos, J.R., Holguín-Quiñones N., Vázquez-Covarrubias, E., Galindo-Hernandez, A. and Grass, D., 1996, Subsistemas generadores de la Cuenca de Veracruz, Mexico. Memorias V Congreso Latinoamericano de Geoquímica Orgánica, Cancún Mexico, p. 127-129.

[19] Talukdar, S.C., Guevara, E.H., Galindo-Hernández, A., Wawrzyniec, T.F., Villanueva-Rodríguez, L., Fouad, K., Vázquez-Covarrubias, E., Sánchez-Barreda, L., Meneses-Rocha, J., Jeanette, D.C., Lugo-Rivera, J.E., 2003, Importance of Deep Burial of Mesozoic Oil-Prone Source Rocks for Commercial Gas Accumulations in Tertiary Reservoirs, Veracruz Basin, Southern Mexico, Abstracts AAPG International Conference, Barcelona.

[20] Meneses de Gyves, J., 1953, Condiciones estratigráficas de los sedimentos terciarios en la Cuenca de Veracruz. AMGP Bulletin, v. 5, no. 3-4, p. 105-112.

[21] Martínez, M., Serrano, E., Bartolo, C., Toriz, J., Espinoza, M. and Vázquez, R., 2001, Mesozoic Plays of the Córdoba Platform, Veracruz Basin. Abstracts AAPG Annual Meeting Denver Colorado.

[22] Schlumberger, 2010, Descubra el Yacimiento, WEC México.

[23] Curtis, C.D., 1977, Sedimentary geochemistry: environments and processes dominated by involvement of an aqueous phase. Philosophical Transactions of the Royal Society, London, p. 353-372.

[24] Burley, S.D., Kantorowicz, J.D. and Waugh, B., 1985, Sedimentology: Recent and Applied Aspects (Eds P. Brenchley & B.P.B. Williams). Special Publication Geological Society of London, Blackwell Scientific Publications, Oxford, v. 18, p. 189-226.

[25] Frey, M., 1987, Very low grade metamorphism of clastic sedimentary rocks. In: Low Temperature Metamorphism (Ed. M. Frey). Blackie, London, p. 9-58.

[26] Slater, D.J., Yardley, B.W.D., Spiro, B. and Knipe, R.J., 1994, Incipient metamorphism and deformation in the Variscides of SW Dyfed, Wales: first steps towards isotopic equilibrium. Journal of Metamorphic Geology, v. 12, p. 237-248.

[27] Berner, R.A., 1980, Early Diagenesis: A Theoretical Approach. Princeton Series in Geochemistry, Princeton University Press, Princeton, NJ.

[28] Chapelle, F.H., 1993, Ground-water Microbiology and Geochemistry. John Wiley and Sons, New York, p. 448.

[29] Morad, S., Ketzer, J.M. and De Ros, L.F., 2000, Spatial and temporal distribution of diagenetic alterations in siliciclastic rocks: implications for mass transfer in sedimentary basins. Sedimentology, v. 47, p. 95-120.

[30] Worden, R.H. and Burley, S.D., 2009, Sandstone Diagenesis: The Evolution of Sand to Stone, in Sandstone Diagenesis: Recent and Ancient (eds S.D. Burley and R.H. Worden), Blackwell Publishing Ltd., Oxford, UK. p. 8.

[31] Vesic, A.S. and Clough, G.W., 1968, Behavior of granular materials under high stresses. Journal of Soil Mechanics and Foundations Division, v. 94, p. 661-688.

[32] Surdam, R.C., Crossey, L.J., Hagen, E.S. and Heasler, H.P., 1989, Organic-Inorganic Interactions and Sandstone Diagenesis. AAPG Bulletin, v. 73.

[33] Kurkjy, K.A., 1988, Experimental compaction studies of lithic sands: Master's thesis, University of Miami, Miami, Florida.

[34] Primmer, T.J., Cade, C.A., Evans, I.J., et al., 1997, Global patterns in sandstones diagenesis: Application to reservoir quality prediction for petroleum exploration. AAPG Memoir, v. 69, p. 61-78.

[35] Waugh, B., 1971, Formation of quartz overgrowths in the Penrith Sandstone (Lower Permian) of northwest England as revealed by scanning electron microscopy. Sedimentology, v. 17, p. 309-320.

[36] Hein, J.W. de Baar, German, C.R., Elderfield, H., Vaan Gaans, P., 1979, Rare earth element distributions in anoxic waters of the Cariaco Trench. Geochemica et Cosmochimica Acta, v. 52, p. 1203-1219.

[37] Ostrander, W.J., 1984, Plane wave reflection coefficients for gas sands at nonnormal angles of incidence. Geophysics, v. 49, p. 1637-1648.

[38] Zoeppritz, K., 1919, Erdbebenwellen VIIIB, Ueber Reflexion and Durchgang seismischer Wellen durch Unstetigkeitsflaechen. Goettinger Nachrichten, I, p. 66-84.

[39] Aki, K, and Richards, P.G., 1980, Quantitative Seismology: Theory and Methods. San Francisco: W.H. Freeman and Co.

[40] Shuey, R.T., 1985, A simplification of the Zoeppritz equations. Geophysics, v. 50, p. 609-614.

[41] Koefoed, o., 1955, On the effect of Poisson's ratios of rock strata on the reflection coefficients of plane waves. Geophysics Prospecting, v. 3, p. 381-387.

[42] Avseth P., Mukerji T., and Mavko G., 2005, Quantitative seismic interpretation: Applying rock physics tools to reduce interpretation risk. Cambridge University Press.

[43] Rutherford, S.R., and Williams, R.H., 1989, Amplitude-versus-offset variations in gas sands. Geophysics, v. 54, p. 680-688.

[44] Ross, C.P., and Kinman, D.L., 1995, Non-bright spot AVO: Two examples. Geophysics, v. 60, p. 1398-1408.

[45] Castagna, J.G. and Swan, H.W., 1997, Principls of AVO crossplotting. The Leading Edge, v. 16, p. 337-342.

[46] Dahl, T. and Ursin, B., 1992, Non-linear AVO inversion for a stack of anelastic layers, Geophysics Prospecting , v. 40, p. 243-265.

[47] Buland, A., Landroe, M., Anderssen, M., and Dahl, T., 1996, AVO inversion of Troll Field data. Geophysics, v. 61, p. 1589-1602.

[48] Gouveia, W., and Scales, J.A., 1998, Bayesian seismic waveform inversion: Parameter estimation and uncertainty analysis, J. Geophysics, Res. v. 103, p. 2759-2779.

[49] Smith, G.C., and Gidlow, P.M., 1987, Weighted stacking for rock property estimation and detection of gas. Geophysics, Prospecting, v. 35, p. 993-1014.

[50] Loertzer, G.J.M., and Berkhout, A.J., 1993, Linearized AVO inversion of multicomponent seismic data. In Offset-Dependent Reflectivity: Theory and Practice of AVO Analysis (ed. Castagna, J. and Backus, M.) Tulsa: Soc. Expl. Geophys., p. 317-332.

[51] Avseth, P., Mavko, G., Dvorkin, J., & Mukerji, T., 2001, Rock Physics and Seismic Properties of Sands and Shales as a Function of Burial Depth. SEG Exposition and Annual Meeting, San Antonio Texas.

[52] Voigt, W., 1910, Lehrbuch der Kristallphysik. Leipzig : Teubner.

[53] Reuss, A., 1929, Berechnung der Fliessgrenzen von Mischkristallen. Z, Angew. Math. Mech, v. 9, p. 49-58.

[54] Dvorkin, J., and Nur, A., 1996, Elasticity of high-porosity sandstones: Theory for two North Sea datasets. Geophysics, v. 61, p. 1363-1370.

[55] Mindlin, R., 1949, Compliance of elastic bodies in contact. Journal of Applied Mechanics, 16, pp. 259-268.

[56] Murphy, W.F.III, 1982, Effects of microstructure and pore fluids on the acoustic properties of granular sedimentary materials. Unpublished Ph.D. thesis, Stanford University.

[57] Gassmann, F., 1951, Über die elastizität poröser medien: Vierteljahrss-chrift der Naturforschenden Gesellschaft in Zurich, 96, 1-23. The English translation of this paper is available at http://sepwww.stanford.edu/sep/berryman/ PS/gassmann.pdf.

[58] Hashin, Z. and Shtrikman, S., 1963, A variational approach to the elastic behavior of multiphase minerals. Journal of the Mechanics and Physics of Solids, 11, pp. 127-140.

[59] Magara, K., 1980, Comparison of porosity-depth relationships of shale and sandstone. Journal of Petroleum Geology, 3, 175-1785.

[60] Ramm, M., and Bjørlykke K., 1994, Porosity/depth trends in reservoir sandstones: assessing the quantitative effects of varying pore-pressure, temperature history and mineralogy, Norwegian Shelf data; Clay minerals, 29, 475-490.

[61] Baldwin, B., and Butler, C.O., 1985, Compaction curves. AAPG Bulletin, v. 69, p. 622-626.

[62] Rubey, W.W., and Hubbert, M.K., 1959, Mechanics of fluid-filled porous solids and its application to overthrust faulting. Part 1 of Role of fluid pressure in mechanics of overthrust faulting. Geo. Soc. Am. Bulletin, v. 70, p- 115-166.

[63] Ødegaard, E, and Avseth, P., 2003, Interpretation of elastic inversion results using rock physics templates, EAGE Ann. Mtg Extended Abstract.

[64] Surdam, R.S., Dunn, T.L., MacGowan, D.B., and Heasler, H.P., 1989, Conceptual models for the prediction of porosity. Evolution with an example from the Frontier Sandstone, Bighorn Basin, Wyoming. In Petrogenesis and Petrophysics of Selected Sandstone Reservoirs of the Rocky Mountain Region (ed.-in-chief Coalson, E.B.) Denver: Rocky Mountain Association of Geologists.

[65] Sintubin, M., 1994, Clay fabrics in relation to the burial history of shales. Sedimentology, v. 41, p. 1161-1169.

[66] Barclay, F., Bruun. A., Camara, A., Cooke, D., Godfray, R., Lowden, D., McHugo, S., Ozdemir, H., Pickering, S., González, F., Herwanger, J., Volterrani, S., Murineddu, A., Rasmussen, A. and Roberts, R., 2008, Inversión Sísmica: Lectura entre Líneas. Oilfield Review, p. 44-48.

[67] Savic, M., VerWest, B., Masters, R., Sena, A. and Gringrich, D., 2000, Elastic Impedance Inversion in Practice. SEG 2000 Expanded Abstracts.

[68] Hampson, D.P., Russell, B.H., and Bankhead, B., 2005, Simultaneous inversion of pre-stack seismic data: Ann. Mtg. Abstracts. SEG, p. 1633-1637.

[69] Mukerji, T., Jørstad, A., Mavko, G., and Granli, J., 1998, Near and far offset impedances: Seismic attributes for identifying lithofacies and pore fluids. Geophysics. Res. Lett., v. 25, p. 4557-4560.

[70] AlMustafa, H. and BakhorjiRock, A.,2011, Rock Physics AVO Depth Trends: Implications for Exploration in Saudi Arabia. SEG Annual Meeting, San Antonio, 5, pp. 386-390.

[71] Box, R. and Doss E., 2008, Typical AVO response as a function of depth and fluid pressure gradient: Gulf of Mexico shelf. The Leading Edge, 8, pp. 1252-1262.

[72] Nasser, M., 2010, Rock Physics-Modeling impact of pore fluid, lithology and depth on AVO signatures. SEG Annual Meeting, Denver, 5, pp. 373-377.

Appendix A

Acoustic impedance vs VpVs ratio cross plots
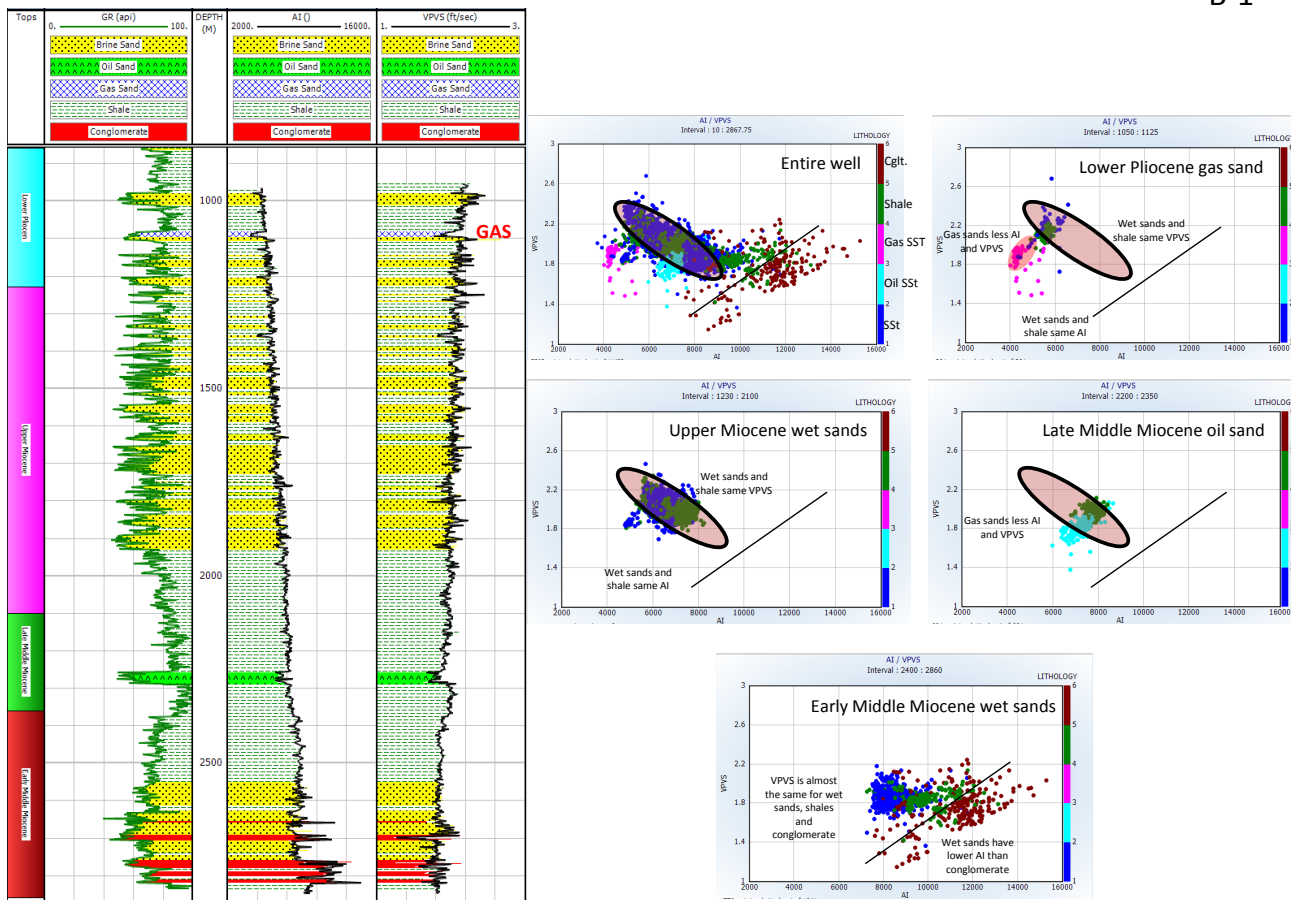
Figure A.1: Well B-1 AI vs VpVs cross plot.
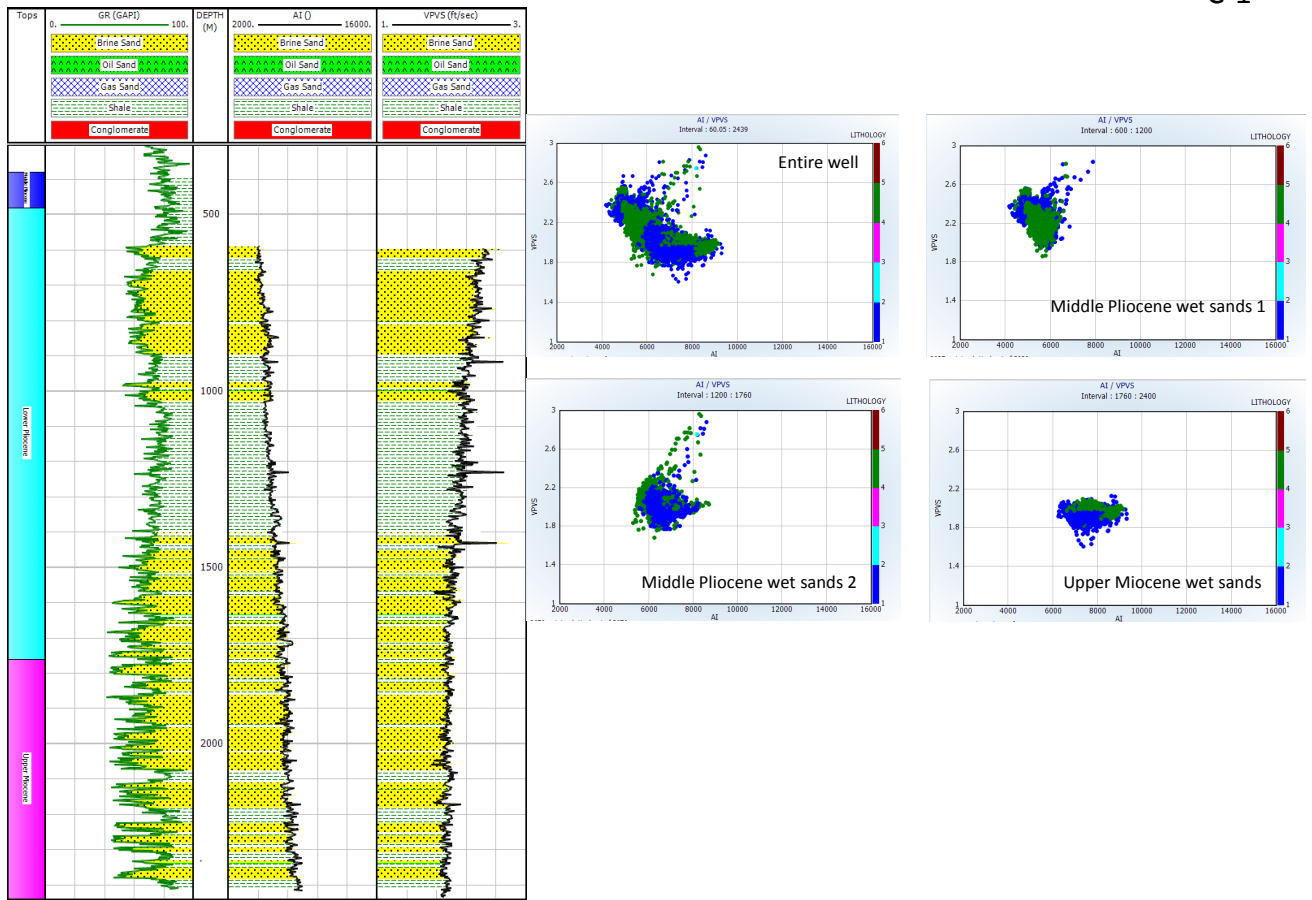
Figure A.2: Well C-1 AI vs VpVs cross plot.
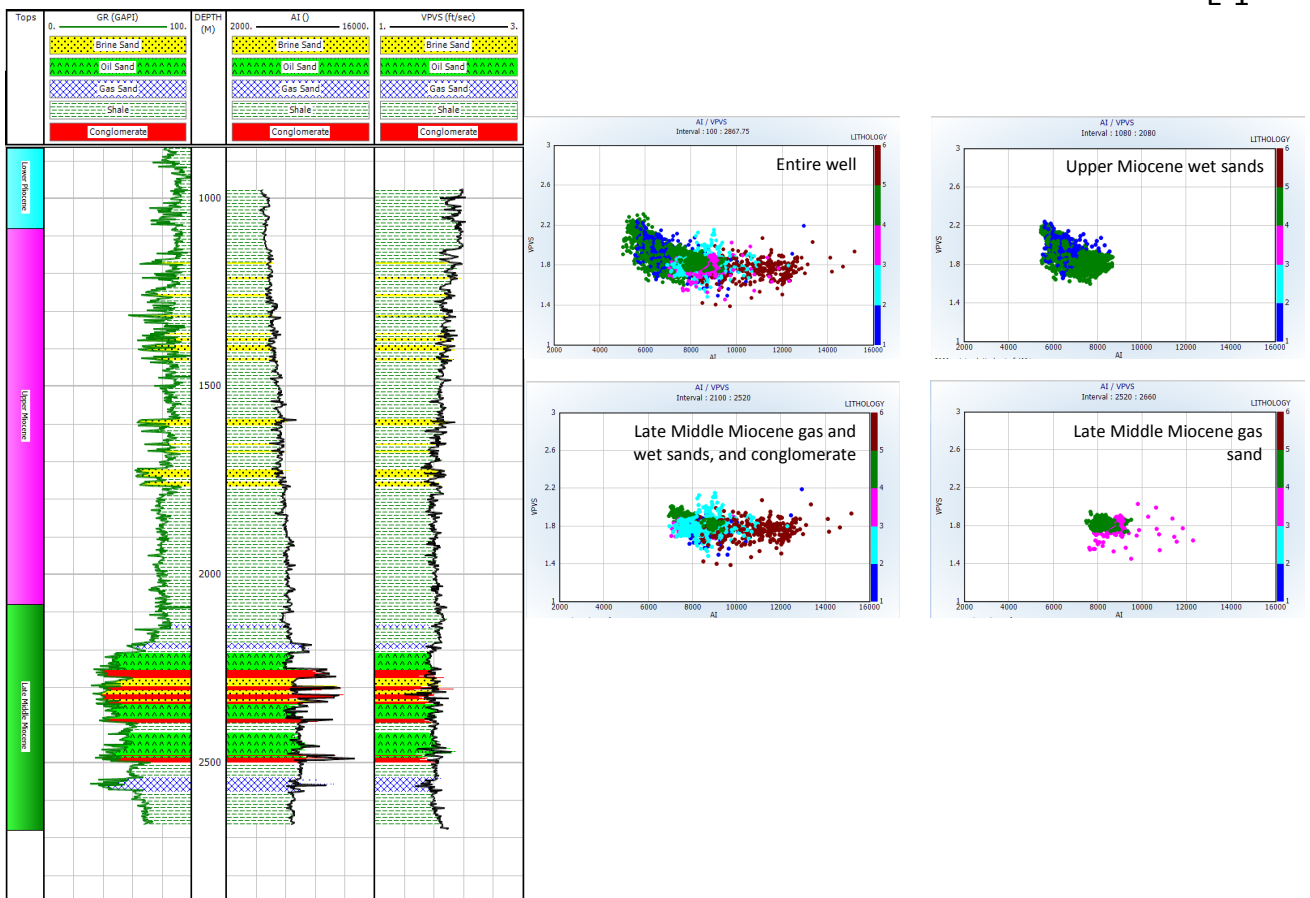
Figure A.3: Well E-1 AI vs VpVs cross plot.
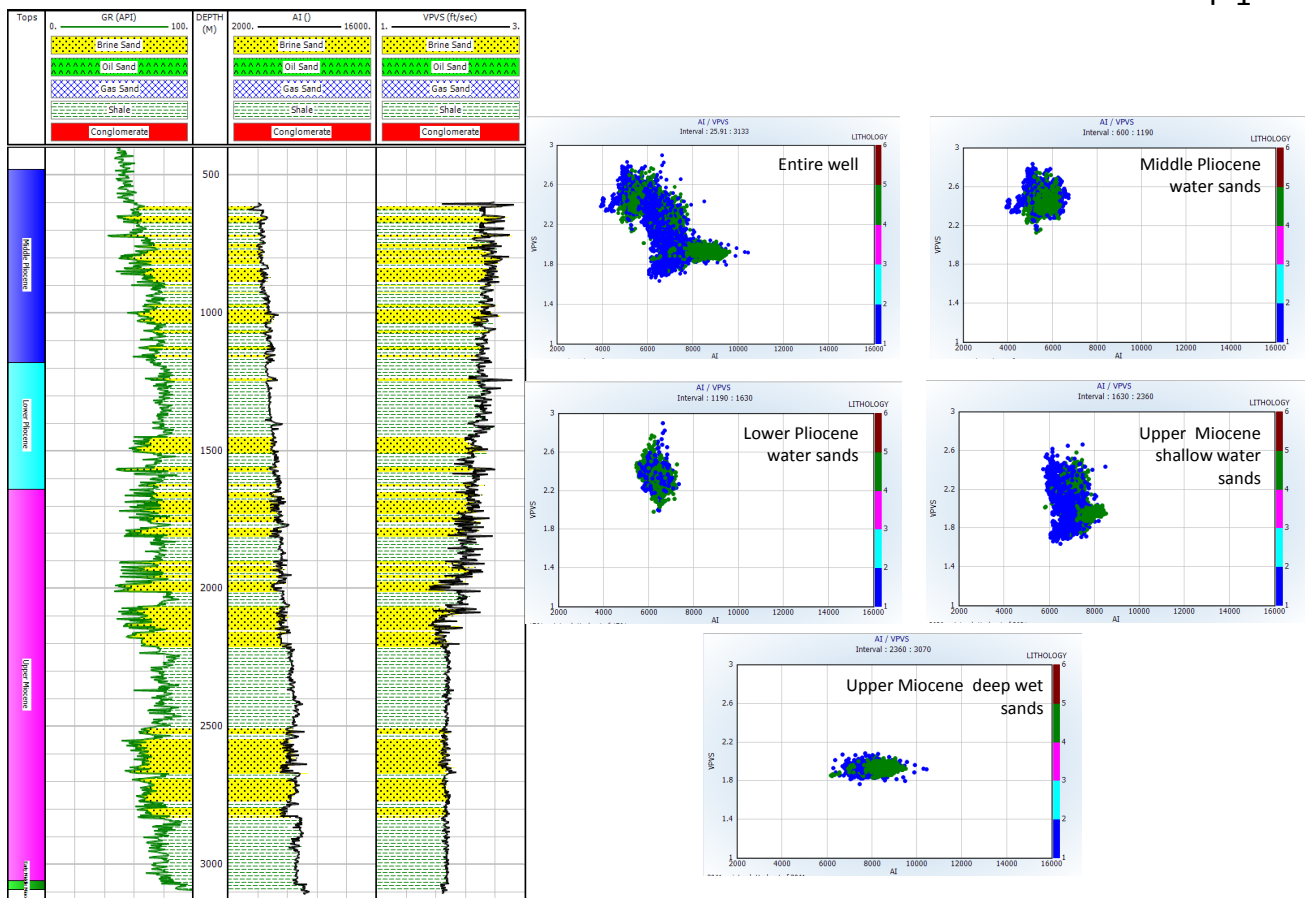
Figure A.4: Well F-1 AI vs VpVs cross plot.
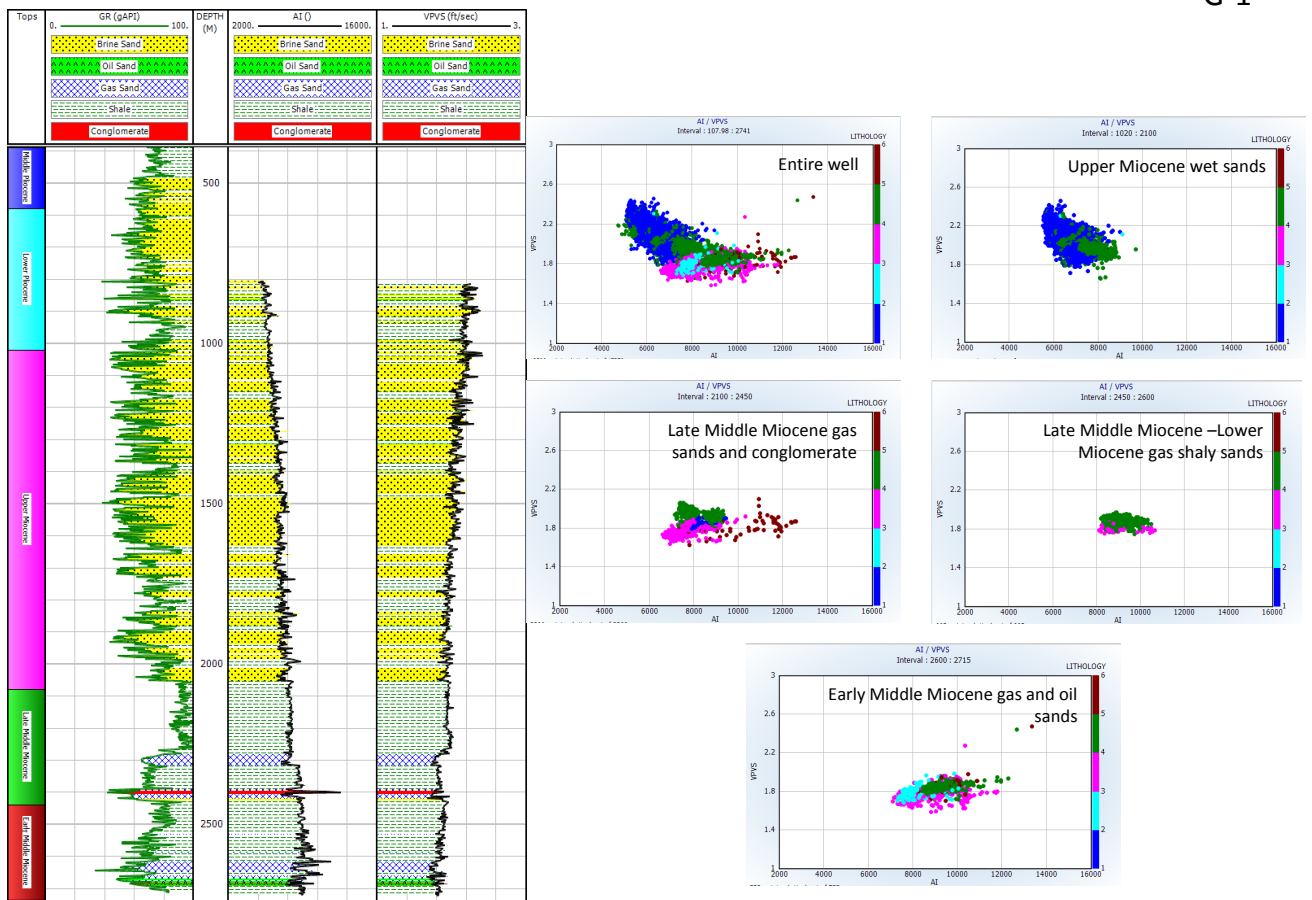
Figure A.5: Well G-1 AI vs VpVs cross plot.
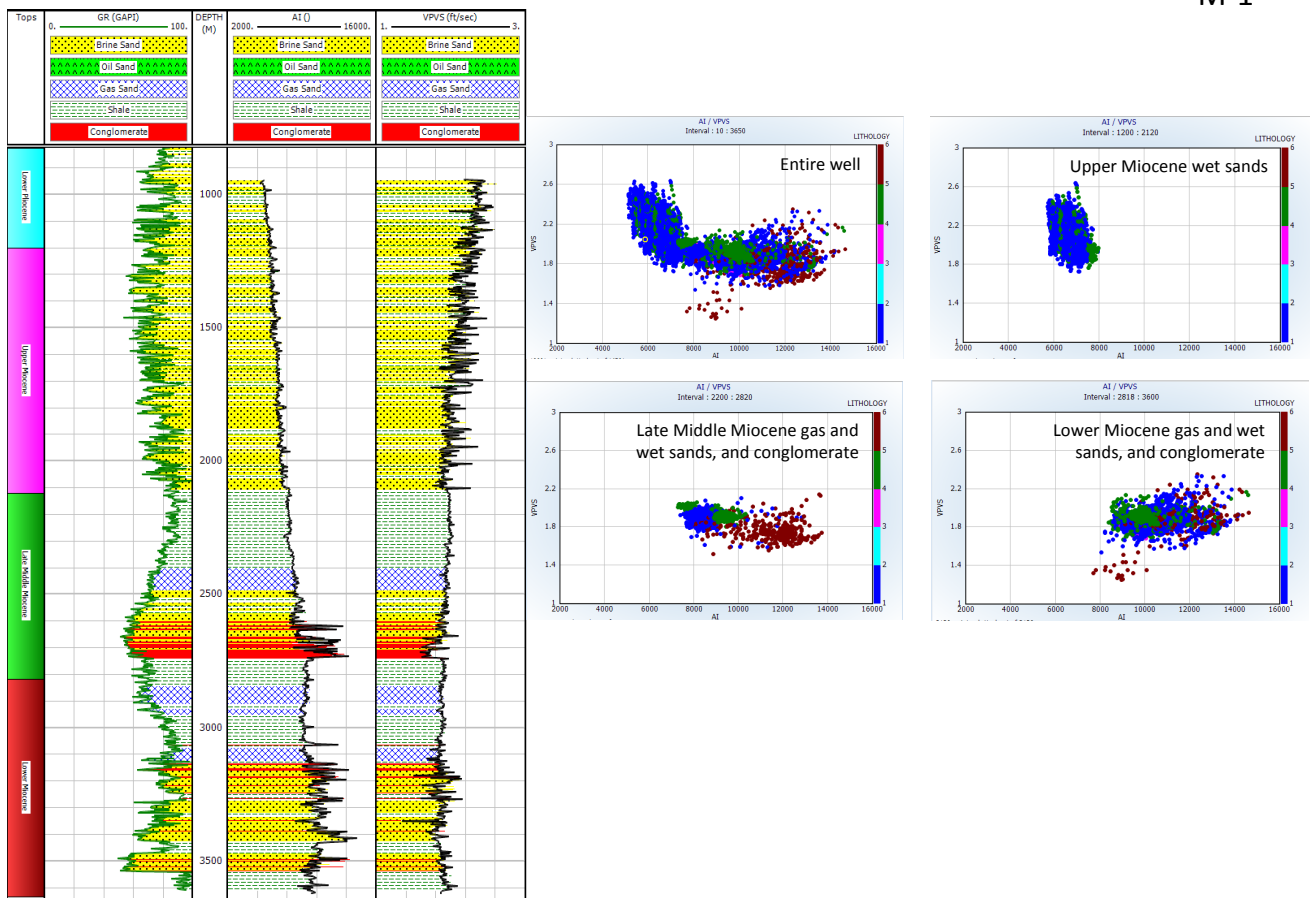
Figure A.6: Well M-1 AI vs VpVs cross plot.
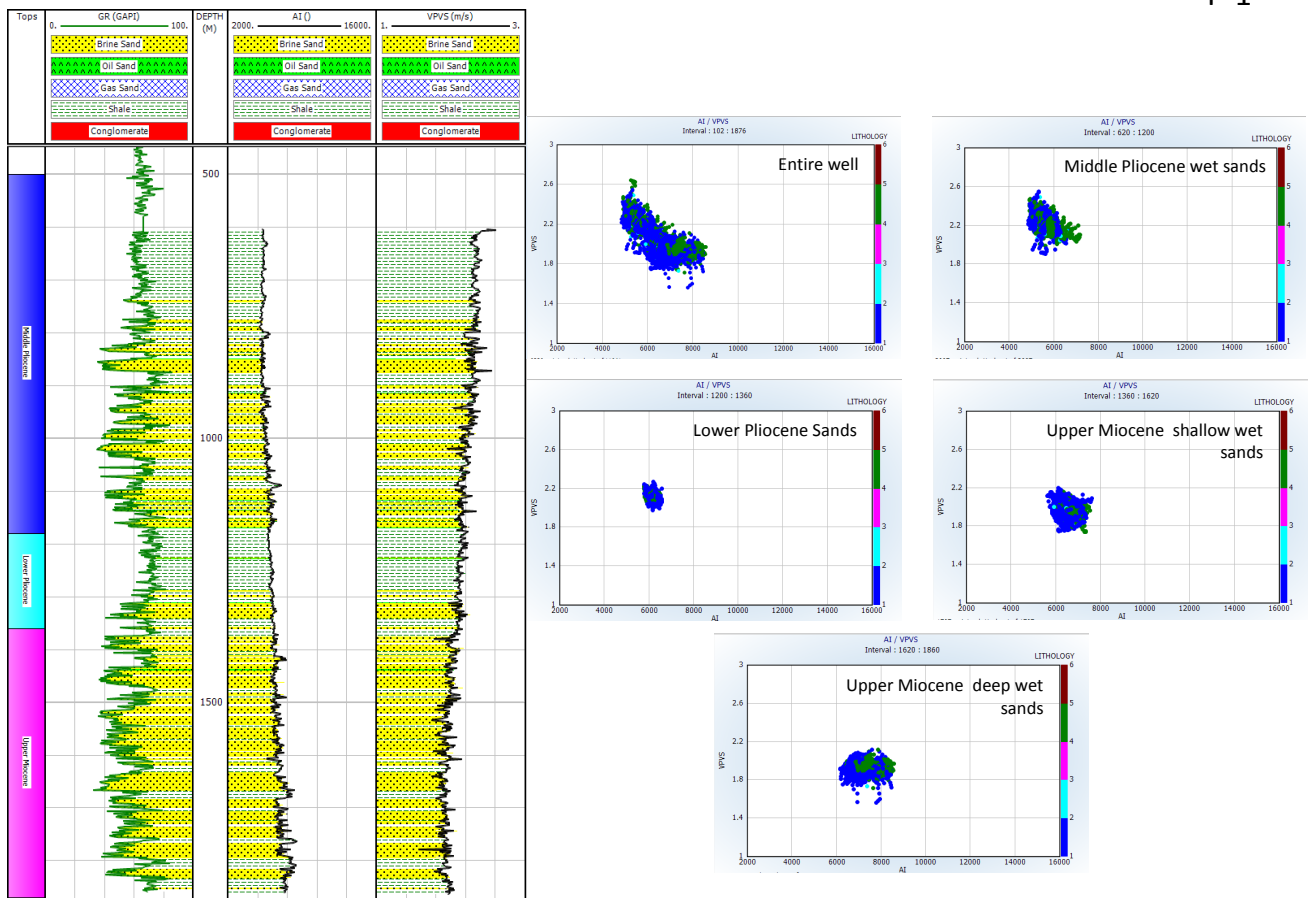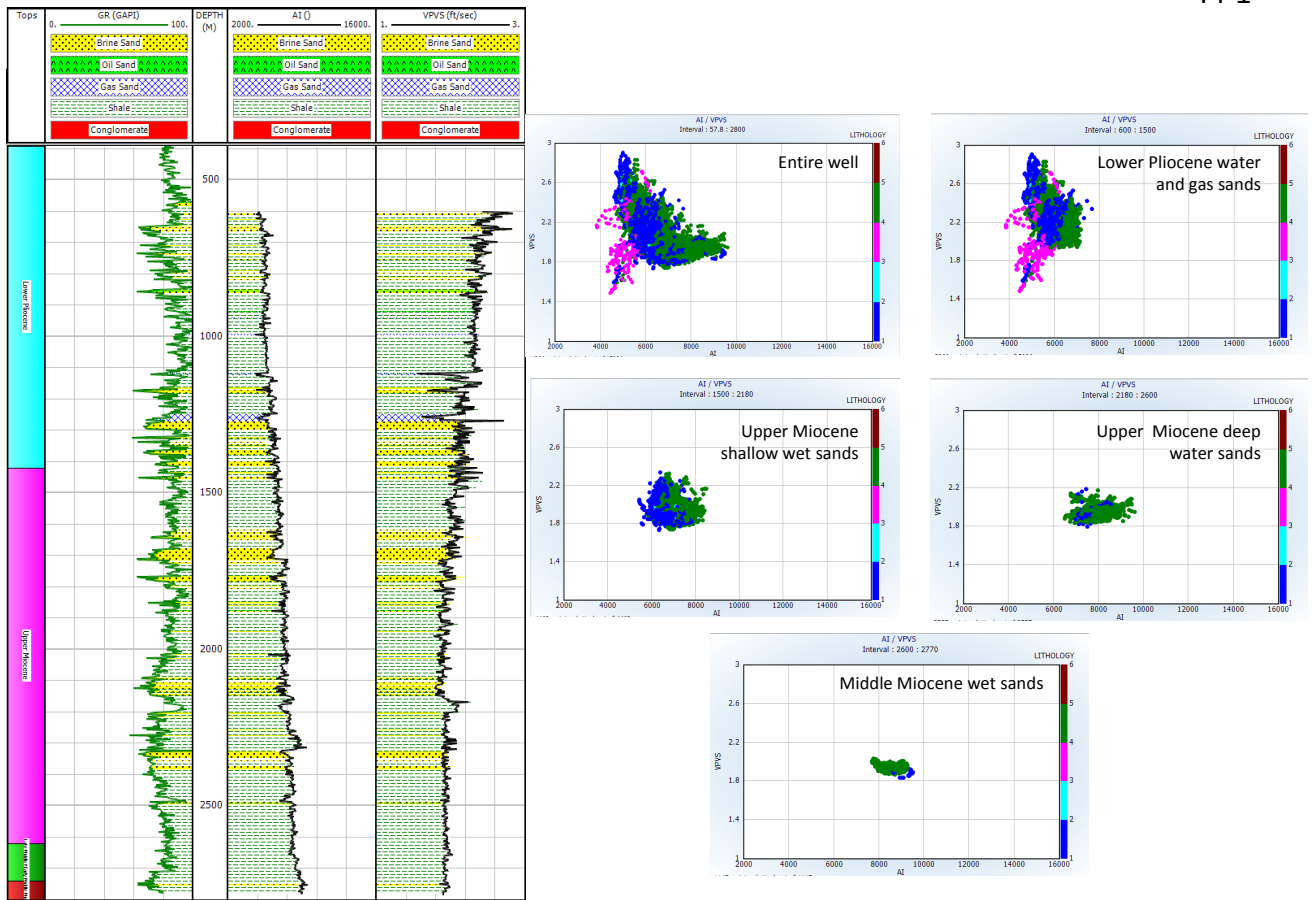
Figure A.7: Well P-1 AI vs VpVs cross plot.

Figure A.8: Well Pl-1 AI vs VpVs cross plot.

Appendix B

Well correlation
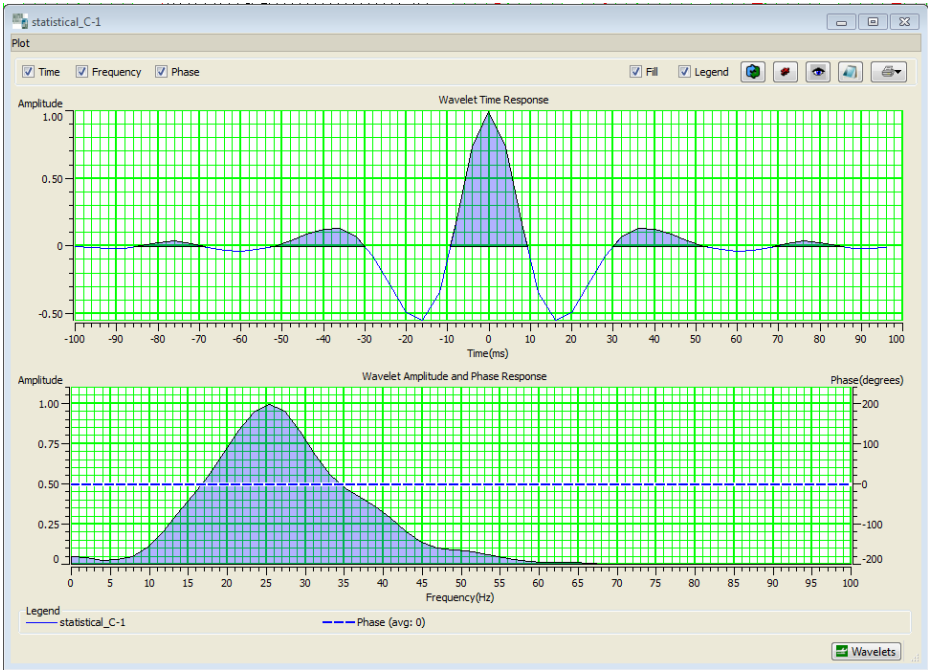
Figure B.1: Statistical wavelet extracted from seismic data.

B-1
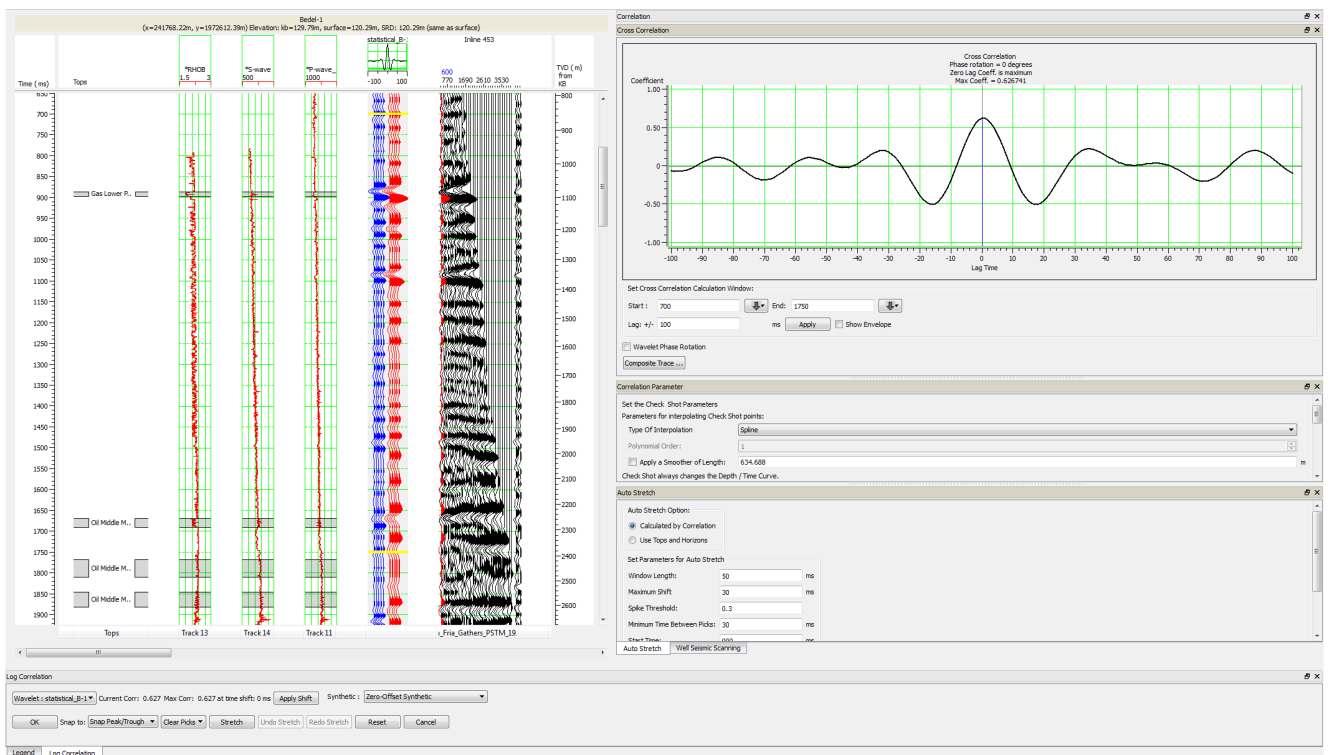
Well correlation

Figure B.2: Well B-1 correlation.
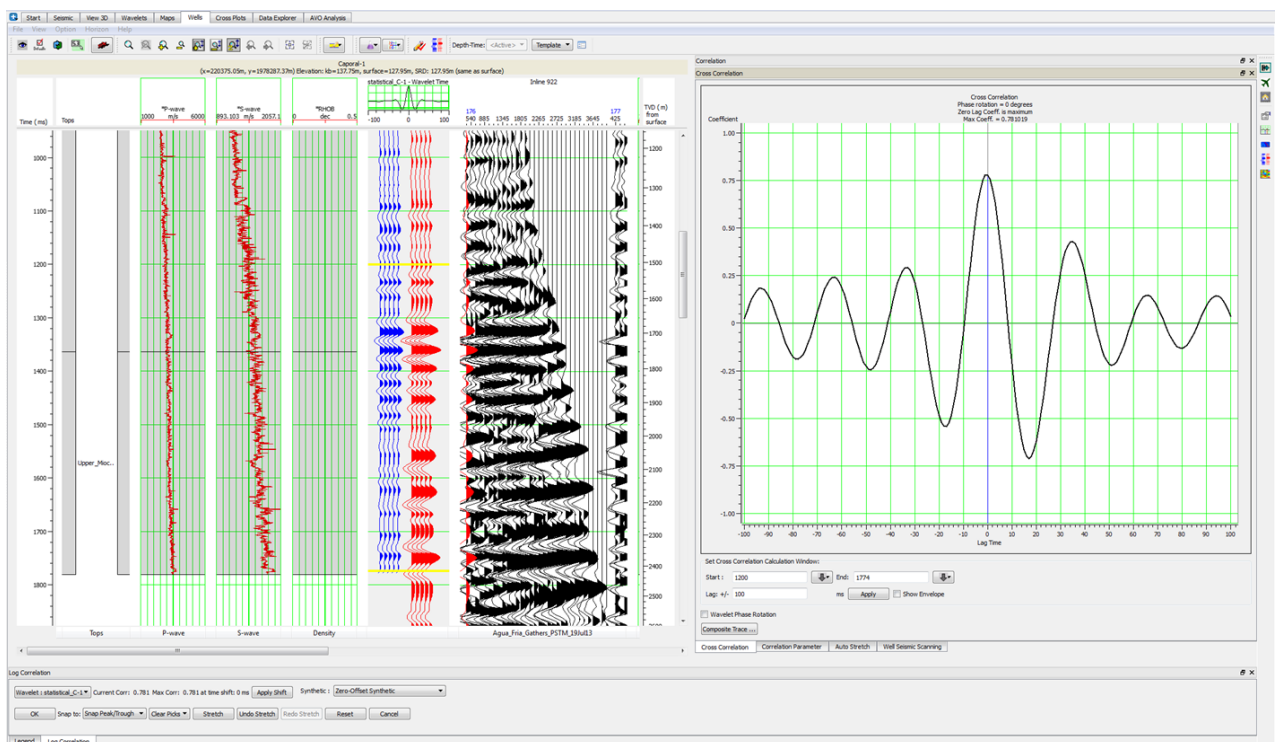
Figure B.3: Well C-1 correlation.
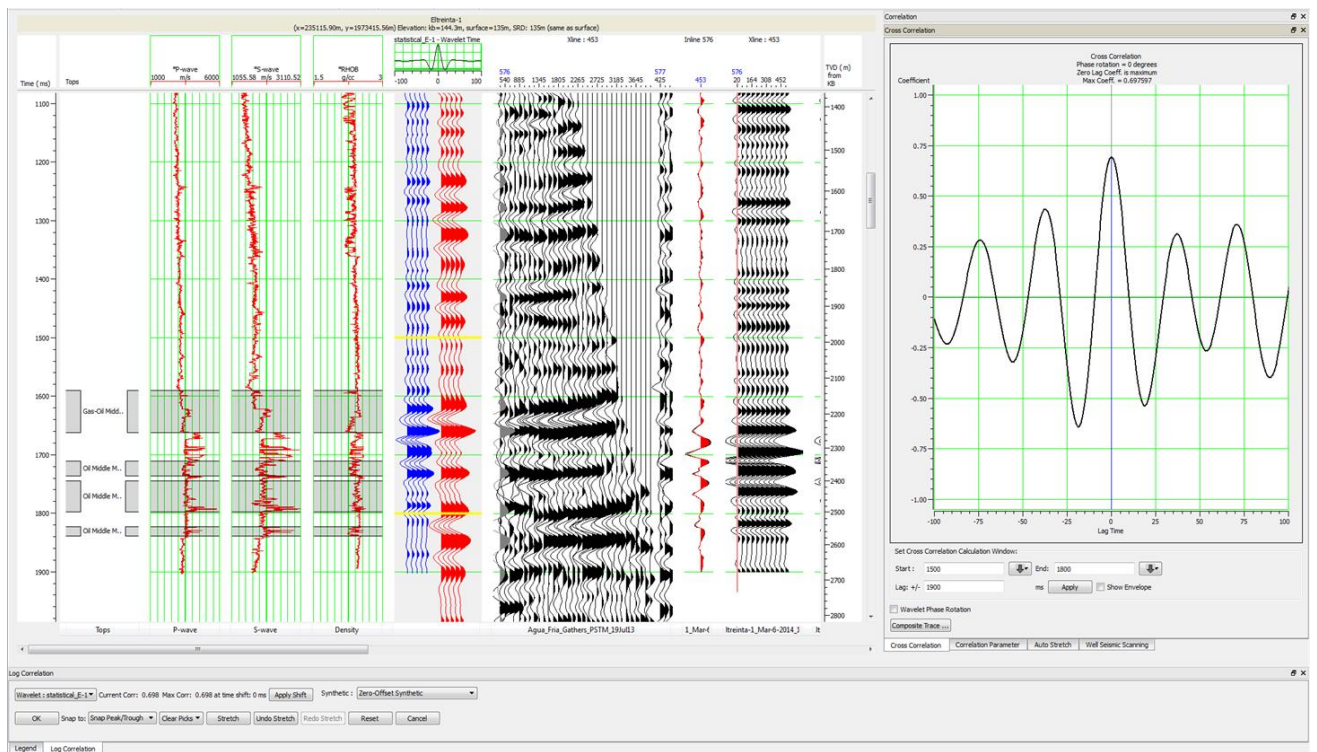
Figure B.4: Well E-1 correlation.
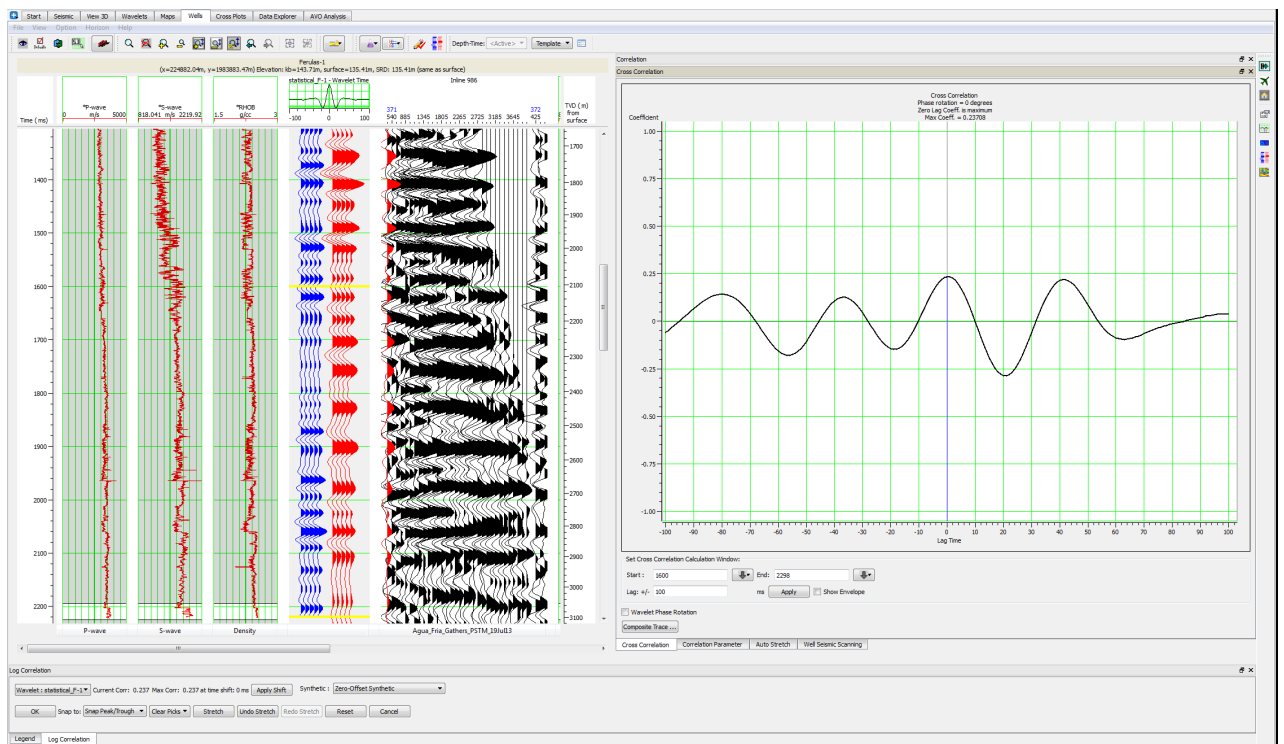
Figure B.5: Well F-1 correlation.
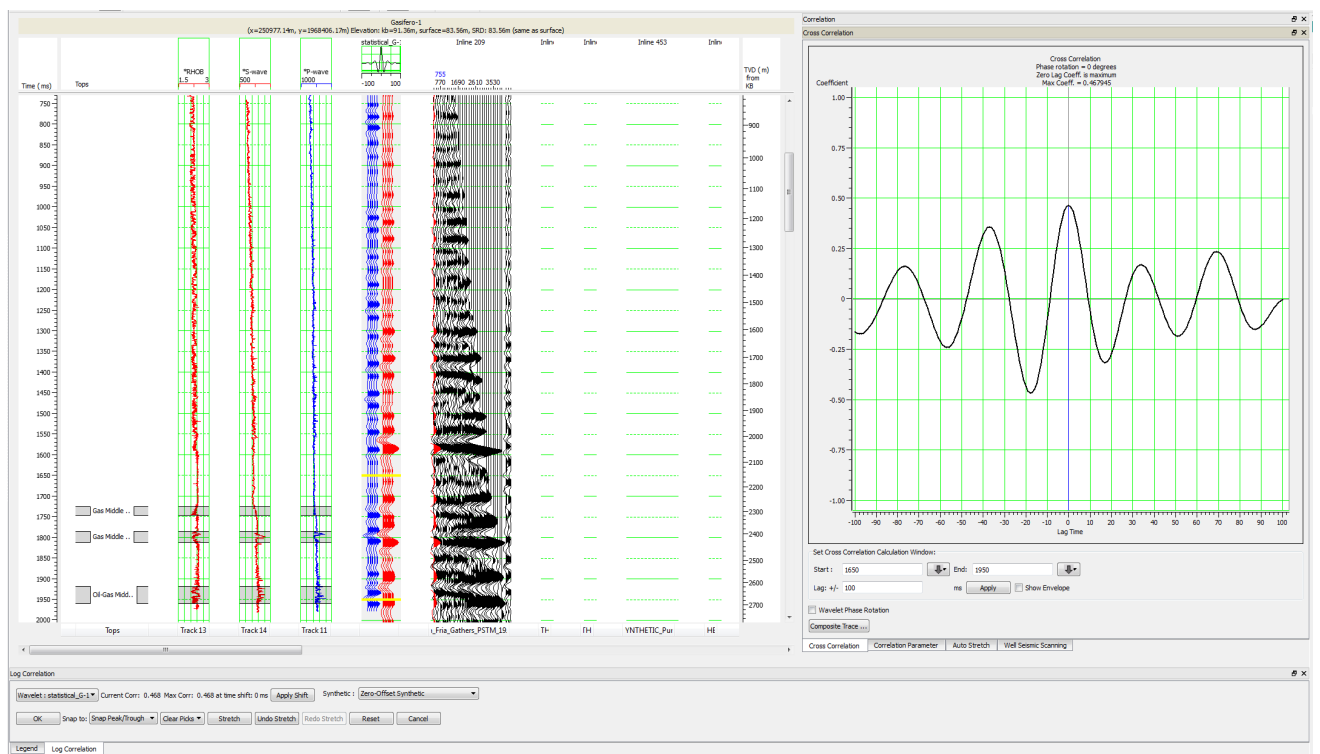
Figure B.6: Well G-1 correlation.
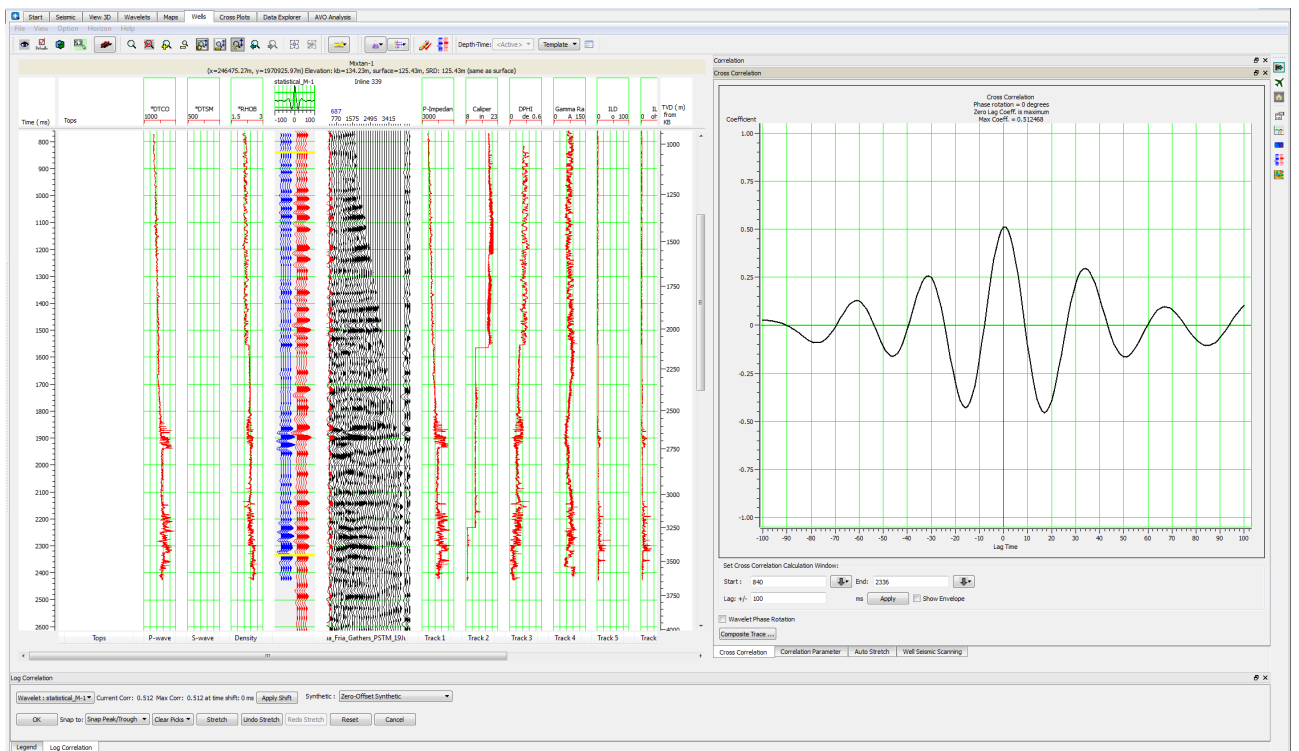
Figure B.7: Well M-1 correlation.
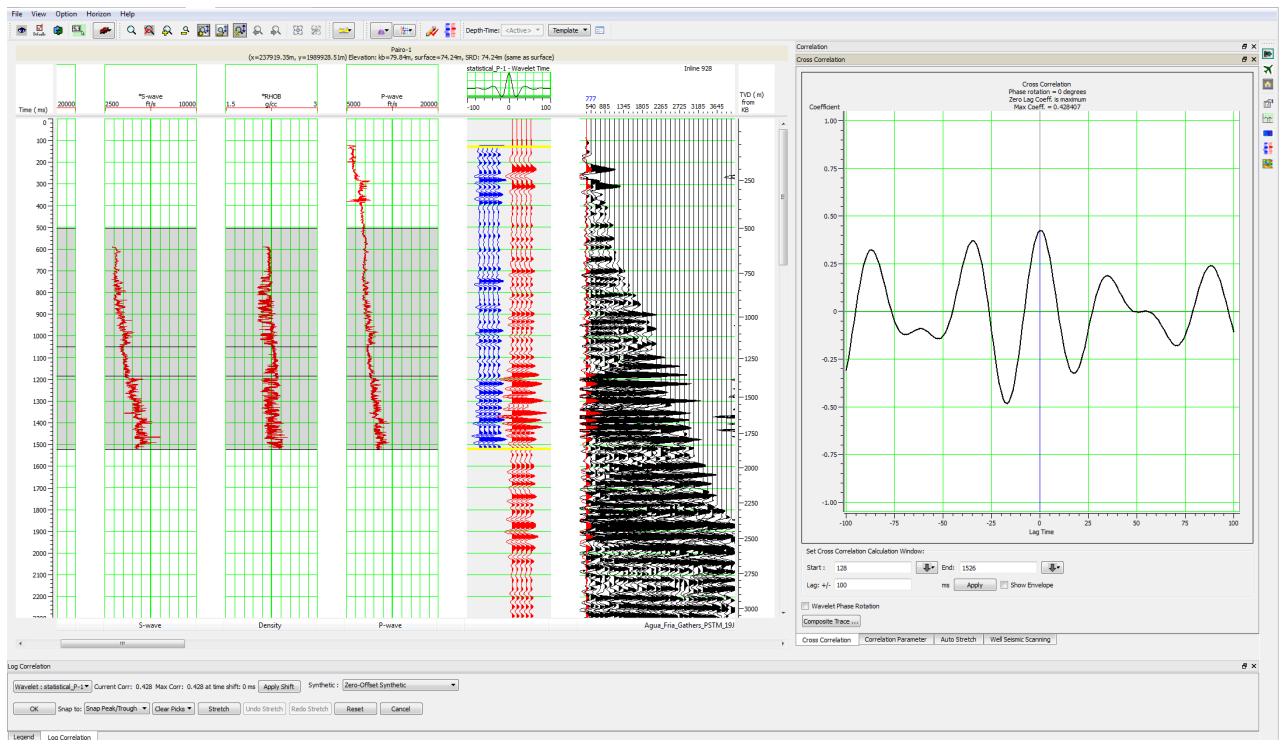
Figure B.8: Well P-1 correlation.

Appendix C

AVO attributes

B-1

IL-453
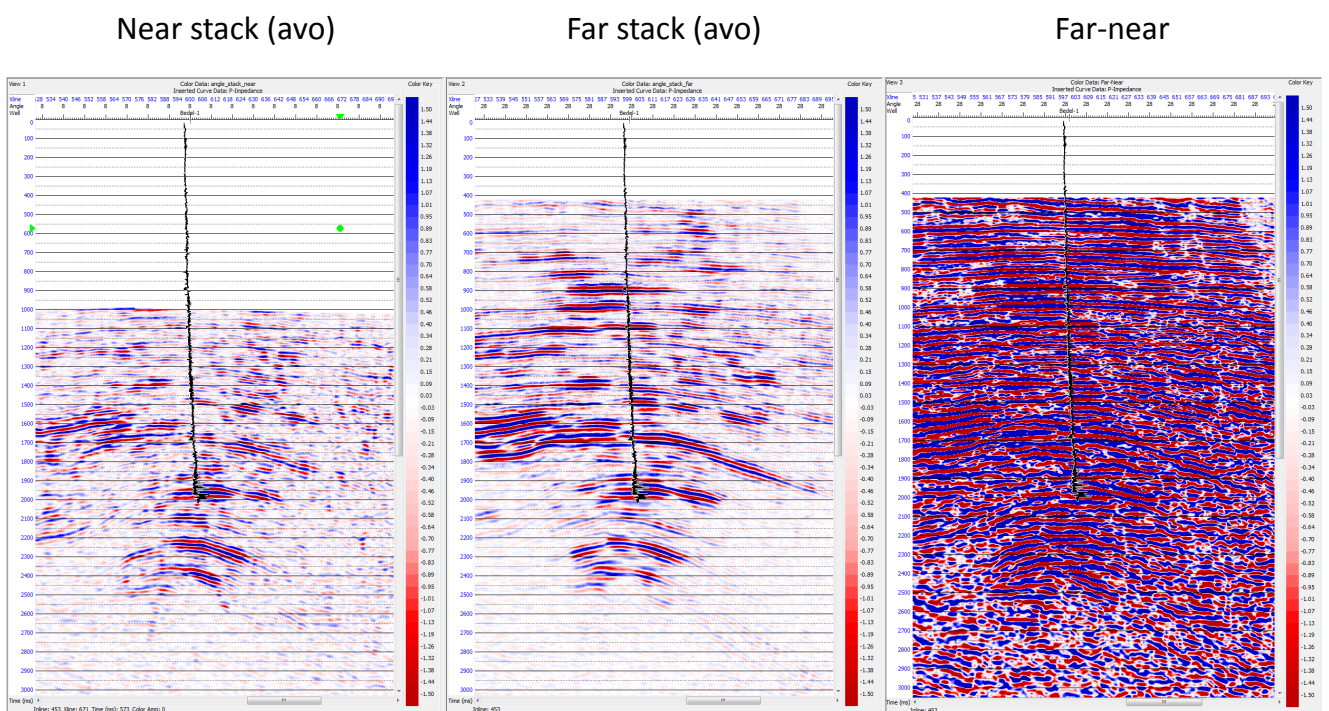
Figure C.1: Well B-1 AVO attributes.

C-1

IL-922

Near stack (avo)   Far stack (avo)   Far-near
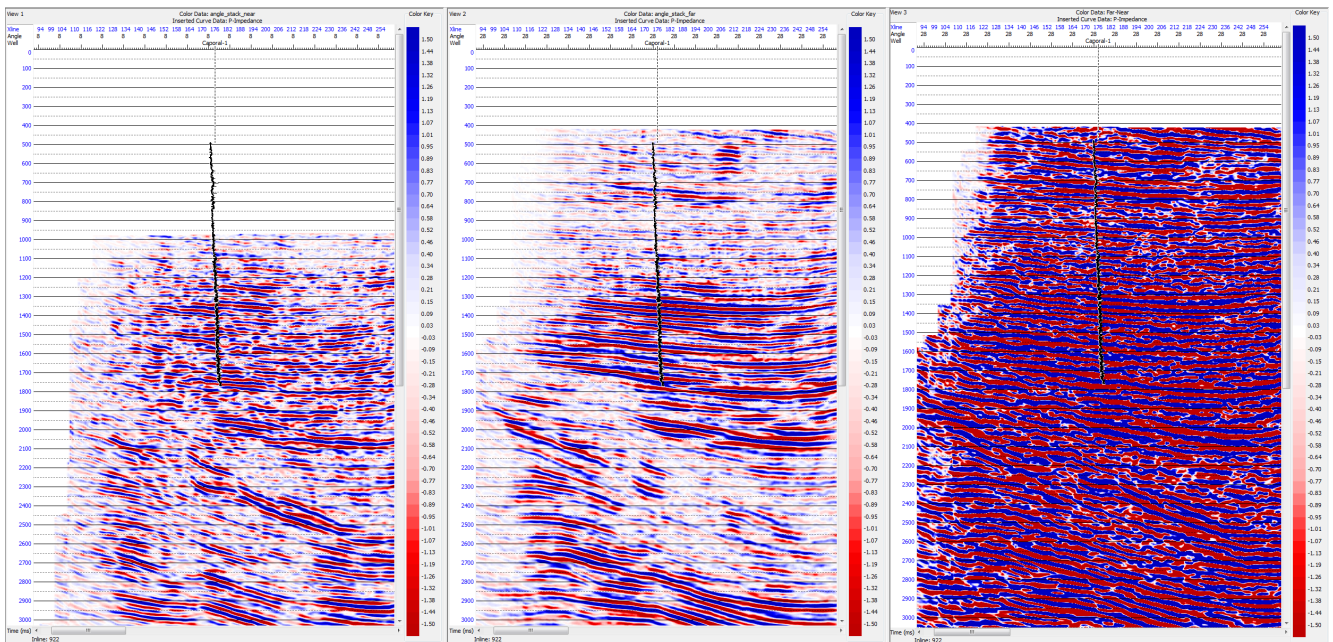
Cross Corr. = 78%

Figure C.2: Well C-1 AVO attributes.
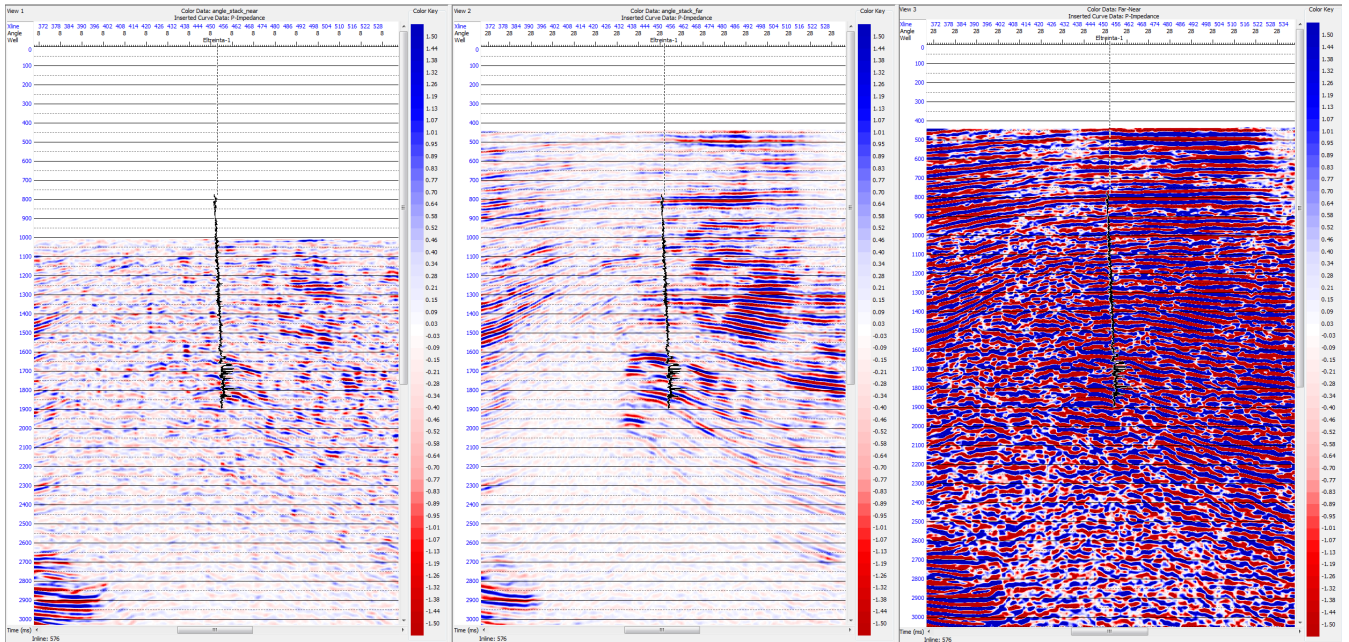
E-1

IL-576

Near stack (avo)   Far stack (avo)   Far-near
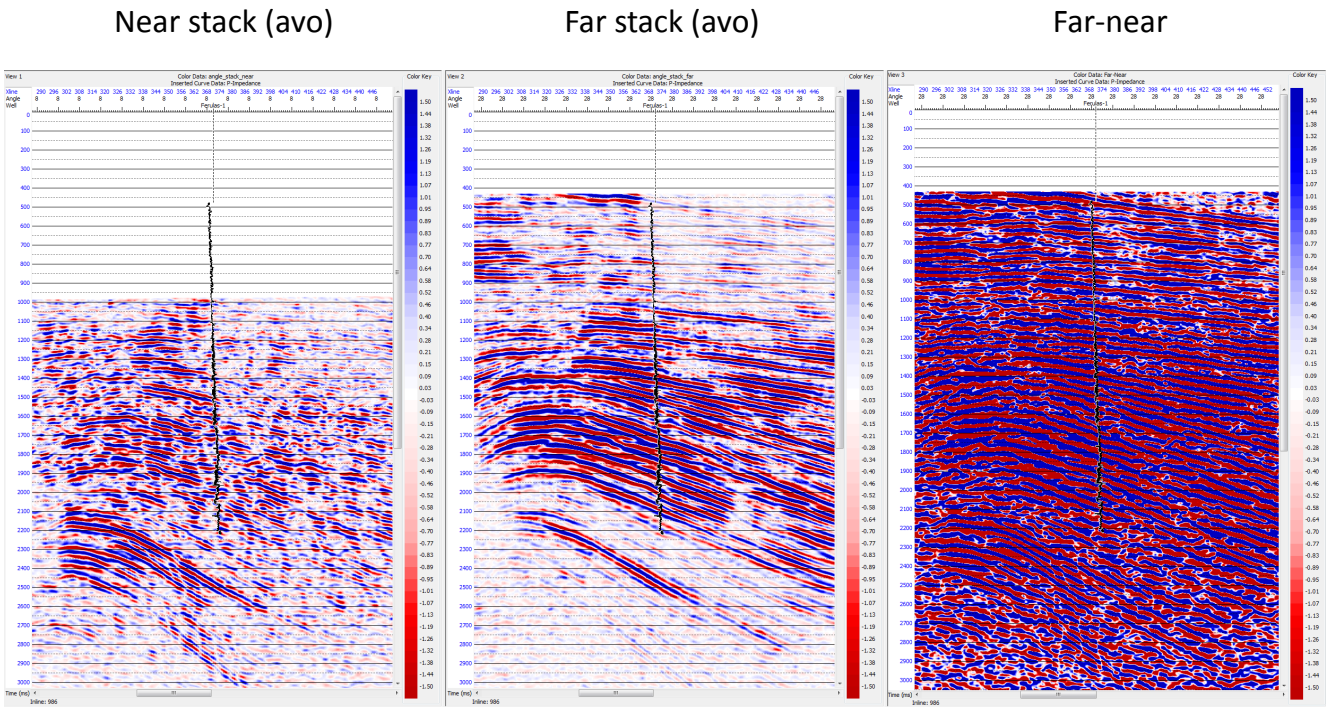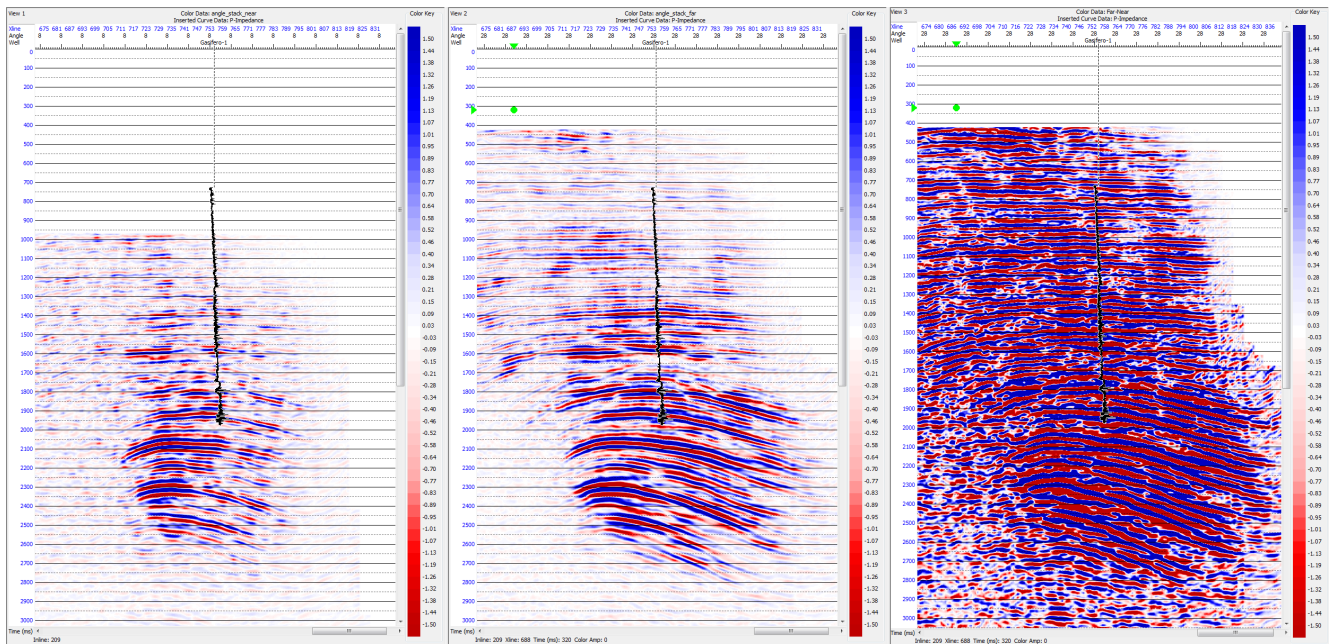

Figure C.3: Well E-1 AVO attributes.

F-1

IL-986

Near stack (avo)   Far stack (avo)   Far-near

Figure C.4: Well F-1 AVO attributes.

G-1

IL-209

Near stack (avo)   Far stack (avo)   Far-near

Figure C.5: Well G-1 AVO attributes.

M-1

IL-339

| Near stack (avo) | Far stack (avo) | Far-near |

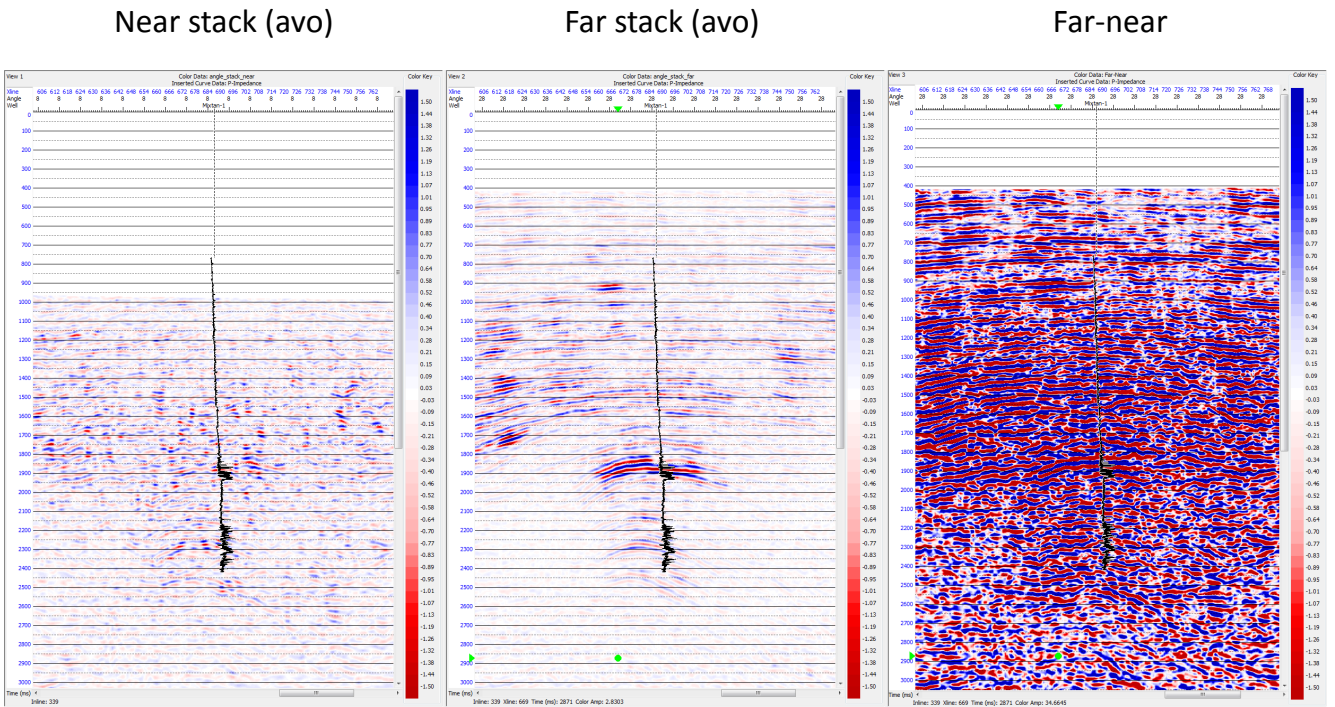**Figure C.6:** Well M-1 AVO attributes.

P-1
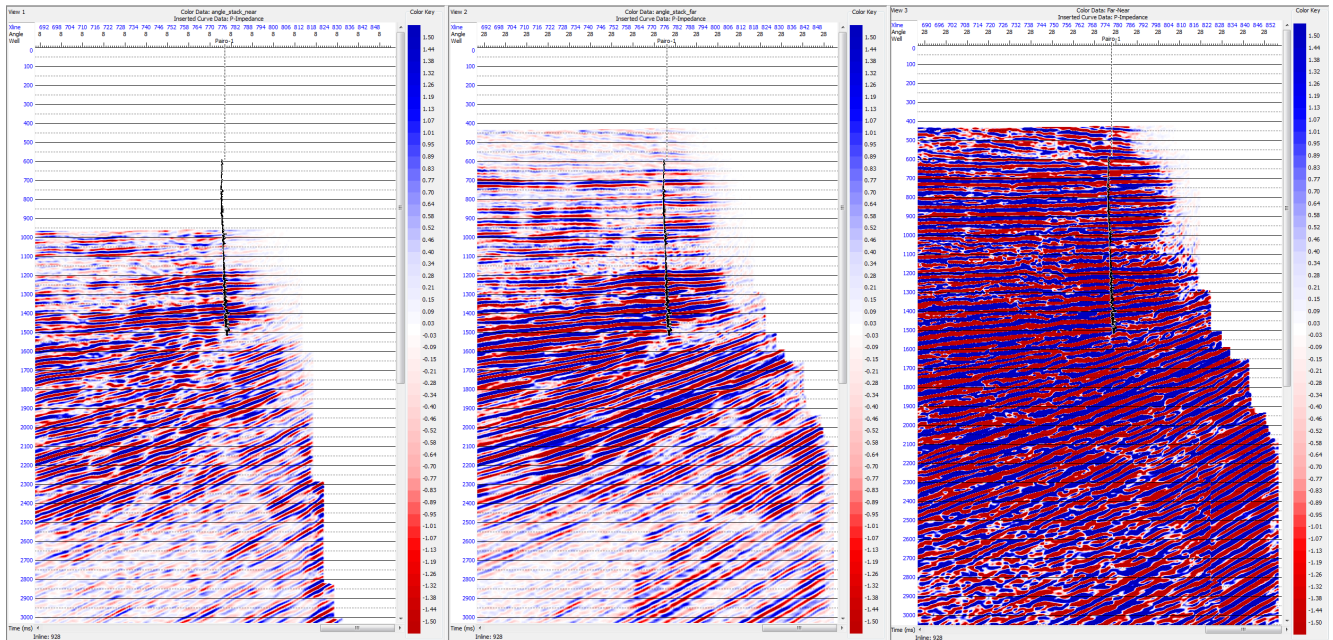
IL-928

Near stack (avo)   Far stack (avo)   Far-near

Cross Corr. = 42%

Figure C.7: Well P-1 AVO attributes.